POLITECNICO DI TORINO

Corso di Laurea Magistrale
in Ingegneria Energetica e Nucleare

Tesi di Laurea Magistrale

Fabrication and encapsulation of micro-SOFCs

Improving the reliability of the system: integration of MEMS technology and novel thin film anode

Relatore

Prof. Federico Smeacetto

Prof. Ferraris Monica

Tarancón Rubio Albert

Candidato

Andrea Turchi

Anno Accademico 2018/2019

Abstract

In the last decades, there has been a huge proliferation of portable devices with increasing energy demands due to the exponential growth of their applications and functionalities. Up to now, batteries have been the main integrated power sources adopted, but, since they are reaching their energy density limit, new technologies are demanding with higher power and storage density, high electrical grid autonomy and able to be miniaturized.
Therefore, in the last years, many efforts have been made by research groups to develop new low power regime (1 – 20 W) supply systems. Due to their long lifetime, high autonomy and power density, micro fuel cells appeared as promising alternatives. Among them, micro solid oxide fuel cells (micro-SOFCs) present the highest value of specific energy density (either by mass and/or volume unit) and they allow a direct operation with hydrocarbons.
The *Ultra-SOFC project*, funded by the European Research Council (ERC) and developed by IREC (Catalunya Institute of Energy Research) and ICREA (Catalan Institution for Research and Advanced Studies) collaboration, is developing functional free-standing membranes (i.e. a thin electrolyte covered by the electrodes, an anode and a cathode one at each side) integrated in silicon-based micro fabricated substrates.

This thesis is carried out in the framework of the *Ultra-SOFC project* and it aims to develop innovative solutions in micro-SOFC state of art to increase reliability. As shown in the following picture, two main topics have been considered: (1) the optimization of the joining thermal treatment and characterization of a commercial glass-based sealant (carried out mainly at POLITO) and (2) a new ceramic anode deposited as a thin film (carried out at IREC).

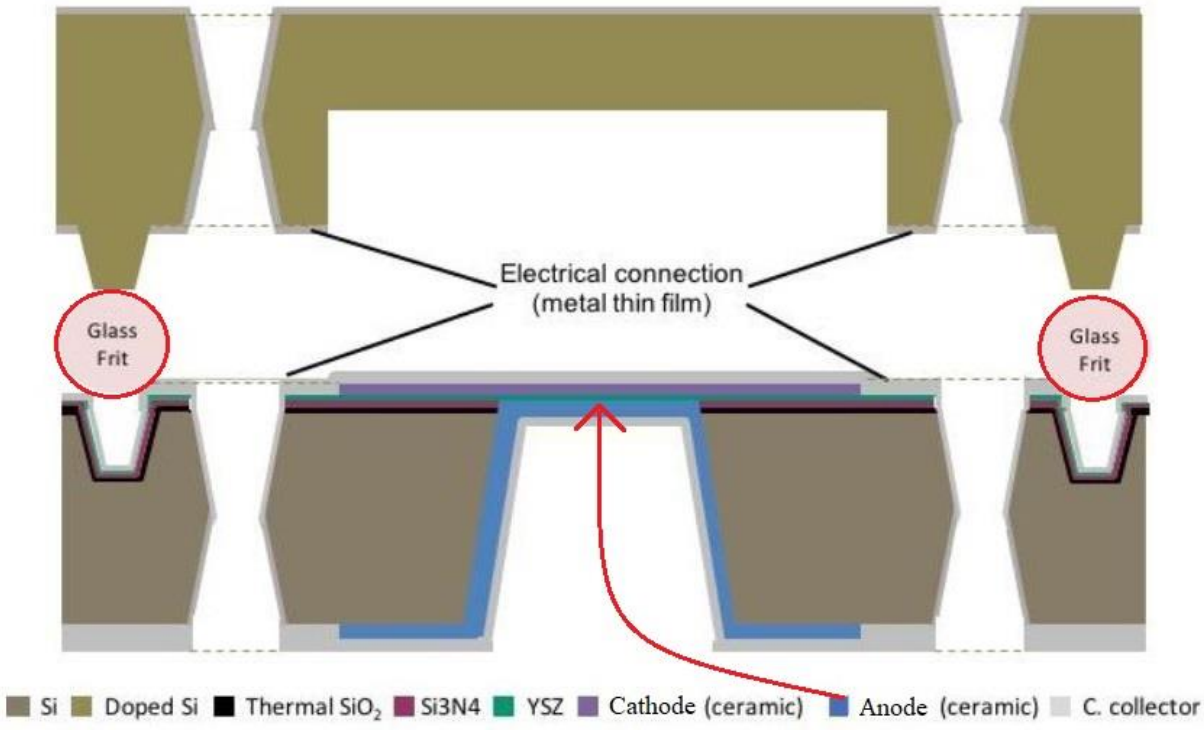

The MSc thesis is composed of four themed chapter.

Chapter 1 introduces the fundamentals and challenges of a micro-SOFC power generator. The principles of functioning, the fabrication techniques, the different type of micro fuel cells and the different materials adopted until now are review and discussed. In the last part of the chapter, the *Ultra-SOFC project* and relative challenges are presented.

The second chapter gives a brief overview of the main Si-wafer joining techniques and the anodes tested for micro-SOFC devices; the main focus is given to glass-based seals and thin film anodes.

The third chapter focuses on the experimental procedures and characterization techniques used in this work. A deep study on the glass-based sealant properties (thermal expansion coefficient (CTE), viscosity, shrinkage behaviour, wettability on different surfaces) have been carried out by comparing two different thermal treatments applied for the joining of two silicon chips. Moreover, a controllable fine line deposition technique has been developed (liquid deposition modelling, LDM).
Simultaneously, the complete characterization route of a strontium-doped lanthanum titanate (LST) thin film ceramic anode is reported, with a description of the experimental method. The work has been carried out considering four different films, obtained with pulsed laser deposition (PLD) technique, by varying the chamber deposition pressure.

The results on the glass-ceramic sealant and on the LST thin film anode are described in chapter 4. Crystallizations at temperature above 675°C have been detected in the glass seal with X-ray Powder Diffraction (XRD) and Scanning Electron Microscopy (SEM) analyses. They should be the responsible of the CTE variation, allowing a good matching (4,716 10^{-6} K^{-1}) with the silicon substrate in the whole range of operating temperature (100 – 600 °C). Moreover, by reaching 700°C during the thermal treatment necessary for the joining, a specific volume reduction of 40% is obtained, thus leading to a reduced porosity and an optimal wettability and adhesion of bonding surfaces. Deposition tests were performed and optimized; leak tests experiments, to access hermeticity of the joining, are necessary to evaluate the glass-ceramic bonding gas tightness.
Four types of films have been deposited with PLD showing different structures, thickness (around 115 – 170 nm) and roughness (with a minimum value around 2 nm) with SEM, ellipsometry and atomic force microscopy (AFM) analyses. In-plane electric conductivity tests have highlighted a strongly difference with the anodes of bulk SOFCs, especially in terms of maximum conductivity (0,2 S/cm). At list 20% of Titanium lack in each film is the main responsible of the low electric properties, since its reduction from Ti^{4+} to Ti^{3+} is the main phenomenon which allows the electrons migration. A further work based on the exsolution of Ti nanoparticles could enhance the conductivity of the films. On the other side a very low activation energy has been measured (down to 0,07 ev) evincing the LST as a promising material for thin film anodes. Moreover, a grain boundary size (hence pressure deposition) correlation with conductivity and activation energy has been demonstrated. Indeed, the larger the film grain size,

the higher electrical conductivity and the lower activation energy have been obtained. Anode electrochemical performance was tested on LST/YSZ/LST symmetrical cells, showing high ionic impedances and an activation energy of 1,6 ev.

In conclusion, the joining thermal treatment of a glass-based sealant for micro-SOFC has been optimized as well as its fine deposition by using the LDM technique. Furthermore, an innovative thin film ceramic anode has been tested, showing very low activation energy with large grain size and hence opening new strategies for a full ceramic-based micro-SOFC.

INDEX

1 INTRODUCTION

1.1 Fuel Cell fundamentals

A Fuel Cell (FC) is an electrochemical reactor that can directly convert chemical energy into electrical and thermal energy [1]. Although this technology appeared for the first time in the 19th century, it has been widely developed from the second part of the 20th century. In fact, it became attractive as a clean and pollution-free technology with high power density and lifetime comparing to the traditional power sources, based on pollutant fossil fuels or limited duration like batteries. Despite all these advantages, further research is necessary to improve this technology in terms of safety, materials and fabrication optimization, in order to enhance the reliability of the system and reduce the production costs [2].
This chapter aims to summarize working principle of these devices with a complete description of the main FC types existing and the different kind of materials used. In the last part, the main advantages and challenges with possible routes of optimization are resumed.

1.1.1 Principles of functioning

Figure 1-1 shows the basic structure of an electrochemical device, in which a global redox reaction occurs [3]. In a FC, a fuel and an oxidant flow through the anode and cathode respectively (the electrodes), generating electrical energy by the oxidation of the former and reduction of the latter. The electrolyte is placed between the electrodes and is responsible for the ions diffusion, whereas the electrons flow through an external circuit, closing the redox reaction. The electrolyte has to be gas tight in order to prevent the direct contact of the oxidizing and reducing atmospheres.

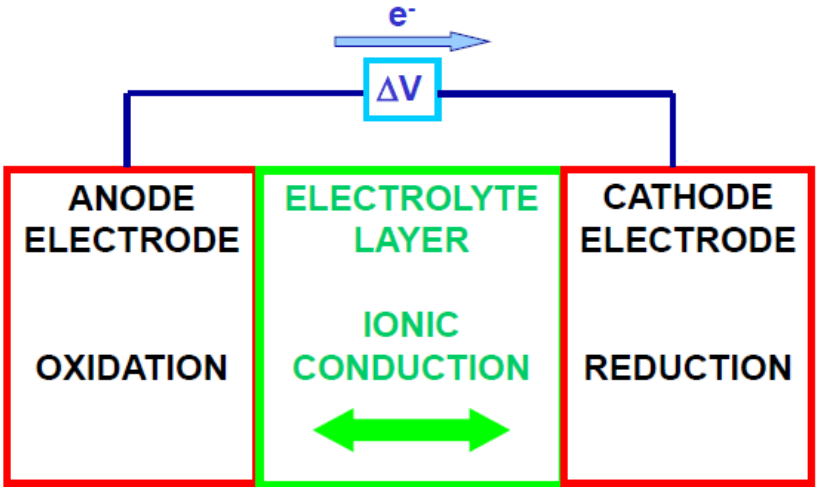

Figure 1-1. Electrochemical cell scheme of functioning (extracted from [1]).

The thermodynamic properties of a FC directly depend on its open circuit voltage (OCV), a measure of the electrochemical potential in equilibrium conditions. It can be expressed by the Nernst equation (1.1):

$$E_{FC} = -\frac{\Delta \bar{g}_{react}(T,p_0)}{z \cdot F} + \frac{R \cdot T}{z \cdot F} \cdot \ln\left[\frac{\prod_R p_r^{\gamma}}{\prod_P p_p^{\gamma}}\right] \qquad (1.1)$$

where z is the charge number (2 for hydrogen as fuel), F is the Faraday constant (96487 C/mol), $\Delta\bar{g}_{react}(T, p_0)$ is the variation of the molar Gibbs free energy between products and reactants calculated in a reference pressure P_0 (usually ambient pressure), R is the ideal gas constant (8,314 $J \cdot K^{-1} \cdot mol^{-1}$), T the temperature (K), p_r and p_p the partial pressures of the reactants and products respectively, each raised to the power of their stoichiometric coefficient ϒ.
In principle, any kind of chemical substance capable to be oxidized/reduced can be used as fuel/oxidant. Practically, hydrogen (H_2) has become the most considered fuel for this application, because of its high reactivity with suitable catalysts. On the other hand, oxygen (O_2) is usually used in the cathode side (in form of air) due to its easy handling and access. Therefore, the complete reaction associated to the cell is the formation of water (H_20) from H_2 and O_2, whose equilibrium potential is +1,229 V. Table 1-1 shows the reactions at the electrodes (hydrogen oxidation at the anode and oxygen reduction at the cathode) and the complete one.

Table 1-1. Electrode and fuel cell reactions.

ELECTRODE	Reactions	
Anode	H_2 oxidation	$H_2 \leftrightarrow 2H^+ + 2e^-$
Cathode	O_2 reduction	$\frac{1}{2}O_2 + 2e^- \leftrightarrow O^{2-}$
Complete cell	Formation of H_2O	$\frac{1}{2}O_2 + H_2 \leftrightarrow H_2O$

Hydrogen is not common as energy vector due to safety and techno-economical reasons (storage and transportation are problematic); therefore, alternative fuels are often employed, especially for high-temperature FCs (700-1000°C) whereby the fuel reforming results more efficient. The electric potential varies for each kind of fuel unless hydrogen is produced directly inside the device.

Passing from the equilibrium conditions (without any current flowing) to the operating ones, electric power is produced reaching a maximum value depending on the polarization losses (see figure 1-3). These phenomena have chemical and physical origins and are related to the amount of current flowing through the cell. In principle, three major losses have been identified, i.e. *activation losses, ohmic losses* and *concentration losses.*

- *Activation losses* (η_{act}) are related to the electrochemical reaction of the electrodes and their kinetic behaviour. When low current is flowing through the cell, the origin driving force (voltage potential) must be consumed to activate the charge transfer, which means to overcome the so-called **activation energy (E_a [ev])**. The E_a depends on temperature, catalyst (type, quantity, granulometry) and electrodes material [3]. In synthesis, it is a function of the *triple phase boundary* (TPB) length, physical spaces in which ionic, electronic and porous phases merge together (see figure 1-3).

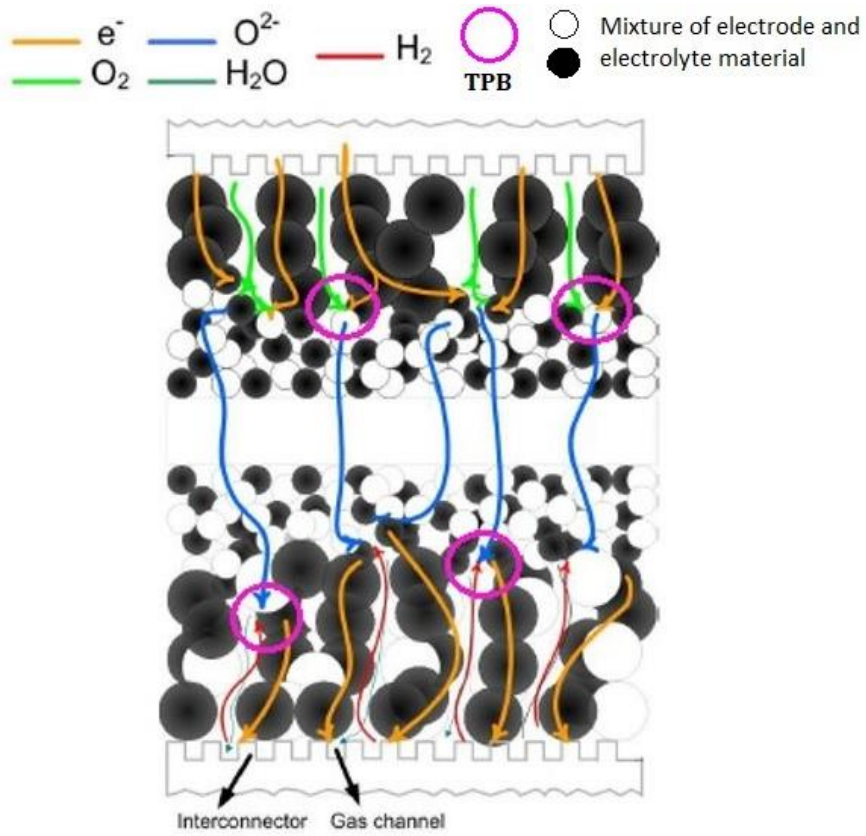

Figure 1-3. Schematic representation of the three phase boundary (adapted from [3]).

- *Ohmic losses* (η_{ohm}) are related to the migration of charged species in conducting materials. They are mainly caused by the ionic resistance (in principle higher than the electronic ones) through the electrodes and the electrolyte. The dependence between the potential and current density is linear, whose constant is the **area specific resistance (ASR [$\Omega \cdot cm^2$])**. ASR is a function of temperature, electrolyte and electrodes material (type and granulometry) and the conduction path of the charged species [3].

- *Diffusion losses* (η_{diff}) strongly depend on the current density and they are related to the diffusion capability of the reactant molecular species inside the electrodes. Temperature, layer porosity and tortuosity are the main governing factors of this physical mechanism [3].

Therefore, the operation voltage (V_{op}) is determined by:

$$V_{op}(i) = OCV - \eta_{act}(i) - \eta_{ohm}(i) - \eta_{act}(i) \qquad (1.2)$$

Every value of current density determines the corresponding potential and electric power. Figure 1-2 shows how these irreversibilities act determining roles for different values of flowing current. Every overvoltage represents a negative contribution to the fuel cell efficiency; therefore, it is fundamental to reduce the materials contribution to resistance as much as possible.

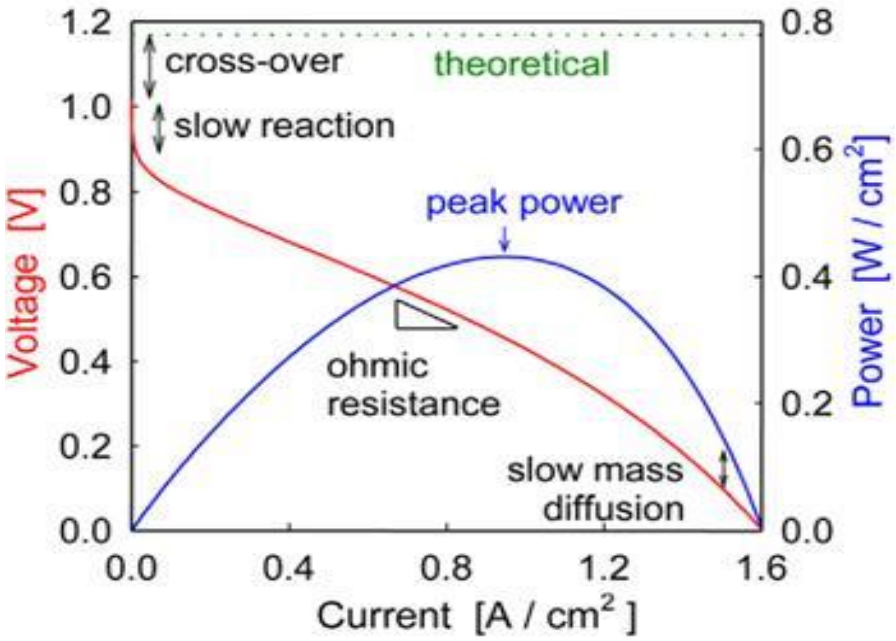

Figure 1-2. Schematic fuel cell polarization, voltage and power density vs. current density (extracted from [4]).

1.1.2 Fuel Cells classification

Table 1-2 summarizes the wide variety of existing fuel cells. They differ from each other because of design approaches, i.e. the use of different type of fuels and consequently specific electrolyte materials conducting different type of ions. The operating temperature plays a key role because it determines the type of useable fuel. In fact, low-temperature fuel cells, e.g. Proton Exchange Membrane Fuel Cells (PEMFC) or Alkalize Fuel Cells (AFC), need hydrogen as fuel; an exception are Direct Methanol Fuel Cells (DMFC) which work with direct methanol injection in the system. Fuel cells operating at higher temperature, like Solid Oxide Fuel Cells (SOFC) or Molten Carbonate Fuel Cells (MCFC), can use a wider variety of hydrocarbons, thanks to the internal reforming, that could happen directly at the anode surface (direct-FC) or in a separate reformer (H_2 on-board production). In both cases, these approaches consist in multistep reactions occurring at the catalyst surface (anode or external reformer) which finally lead to the formation of gas mixture (including H_2, CO and CO_2). The selectivity of the catalyst towards the fuel is an important parameter.

For instance, considering methane as fuel, two main reactions occur (*steam reforming* and *water gas shift*) which are resumed in the equations (1.3) and (1.4):

$$CH_4 + H_2O \leftrightarrow 3H_2 + CO \qquad (1.3)$$

$$CO + H_2O \leftrightarrow CO_2 + H_2 \qquad (1.4)$$

Table 1-2. Summary of main characteristics of different fuel cell types.

FC type	Electrolyte material	Mobile ion	Fuel compatibility	Operating temperature (°C)
PEMFC	Hydrated polymer	H^+	H_2	30 - 100
DMFC	Hydrated polymer	H^+	H_2, CH_3OH	30 - 100
AFC	KOH or NaOH solution	$(OH)^-$	H_2	50 - 200
PAFC	H_3PO_4 solution	H^+	H_2	200 - 250
MCFC	Molten salts (K_2CO_3)	CO^{3-}	H_2, CH_4	650
SOFC	Ceramic	O^{2-}	H_2, hydrocarbons	700 - 1000

PEMFCs are one of the most mature and commercialized technology in this field, ranging from fuel cells for vehicles to stationary auxiliary power units for houses. However, they have some shortcomings like flooding, relative unavailability of hydrogen, high cost of bipolar plates and low operating temperature which limits their operation with H_2. SOFCs usually operate above 700°C which permits the use of different types of fuels (methane, butane, ethanol, gasified biomass). SOFCs are considered a promising alternative electric power generation system due to high energy-conversion efficiency, environmental safety, low noise and a possibility to recover exhaust heat. For all these advantages, SOFC technology has been considered in this thesis.

1.1.3 Solid oxide fuel cell materials

This chapter aims to briefly summarize the state of the art of the materials used for bulk SOFCs. Even though the focus of this thesis is related to a miniaturized device (see section 1-2), it is important to underline that every material implemented in the micro scale is inspired by the "big" one.

Two main types of SOFC configurations have been developed: the tubular and the planar one. The former (patented by *US Westinghouse Electric Corporation* in the 70s) possesses the main advantage is the hermetic design which does not permit any fuel leakage even at high temperature. Anyway, their connection and hence the formation of stacks, which increase the total power produced, is difficult because of the related high ohmic losses [6]. Therefore, the simpler process to obtain a stack and the widely spread research on materials in the last decades, which allowed for improved performances, favour the planar configuration.

Planar SOFCs are characterized by a supported design, which can be extern or autonomous i.e. a part of the cell itself. Figure 1-4 shows the configuration of a planar SOFC with a summary of the main materials used for each component and their related issues.

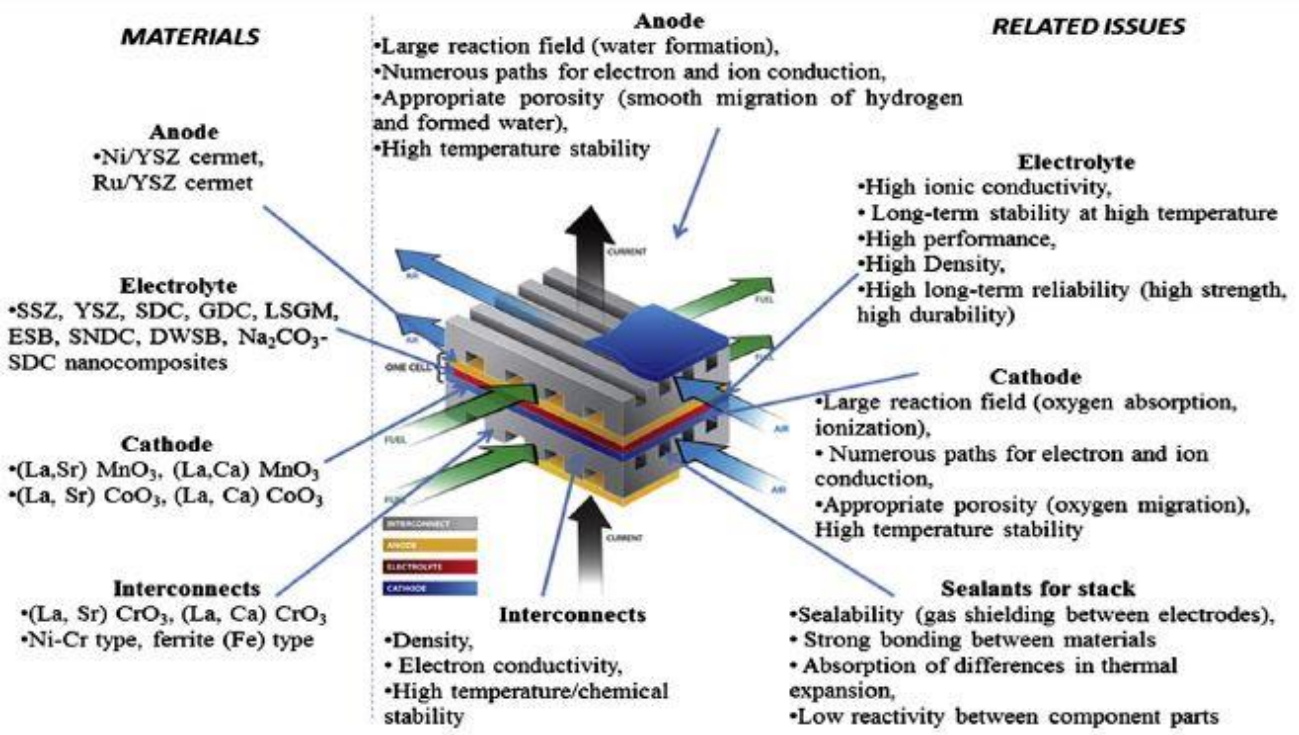

Figure 1-4. Planar SOFC scheme with materials used and related issues (extracted from [2]).

Every fuel cell is composed of five elements: anode, electrolyte, cathode, interconnect and sealant; their main features and materials are listed below:

- **Anode**

  Anode materials should possess enough electrocatalytic activity with H_2 and high electrical conductivity (≥100 S/cm). It must also possess good chemical and thermal stability along with minimal thermal expansion coefficient (CTE) mismatch with other adjacent cell components. Finally, it should be able to handle fuel flexibility with hydrogen, CO and other hydrocarbons tolerating carbon deposition and sulphur poisoning [2].

  At the beginning, metals were both used as anode and cathode, such as platinum, graphite, iron, cobalt and nickel either for low cost, good chemical stability or excellent catalytic activity. Ni was used for several years but its CTE is largely different from the common electrolyte used. Afterwards, an yttria-stabilized zirconia (YSZ) matrix was implemented around Ni particles allowed to reduce the CTE mismatch and enhance the adhesion between anode and electrolyte [6]. Cermet (e.g. Ni/YSZ) materials face several issues with the variation of fuel. For instance, using CH_4 as fuel, at high temperature, the presence of Nickel could cause the deposition of carbon whiskers which block the ion (O^{2-}) motion. Since O^{2-} ions cannot find any molecule of external fuel to oxidize, they form NiO which irremediably breaks the cell [7]. One interesting approach to replace Ni cermet is to introduce a mixed ionic electronic conductor (MIEC) perovskite oxide (general formula ABO_3) and a well-dispersed electro-catalyst (e.g. CeO_2, GDC), [8]. The most promising perovskite families are **chromites** (Lanthanum chromites, $LaCrO_3$,

doped in A and B sites), **titanates** ($SrTiO_3$) and **molybdates** (double perovskite Sr_2MgMoO_6, SMM).

- **Electrolyte**

The electrolyte conducts O^{2-} ions migrating from cathode to anode and can be considerate as the heart of a SOFC. It must be dense, to avoid electrical and gas shortcut, and as thin as possible to reduce the ionic resistance. It must resist thermal shocks and be stable in oxidant and reducing environment [6]. Finally, the crystal structure of the electrolyte must possess a high amount of point defects and so high ionic conductivity [2].

The most used electrolyte material is yttria stabilized zirconia, YSZ. It is obtained by doping ZrO_2 by Y_2O_3 generating oxygen vacancies ($V_O^{\cdot\cdot}$), according to the following Kroger-Vink notation:

$$Y_2O_3 + 2Zr_{Zr} + O_O \rightarrow 2Y'_{Zr} + 2V''_O + 2ZrO_2 \qquad (1.5)$$

The increasing number of oxygen vacancies upon doping is responsible of the high ionic conductivity (≈0,1 S/cm at operating temperature) of the YSZ. Two different types of crystallographic structures are reported in literature: the fluorite and the perovskite structures. YSZ belongs to the first family, which possess face-centered cubic arrangement of cations, with anions occupying all the tetrahedral sites. Ceria oxide (CeO_2) has a fluorite structure too and it is used for intermediate temperatures SOFCs. However, since CeO_2 has not sufficiently oxygen vacancies, they are introduced by substituting Ce^{4+} with trivalent rare earth ions, like Gd^{3+}, Sm^{3+} or Y^{3+} [2]. On the other side, LSCM ($La_{1-x}Sr_xCo_{1-x}Mn_xO_3$), LSGM, LSGMC or $LaAlO_3$ perovskite-based materials are currently investigated [8].

- **Cathode**

Oxygen (from supplied air) flows and gets adsorbed onto the surface of a porous cathode and it is reduced by accepting electrons coming from the current collector. A cathode material should have high electronic conductivity and chemical stability, it should match the CTE with the other components and show sufficient porosity to transport oxygen molecules to the cathode-electrolyte interface, as well as high oxide ion conductivity [6, 9].

Lanthanum doped with alkaline or rare earth elements is commonly used as cathode material. LSM ($La_{1-x}Sr_xMnO_3$) perovskite is one of the most studied materials. Its conductivity origins from the substitution of a La^{3+} cation with a Sr^{3+} one, which generates an electric hole in the Mn^{3+} position (for the neutrality).

- **Interconnect**

Interconnects provide electrical connection between cathode of one cell to the anode of the adjacent one in a SOFC stack and ensure a physical barrier between two different atmospheres: oxidizing and reducing. They need to ensure: high electrical conductivity with ASR less than 0,1 Ωcm^2, structural and chemical stability in both oxidizing and

reducing atmospheres at high temperatures (800-1000 °C), excellent gas tightness and low ionic conductivity, matching CTE (≈ $10{,}5 \cdot 10^{-6}$ K^{-1}) with electrodes and electrolyte materials, non-reactivity with the cathode surface [2].
There are two classes of interconnect materials for SOFCs: ceramics and metallic alloys. $LaCrO_3$ and $YCrO_3$ belong to the first group and their conductivity becomes sufficient (≥1 S/cm) above 800 °C. If sintered in reducing atmosphere, these chromites tend to lose oxygen which cause both expansion of the structure and decreasing of conductivity. Therefore, doping with Sr or La could be a solution for at least the mismatch of CTE. Metallic interconnects have several advantages comparing to the ceramic ones: low fabrication costs, better electrical and thermal conductivity, low operating temperature (600 – 850 °C), [6]. Chromia forming ferritic stainless steels are the most widely used. However, a big issue related to the compatibility of these materials with the interconnectors is the Cr deposition and poisoning of the cathode. A possible solution is the coating deposition of $Mn_{1,5}Co_{1,5}O_4$ which blocks the Cr evaporation [2, 9].

- **Sealing**

  To connect the cells in series in the planar SOFC stack, sealant materials are needed to avoid any leakages of either fuel or air. Since they are always exposed to both oxidizing and reducing atmospheres at high temperatures, their strict requirements are: hermeticity, matching CTE to other components, tolerance to thermal shock and cycling, long-term chemical stability under oxidizing/wet fuel, naturally insulator, design flexibility, low cost and simple application [2].
  There are two main methods of sealing: compressive sealing (glass joining) or rigid sealing. In the first case, the material is typically fitted in-between two surfaces and compressed. Since the two adhesion surfaces could be different, with harsh conditions and high operating temperatures, there is a huge effort on this research field. Metallic (non-degraded but expensive noble metals like Pt, Au, Ag) and mica-based (phyllosilicates minerals like parallel sheets of silicate tetrahedra) compressive seals belong to this group. As regard rigid seals, they require a relatively simple bonding method (even with ceramic and metals) but they are expensive. They are electrical insulators (glass or glass-ceramics) and characterizable by thermal treatment which causes or not the formation of crystallizations. B/Ba/Al/Si-based glass-ceramics are the state of the art of the rigid seals [2].

1.1.4 Advantages and challenges of Solid oxide fuel cells as power sources

Compared to other electric power generation systems, SOFCs offer many advantages including high energy conversion efficiency and fuel flexibility by allowing the use of liquid and gaseous hydrocarbons as well as hydrogen [10]. They are also particularly attractive because:

- ✓ They can directly convert chemical energy into electrical energy [6];
- ✓ They emit low level of pollutants (no NO_x or SO_x emissions);

- ✓ They are low-vibration and low-noise systems [11];
- ✓ They have high volumetric energy density and specific power [6];
- ✓ Unlike batteries, they can continuously produce energy (as long as fuel is provided), [11];
- ✓ They have long life time, thanks to their ceramic materials, which resist at high temperature operation and harsh conditions;
- ✓ They can be integrated with gas/steam turbine systems for the energy cogeneration [6];
- ✓ They can be miniaturized [12].

The high price of the SOFC systems has been the major obstacle on the way to commercialization. As a result, research and development efforts are now focused on the cost reduction of the SOFC components and fuel cell stacks [13].

The performance of a fuel cell is mainly determined by three impactive losses (see chapter 1.1.1): the activation losses, originating from a limited rate of electrochemical charge-transfer reactions at cathode and anode; ohmic losses, due to the low ionic conductivity of the electrolyte membrane; concentration losses, caused by limited diffusion of gases through the electrodes [14]. To overcome most of these functioning issues, the required operating temperature is raised up above 800 °C. Nevertheless, high working temperatures cause other issues:

- Extended start up times [9];
- Stringent demands on materials selection to satisfy structural, chemical and thermal stability [10];
- Insulating sealings, expensive interconnect and integration of the balance of plant with SOFC stacks [9];
- Excessive interdiffusion kinetics between cell components due to high temperature thermal cycles [9];

Attempts have been made to lower their operating temperature (<500 °C) resulting in the so-called intermediate temperature SOFCs (IT-SOFCs). Since both sintering and radiative heat transfer decrease at low temperatures, materials degradation mechanisms and insulation costs are significantly reduced. Low operating temperatures on the other hand significantly increase fuel cell losses, and thus reduce cell performance [10].

Despite the discussed points, the high energy density (associated to the capability of using hydrocarbons), the easy and cheap fuel refilling and the possibility of packaging make SOFCs an attractive technology for miniaturization and portable applications (see chapter 1.2), [15].

1.2 Microfabrication and micro-SOFC state of art

Recent advances in miniaturization technologies allowed the downscaling of solid oxide fuel cells, launching this relatively new type of device as a possible candidate for portable applications (see section 1-3), [16]. Although fuel cell principle was invented more than 100 years ago, micro-FC technology is a relatively new field (≈20 years of research), [15]. The easily integration of micro-FC with the well-known silicon technology makes possible the implementation of new micro electro-mechanical systems (MEMS).

This chapter aims to resume the main microfabrication steps adopted for the micro-SOFC realization, and the state of art of this technology, by citing different approaches and designs of the research groups involved.

1.2.1 Microfabrication technologies

Micro electro-mechanical systems can be defined as the set of miniaturized structures which combine electrical and mechanical elements, developed by microfabrication techniques [17]. The main goals to achieve are miniaturization (reduce the substrate area) and multiplicity (simultaneously production). Considering the main core of a μSOFC, composed by positive electrode-electrolyte-negative electrode (PEN), there are basically two types of designs [18], as reported in figure 1-5: (1) free-standing membranes supported by a substrate material (typically Silicon) [14, 22, 25, 33,]; and (2) porous electrode support designs [5, 23, 24, 28, 34].

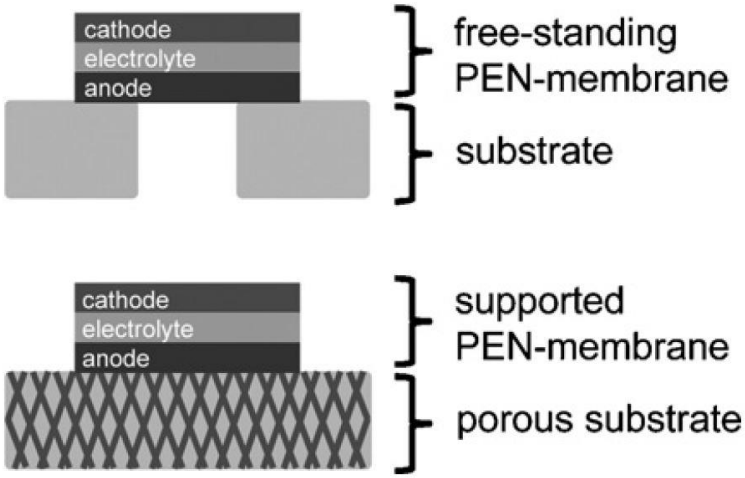

Figure 1-5. Schematic drawing of a free-standing PEN-membrane on top and PEN-membrane on a porous substrate in the bottom (extracted from [18]).

While the latter is not characterized by several micromachining steps, the former follows the process flow represented in figure 1-6, which is based on clean room-based processes. The three mainstream processes adopted for silicon micromachining are reported hereafter [17]: (i.) *patterning or lithography*, where a pattern is transferred from a master to a resin covering the silicon surface; (ii.) *etching*, where, a certain amount of material is removed following the

previous lithography; (iii.) *film deposition or growth*, where a new material is added on top of a surface.

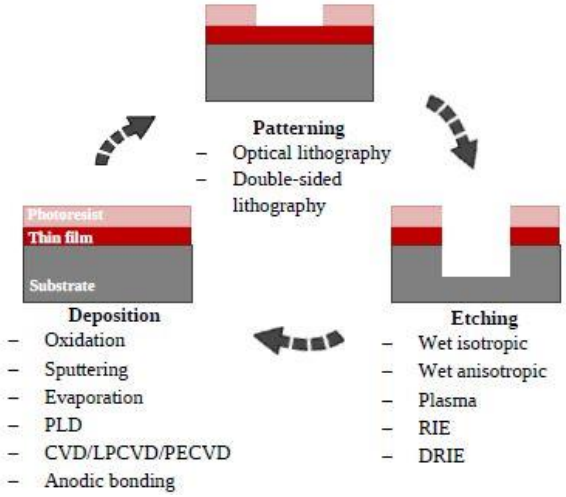

Figure 1-6. Basic microfabrication route in silicon technology (extracted from [19]).

- **Patterning or lithography**

  This process transfers a pattern from a master directly to the substrate. It is fundamental to build the desired design, by using this model as the base step for afterwards alterations, like removing, adding, growing or depositing any material [15]. One of the most extended lithographic techniques is *photolithography*. It is based on three sequential steps [17]: thin film *spin-coating* of a resin (photoresist) on the wafer; *optical exposure* through a mask by UV light to transfer the pattern onto the resin; *development*, where the resist is eliminated only from the desired zones by dissolving it on the proper solvent.

- **Etching**

  After a lithographic step, a pattern defined on the resin can be transferred to the substrate by adding or removing material. Etching refers to the second process, where the pattern is transferred by a physical or chemical removal of material from the substrate. There are basically two categories of etching processes: *dry etching* and *wet etching*. Both mechanisms can be either *isotropic* (similar etch rate in all directions) or *anisotropic* (different etch rate depending on the direction), as schematized in figure 1-7.

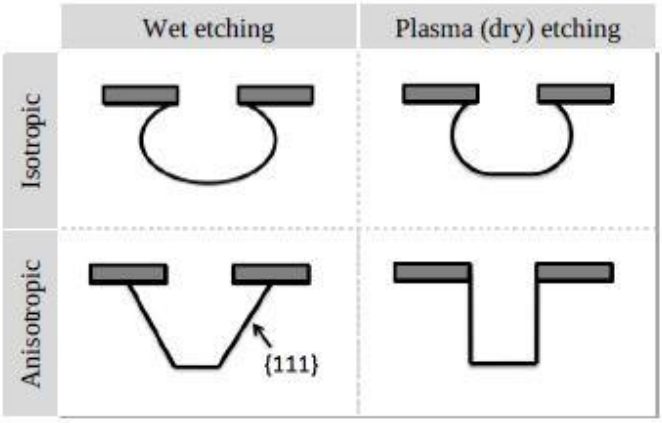

Figure 1-7. Four different types of etching methods (extracted from [17]).

Dry etching techniques involve gaseous reactants in low pressure plasma. For instance, Reactive Ion Etching (RIE) combines physical and chemical etchings, by using two different plasma species [15] or Deep-RIE (DRIE) or "Bosch process" used to create deep penetration, steep-side holes [50].
In wet etching techniques, the substrate is immersed on a chemical bath filled with the etching solution. For instance, anisotropic etchant KOH is widely used in silicon technology, due to its high predictability of the generated etching angle. In fact, the (111) planes of Si are not attacked, i.e. their etch rate is negligible compared to other planes [17]. Wet chemical etching provides higher selectivity and is often faster compared to dry etching [15].

- **Film deposition and growth**
  It is possible to include in this category all the techniques where a surface is modified for a specific purpose, like adding a functional layer of the membrane or even protecting the substrate material against corrosion [15]. Growing a film consists of a chemical surface change (like oxidation) and so no addition of any material is involved, which instead is the base principle of deposition. Both films can range from few to hundreds nanometers. One of the most used growing process consist in heating a silicon wafer (typically a thin circular plate of ~ 10 cm diameter) and reaching high temperature (600 – 1250°C) in oxidizing atmosphere (air, or a mixture of O_2/N_2), so that a thin layer of SiO_2 is produced [15]: it is an excellent thermal and electrical insulator and it could be used as mask or sacrificial layer in etching processes [17]. Compressive films are obtained with these high temperatures, therefore a tensile Si_3N_4 layer is often added to obtain a relaxed and thermo-mechanically stable substrate.
  As far a deposition is concerned, thin films are usually produced, due to miniaturization goals. They can be defined as a low-dimensional material (less than 10 μm) created by condensing, one-by-one, atomic/molecular/ionic species of matter, from a **target**, on a **substrate** [20]. Thin films exhibit peculiar properties that can be totally different from the bulk ones or can enhance them [21]. These techniques can be grouped into two categories: Physical Vapor Depositions (PVD) and Chemical Vapor Depositions (CVD). In PVD process no reaction takes place but only a material is vaporized and transferred directly to a substrate. While, a CVD process is based on chemical reactions in a controlled atmosphere. Main PVD techniques are sputtering (DC sputtering, RF i.e. radiofrequency sputtering or magneton sputtering) and Pulsed Laser Deposition (PLD, deeply described on section 3-2). Temperature and pressure are the main parameters which could affect the grain size, the thickness, the crystalline orientation and mechanical-electric-thermal-optical properties of a PLD film. As regard the CVD techniques, Atomic Layer Deposition (ALD) deserves to be cited thanks to its high thickness precision and conformal films. It is a self-limiting reaction in which alternative gaseous species (precursors) are overlapped and they interact in any reactive sites covering the whole surface.

Finally, doping is another technique used to modulate a silicon substrate [22]. Boron is typically used as p-type doping (one less valence electron than Si) and phosphorous, arsenic or antimony

are the elements for the n-type doping (one more valence electron than Si), [15]. Combining these microfabrication steps in different order, it is possible to design and modulate almost every geometry on silicon.
It is important to underline some limiting technical procedures which do not permit a trivial fabrication. For instance, photolithography, in combination with etching process, is complicated since the latter could damage cell materials. Moreover, the resolution of wet etching is generally limited to ~10μm, while dry etching would allow much finer patterns, but it is quite time-consuming for multi-micron thick nickel substrate [24].
Another important challenge regards the production of large-area thin membranes which could enhance the performances (large flux of ions but small thickness of the electrolyte, so low resistance). Indeed, the active area cannot be increased by simply interconnecting several microscale junctions, because, for instance, the KOH anisotropic etching leaves an extremely poor area of utilization with a limited thickness of the substrate [25]. Great efforts are spent in order to maximize the active area and each research groups adopts different approaches, as resumed in the next section.

1.2.2 Micro solid oxide fuel cells state of art

As reported in section 1-1, the operating temperature of a bulk SOFC is above 700°C. The use of nanoscale electrolyte and its integration in silicon technology allowed to decrease the micro-SOFC working temperature to 300-500°C [25].
Reducing temperature is considered crucial for facilitating encapsulation and integration of other components in the final system (i.e. electrodes degrade faster at high temperature). On the other hand, higher temperatures are necessary to promote the hydrocarbon reforming. Nowadays, this difficult trade-off is managed with two opposed strategies [16]:

1. A first approach is to lower the operating temperature, close to room temperature (RT). Encapsulation and heat management would be easier, but electrolytes with higher conductivity than YSZ and electrodes with enhanced surface catalytic activity are necessary.
2. A second approach is to increase the operating temperature, guaranteeing new possibilities of hydrocarbons as fuels. It would be necessary to abandon the highly degrading metallic electrodes and substitute them with more thermomechanically stable ceramics. Here, the thermal management would be challenging, and the device would require an excellent encapsulation and compact integrations with all the components.

Table 1-3 resumes the main results obtained by the different research groups. Key factors to evaluate and compare these works are: the OCV generated by the single cell, as well as its power output; the operating temperature; the total membrane thickness; the maximum active area obtained; the different materials used for the electrolyte and the electrodes. Only the significant results (maximum total power or power density) are reported per each group, adapting the state of art resumed by I. Garbayo et al. in [22]. Pt has been the material of choice for at list one of the electrodes in almost all the designs. Its quick degradation associated to dewetting processes and subsequent loss of performance has been reported as a key issue for the power stability [22].

Table 1-3. Summary of the main results reported on μSOFCs (adapted from [22]).
{*Corrugated membranes; power density calculated respect to the projected area}.

Group	*Anode (dep. tech.)*	*Electrolyte (dep. tech.)*	*Cathode (dep. tech.)*	*Thickness (nm)*	*Active area (mm^2)*	*OCV (V)*	*Power density (mW/cm^2)*	*Total power (mW)*	*Temperature (°C)*	*Year*	*Ref.*
Stanford University	Pt (sp)	YSZ (ALD)	Pt (sp)	310	4	1,12	198	2,98	450	2012	[26]
	Pt (sp)	YSZ-YDC (ALD)	Pt (sp)	220	0,002	1,05	1300*	0,024	450	2013	[27]
ETH Zurich	Pt (sp)	YSZ (PLD)/YSZ (s.pyr)	Pt (sp)	660	0,03	0,57	209	0,063	550	2012	[28]
	Pt (sp)	YSZ (CVD)/ YSZ/CGO (CVD)	Pt (sp)	260	0,13	0,84	166	0,22	410	2013	[29]
EPF Lausanne	Pt (sp)	YSZ (sp)	Pt (sp)	600	0,8 (with Ni grid)	0,85	0,02	0,0002	500	2010	[30]
Harvard University	Pt (sp)	YSZ (sp)	Pt (sp)	260	0,03	0,97	1037	0,31	500	2011	[31]
	Pt (sp)	YSZ (sp)	LSCF (sp)	131	25 (with Ni grid)	0,75	155	21,1	510	2011	[25]
KIST	Pt on AAO (sp)	YSZ (PLD)	Pt (sp)	1060	0,01	1,02	350	0,035	500	2011	[32]
Sony Corp.	Ru (DC sp)-CGO (RF sp)	YSZ (DC sp)	Pt (sp)	270	-	0,97	275	-	485	2012	[33]
Pohang University	Ni-YSZ (PLD)	YSZ (PLD)	LSC (PLD)	3300	3	1,0	560	16,8	550	2016	[34]
IREC	Pt(sp)/CGO (PLD)	YSZ (PLD)	Pt(sp)/LSC (PLD)	850	2	1,05	100	2	750	2015	[17]

Only the significant works of the different research groups are considered.
This master thesis belongs to the Ultra SOFC European Project by IREC (widely descripted in section 1-4) as a further development of the results resumed in the table [17].

It is important to focus the attention on the output power density obtained, since a batch mode fabrication (like the wafer-level one) could strongly reduce the fabrication costs [15]. In this sense, Ramanathan et al. published output power densities higher than 1000 mW/cm^2, respectively 1300 mW/cm^2 at Stanford University and 1037 mW/cm^2 at Harvard University (see table 1-3).
Although these brilliant results, it is possible that a little modification on the design would lead to a strong variation on performance. Indeed, the choice of materials and deposition types, temperature and set-up conditions (for the electric power measurements) could deeply change the output power. According to literature, the performance variation seems to be related to the low stability and fast degradation of the thin film metallic electrodes at micro SOFC working temperatures [15]. Micro-FC durability tests are a lack of knowledge up to now.
Another observation which can be extracted looking the table 1-3 is related to the OCVs values. Some of them are far from the theoretical one (1,23 V, see section 1-2) but others seem to be closer (~1,1 V), like [17,26,27]. Literature reports justify this gap to two causes:

1. *Sealing problems*: electric shortcut between electrodes due to a non-homogeneous sealing layer or even loss of performance due to a non-hermetic sealing;
2. *Pinholes issue*: leakages between anode and cathode through the electrolyte membrane. This is one of the most difficult problem to deal with, because a clean process without any particle and dust must be realized. Clean rooms are necessary (like the IMB-CNM at Autonomy University of Barcelona), with a completely controlled atmosphere equipment like sensors of particle per cm^3.

In this scenario, it is evident that further research works on materials and operating test conditions are fundamentals. For instance, increasing the electrolyte thickness or depositing a multi-layer thin film electrolyte can minimize the pinholes issue. Working with thermo-mechanically stable functional materials is another solution to null the degradation of the electrodes. So, by a direct comparison with the bulk SOFCs, full-ceramic membranes seem to be an ideal solution which is not widely developed, up to now. Finally, to ensure a better encapsulation and leakage control is fundamental for the reliability of the system.

1.3 Motivation

In the last decades, there has been a huge proliferation of portable devices (PD) and wireless sensor networks (WSN); those technologies are also called machine-to-machine (M2M) and include any technology that enables networked devices to exchange information. Consumer Electronic (CE) devices, such as smartphones, tablets, laptops, e-books or media players have annually increased in number of units since their introduction into the market. A recent study published by Cisco predicts that by the end of 2022, there will be 8,4 billion handheld or personal mobile-ready devices [36]. Figure 1-8 shows the increasing trend of M2M connections as well as the huge amount of used PD forecast.

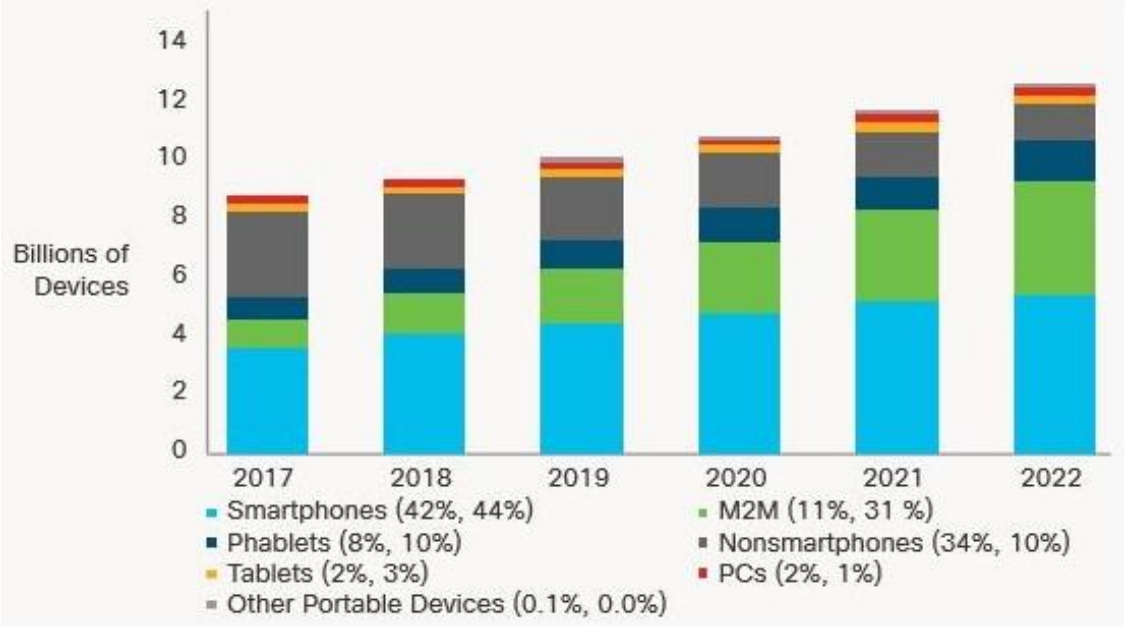

Figure 1-8. Global mobile devices and connections growth (extracted from [36]).

In the last 30 years, the development of more advanced CE devices has incredibly increased their energy consumption because [12]:

(i) they are used away from stationary power sources;
(ii) they are equipped with several numbers of applications and power hungry features;
(iii) they are used frequently.

Portable electronics are essential for our daily life; therefore, it is important to supply them with sufficient energy and to assure a long grid independency [16]. The production method should be cheap and sustainable, and it should also allow to integrate the power supply system within the device packaging.

Figure 1-9 represents a classification of the main PDs as a function of their operating power needed. Calculators or electronic watches are generally powered by Energy Harvesting (EH) and button batteries because less than 1 mW is required (ultra-low power regime). On the other hand, the devices which can provide 0,5-50W of power (low power regime) are frequently called micro power sources. In this field, batteries are nowadays responsible of powering most of the commercial CE devices (µP desktop, µP laptop, MP3, smartphones), [37].

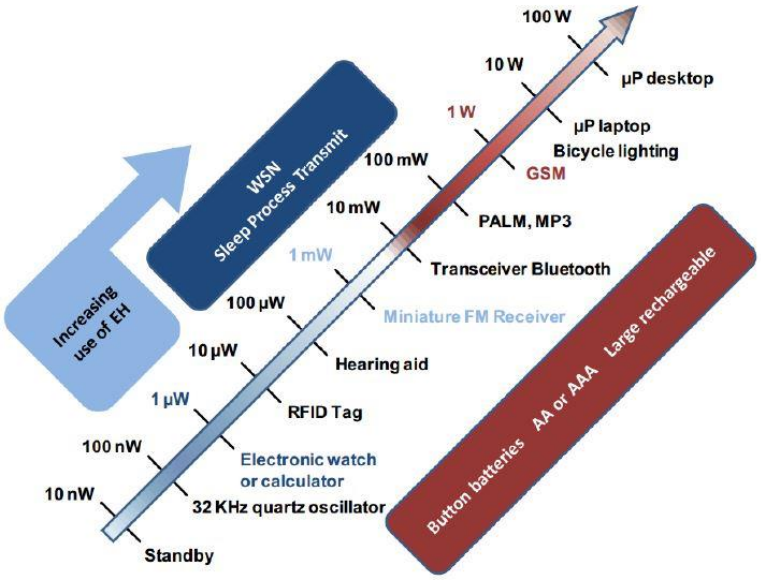

Figure 1-9. Power consumption of portable devices (extracted from [38]).

1.3.1 Limitations of batteries for new energy demands

Up to now, batteries have guaranteed smartphones autonomy (hours) with a regular wiring to the electrical grid for recharging. However, as the potential applications and functionalities increased, the need of power out-off-grid increased exponentially. Figure 1-10 illustrates the evolution of phones energy requirement in the last years as well as the battery energy capacity trend (Wh). The energy gap between the capacity of the current battery technology and the power requirements is increasing year by year [12]. According to this study, batteries are simply unable to meet this growing energy demand, since they have already reached their energy density limit. Therefore, the development of new technologies is needed and the main requirements to fulfil are:

- Possibility of miniaturization;
- High power and storage density;
- Long electrical grid autonomy;
- Low cost.

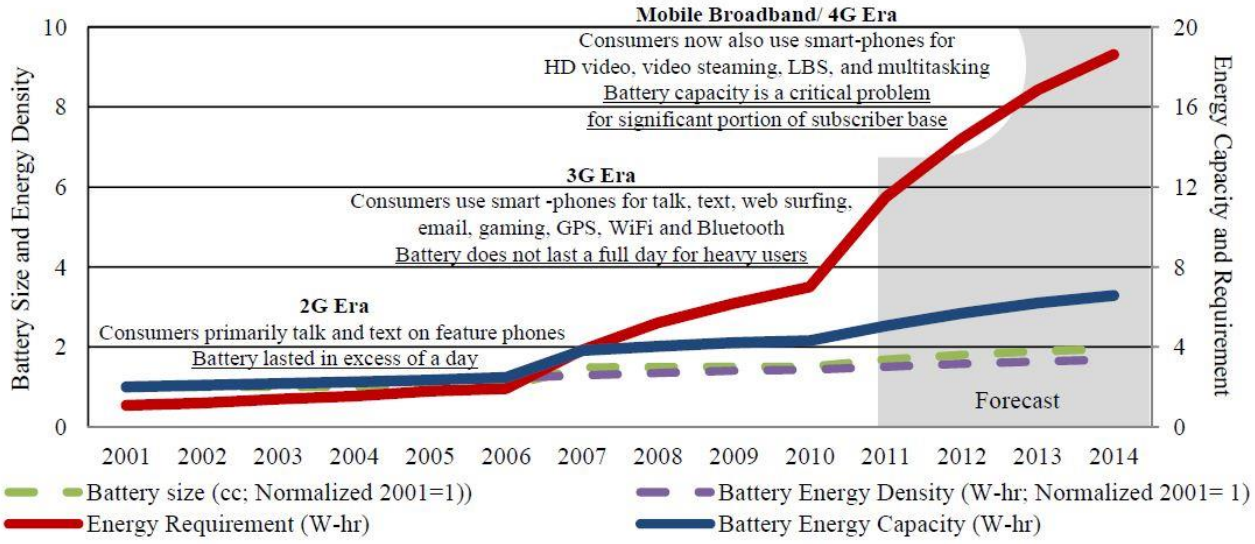

Figure 1-10. Energy needs and smartphones capacities evolution (extracted from [12]).

1.3.2 Micro fuel cells alternative

In the last decades there have been several efforts to develop a different power supplying system. Micro fuel cells appeared as one of the most promising alternatives, since they have higher energy density than batteries (up to three times Li-ion or nickel-metal hydride batteries), as shown in figure 1-11. Moreover, they have instant refill capability which allows longer out-off-grid autonomy.

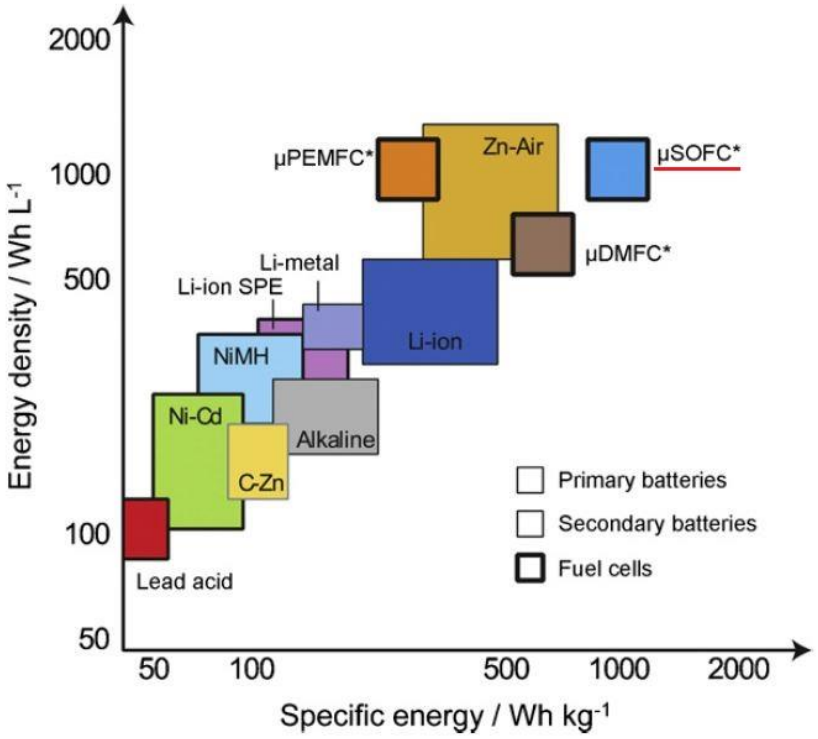

Figure 1-11. Specific energy vs. energy density of different powering technologies (extracted from [18]).

Micro-PEMFCs (µPEMFCs) and micro-DMFCs (µDMFCs) have already been used in some prototypes for portable applications due to their low-temperature operation (50-100 °C), but they require expensive Pt catalyst for efficient conversions. On the other hand, micro-SOFCs (µSOFCs) have higher specific energy and energy density compared to both µPEMFCs and µDMFCs. The operating temperature can be reduced as low as 350°C by reducing the electrolyte thickness and optimizing the material properties [18].
µSOFCs are based on the integration of functional free-standing electrolyte membranes in silicon technology, which ensures high reproducibility, cheap production and reliability [35]. In these systems, energy is stored in a fuel reservoir out of the cell body; the replacement of the fuel cartridge allows an instant recharge and guarantees autonomy from the electric grid.
Moreover, µSOFC are attractive also for the reduced size, the long lifetime, the quick start-ups and the possibility working with hydrocarbons.

As illustrated in figure 1-12, the main components and connections (block diagram) of a complete µSOFCs power generator (PG) are [35,39]:

1. A µSOFC stack for power generation (fuel cell module);
2. A fuel-processing unit (FPU) for hydrogen production from a hydrocarbon;
3. A catalytic post-combustion unit (CPU) for exhaust gas processing, producing H_2O;
4. A heat power management unit, consisting of some heat exchangers (HX) for air and fuel and thermal insulation (INS);
5. Balance-of-plant (BOP) components like a fuel cell controller, a power conditioning and a rechargeable battery or capacitor in order to manage the output power in steady and transition conditions;
6. Fuel and products cartridge.

The first five sections compose the hot module (HM) or micro-SOFC power unit. With the sixth the micro-SOFC power system is complete.

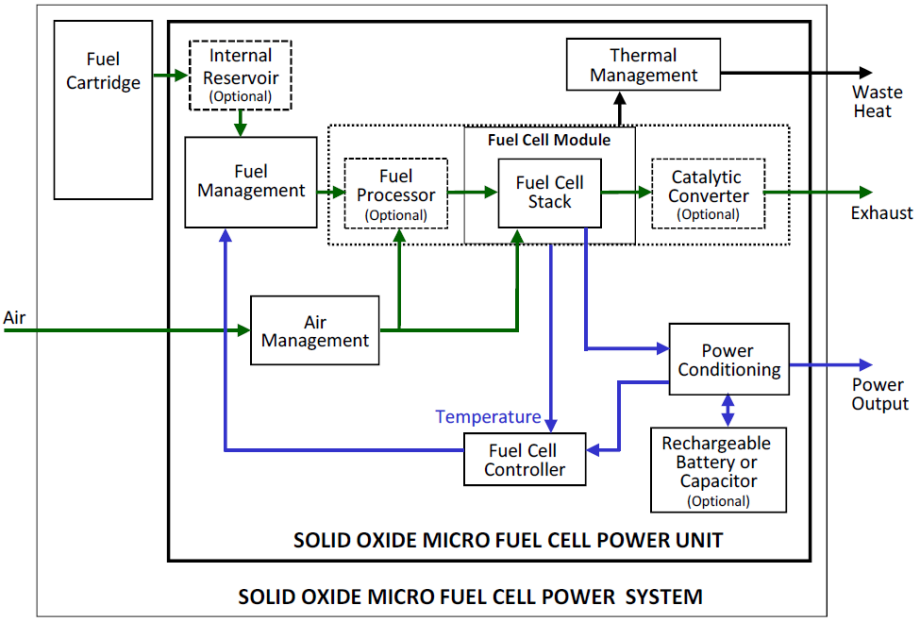

Figure 1-12. Hydrocarbon-based fuel cell system block diagram (extracted from [39]).

1.4 Ultra-SOFC project

This master thesis belongs to the *Ultra-SOFC project* [40], funded by the European Research Council (ERC) and developed by IREC (Catalunya Institute of Energy Research) and ICREA (Catalan Institution for Research and Advanced Studies) collaboration. The project aims to design an ultrathin portable power source based on stack of novel micro-SOFCs fully integrated in silicon.

The main limitation on μSOFCs development regards temperature restrictions, i.e. limited performances of the state-of-the-art electrolytes at room temperature (RT) or the difficulties related to quick start ups with low energy consumption at high temperature (HT ~ 650°C). The Ultra-SOFC project tries to break these limitations by taking advantage of the new opportunities in nanotechnologies. Employing thin film membranes with low-cost electrodes would allow a RT operation (with H_2), while a full-ceramic μSOFC integrated in a low-thermal-mass structure would permit the operation under HT conditions (with hydrocarbons).

Figure 1-13 shows the HT full ceramic membrane realized at IREC [40], which can provide 5W in a size of one-cent coin.

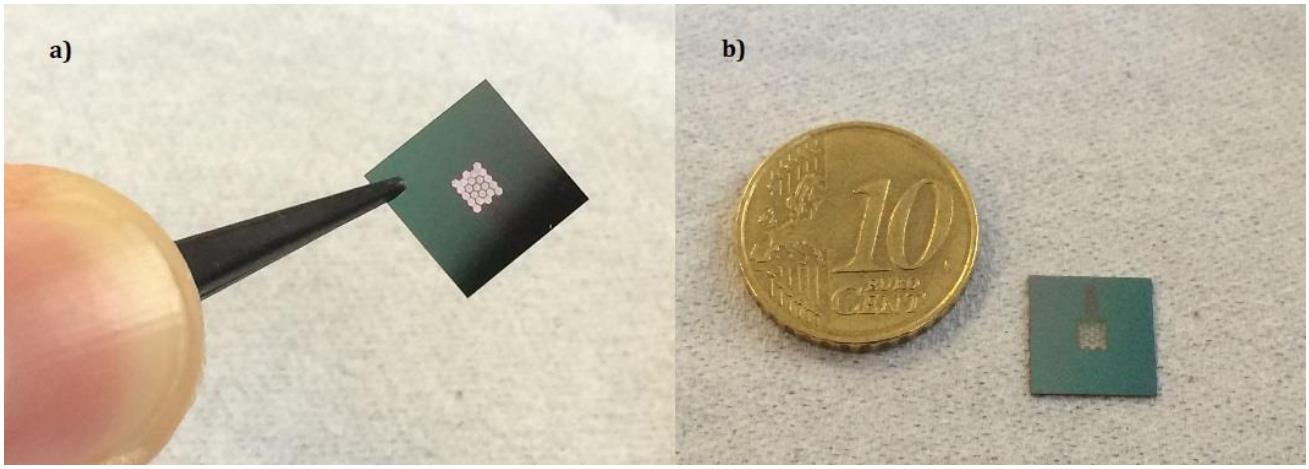

Figure 1-13 (a), (b). Size comparison of a single large-area μSOFC (extracted from [40]).

In this section, the microfabrication route of the full ceramic membrane and its materials are described as well as the stack configuration with the balance of plant (BoP) and thermal insulation analysis.

1.4.1 Device fabrication and balance of plant

The fabrication route of the free-standing low-thermal-mass large-area (active area is higher than 2 mm^2) membrane is briefly described in figure 1-14. Increasing the active area of the device is a key factor, which has been obtained by using a grid of doped-silicon slabs as mechanical support (free-standing structure). The main fabrication steps of the full-ceramic membrane are [22]: (a) photolithography, to define the Si-doped zones (supporting slabs), which will not be affected by anisotropic etchants; (b) SiO_2/Si_3N_4 dielectric layer deposition; (c)

selectively etching on the backside realising the Si_3N_4 layer of the topside; (d) PLD electrolyte deposition; (e) realising of the electrolyte layer with a backside RIE; (f) PLD electrodes deposition on both sides; (g) metallic films deposition with nanosphere lithography, as current collectors.

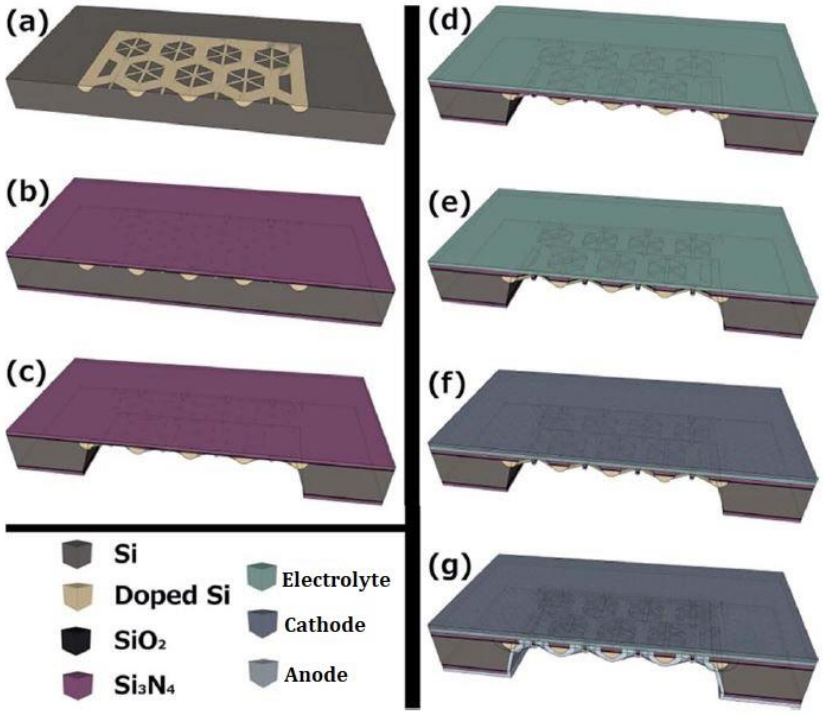

Figure 1-14. Main fabrication steps of the large-area µSOFC membranes (extracted from [22]).

The novel ceramic materials (compared to the µSOFC state-of-art, see chapter 1.2.2) deposited and tested until now for the *Ultra-SOFC* project, as competitive ionic conductors and MIEC are:

- Electrolyte: a thermally stable 8 mol% YSZ (8YSZ) thin film able to withstand different thermomechanical cycles [15]. Low electrical resistance (ASR = 0,15 Ωcm^2) is obtained at low temperature (400°C) with 250 nm thick free-standing membranes [22].
- Anode: a porous $Ce_{0,8}Gd_{0,2}O_{1,9-\delta}$ (CGO) thin film (250 nm). A very low conductivity in plane was measured (0,1 S/cm from 400°C to 700 °C) under reducing atmosphere. Therefore, porous Pt layer (150 nm) was added to increase the electrical conductivity and a symmetrical membrane was tested (Pt-CGO/YSZ/CGO-Pt) with an ASR of 0,30 Ωcm^2 at 700°C.
  Furthermore, thin films of $Sr_2Fe_{1,5}Mo_{0,5}O_{6-\delta}$ (SFM) have been evaluated in both oxidizing and reducing atmosphere, reaching the target value of ASR at intermediate temperature [17].
- Cathode: a porous $La_{0,6}Sr_{0,4}CoO_{3-\delta}$ (LSC) thin film (200 nm) revealing high electrical conductivity in plane (200 S/cm) with no degradation at high temperature [15]. LSC/YSZ/LSC membrane was fabricated and the required ASR of 30 Ωcm^2 has been reached at intermediate temperature (700°C).

Moreover, $La_{0,8}Sr_{0,2}Mn_{1-y}O_{3\pm\delta}$ (LSM) has been recently tested with good results, demonstrating the strongly influence of grain boundaries on the electronic and oxygen mass transport [41].

Once the membrane is fully optimized in terms of thermomechanical stability, electrochemical performances and material compatibility, a μSOFC stacks implementation with the balance-of-plant (BoP) elements is necessary. The design of the complete system is represented in figure 1-15. Basically, it consists of three parts [35]:

1. Fuel processing unit (FPU): it is composed by a μ-vaporizer and a μ-heater, whose total active area is increased thanks to micro-pillars; then, two different μ-reformers in series are necessary in order to satisfy the H_2 production from hydrocarbons in steady state (bulk μ-reformer) and transient conditions (suspended μ-reformer); finally an HOYA glass is set between the reformers to reduce the start-up time by insulating the FPU;
2. μSOFC stack: tens of μ-SOFC cells vertically stacked, connected electrically in series and fluidically in parallel. A sealing material is used to bond the cells to each other;
3. Post-combustor unit (CPU): a catalytic μ-post combustor unit allows the almost complete conversion of hydrogen into water and carbon oxides. The heat produced by the reaction is recovered by the system.

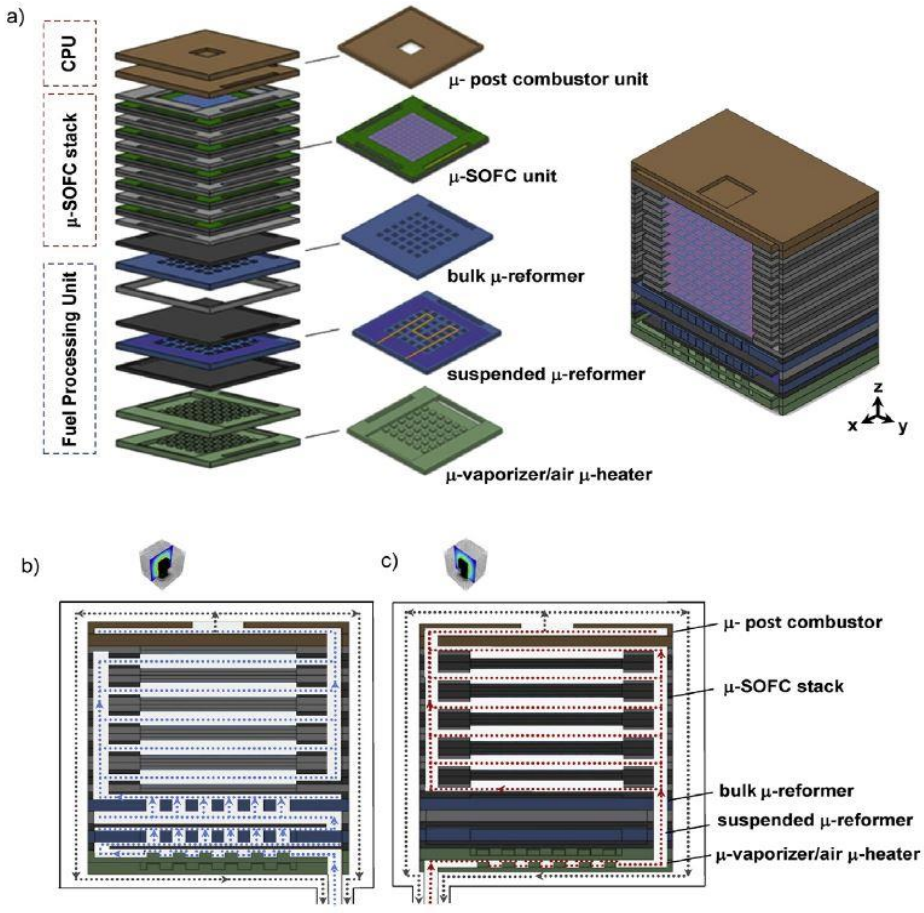

Figure 1-15 a) Layout of the different elements of a vertically stacked hot module of μSOFC PG; (b), (c) Orthogonal cross-section schemes of the PG showing the flow pathways of fuel (blue) and air (red) respectively (extracted from [35]).

Figures 1-15 (b) and (c) show the fuel and air pathways, highlighting how these fluids are kept separated until the CPU, where H_2 burns and generates a recovery heat for the system.
Since the device needs to operate at intermediate temperatures (500°C – 700°C), an external insulation (INS) is fundamental for safety reasons. A Computational Fluid Dynamic model (CFD) was adopted to simulate the steady-state and transition operation mode. Dolors Pla et al. [17, 35] determined a start-up time around 55 s, (after which the μSOFC PG is fully operative) and ca. 13 min to reach the steady-state condition (switching off the heaters). The required material for the insulation would have a thermal conductivity (k) as low as 5 $mWm^{-1}K^{-1}$ and 10 mm of thickness.
Despite the innovative results on microfabrication and μ-SOFC integration with the balance-of-plant, there is still need of improvements, mostly regarding the reliability of the entire system. Next section will introduce the main goals of this thesis work.

1.4.2 Integration of MEMS technology and novel thin film anode

There are few publications regarding thermo-mechanical stability tests on membranes and μ-SOFC stacks [15, 22, 25, 27, 31]. Indeed, there are still some issues to solve prior to the future commercialization of these devices; they can be resumed as:

- The need of high temperature multi-chip **sealing** [12]. Due to several thermal cycles required, severe thermal expansion stresses must be withstood. If dissimilar materials were used, a significant mismatch with their CTE could occur, causing the cell breaking. Since silicon is the main substrate material used, the CTE of each component must be comparable to the silicon one [12].
  Moreover, the sealing integration of multiple silicon-based component must be tight and hermetic. In fact, issues related to leakage control and connection of μ-SOFC modules decrease significantly the theoretical OCV and hence the maximum power output [16]. Finally, since the sealing material works in both oxidizing and reducing atmospheres, it must be stable in both environment in a big range of temperature, from RT to 700°C, [12].

- The presence of **pinholes** in the electrolyte of silicon-based free-standing μ-SOFC [16]. They are generated due to dust and particles accidentally depositing and creating shadow effects during the growth of the film [16]. The appearance of pinholes on a YSZ membrane provokes failure of the cells by shortcutting the two electrodes. In the case of large membranes, even a single pinhole can detrimentally affect the performance of the entire system. The probability of failure is lower for smaller areas, favouring small membranes for μ-SOFC applications [18], but the corresponding low power production (due to a smaller active area) decreases their consideration.
  In order to solve this issue, some practical solutions could be adopted: (i) pre-cleaning of the substrates to avoid shadowing effects by dust particles; (ii) making use of dense and thermomechanically stable targets, to reduce particle ejection while depositing; (iii)

performing a multi-step deposition to clog the nano-pinholes, possibly by atomic layer deposition (ALD), [5].

- The lack of studies devoted to the development of **thin film anodes**. Indeed, Pt anodes cause several stability and degradation troubles. Two main strategies are considered to fabricate more reliable thin film anodes: (i) implementation of cermet based on stable ceramic scaffolds; (ii) the use of more stable **fully ceramic anode** materials [22]. Moreover, to improve the performances it is necessary to increase the density of active electrode sites and/or to use more catalytically active materials [12]. Properties of thin films are rather different from those of bulk materials [18]. The thermal and mechanical stability, chemical compatibility during preparation and operation, reliability and electrochemical performance of microfabricated μ-SOFC membranes are scale dependent properties, and hence the structural design of the electrochemical active membrane must be configured carefully [18].

- Economic considerations, such as the capital cost. Ensuring a batch production by adopting the well-known microfabrication technology on silicon is a key factor [15].

This work aims to develop innovative solutions in μ-SOFC state-of-art to increase the reliability of the entire system. As shown in figure 1-16, two main fields of study have been considered:

1. **Study of glass-ceramic sealing for MEMS:**
   To guarantee a perfect device encapsulation and keeping two environments (reducing and oxidizing) completely isolated, this project has focused on the deposition of a material able to resist at high temperature and in harsh conditions. The sealant needs to match the thermal expansion coefficient (CTE) of the silicon and to be an electric insulator, to avoid short circuit with the electrical connections integrated in the device. For this purpose, the chosen material is based on glass-ceramic material, which is applied on the device as a paste of glass frit. Figure 1-16 represents a cross-section of a possible final design and the application of the sealing glass between two silicon wafers. It is important to underline that the deposition of this sealing paste must be carefully managed in order to obtain a controlled fine-line and smooth deposition that will create gas chambers of desired dimensions.

2. **New ceramic anode characterization:**
   To overcome the issues related to Pt anodes, a novel thin film ceramic material has been tested as μSOFCs anode. The perovskite $La_{0,3}Sr_{0,7}TiO_3$ (LST37) anode has been chosen from a direct analogy of the bulk SOFC materials. Being a ceramic composite, it should guarantee thermo-mechanical stability in the whole range of operating temperature. Moreover, it should be catalytically active towards H_2 and compatible with the electrolyte used, YSZ. Another important characteristic is the dual electrochemical behaviour, being electronic and ionic conductor (MIEC), hence extending the electrode active area. A highly

porous thin film would increase the TPB (three-phase-boundary), enhancing the electrochemical performances. A typical target value of ASR is 0,15 Ωcm^2, which should be reached at intermediate temperature according to the other cell materials [15, 17, 22].

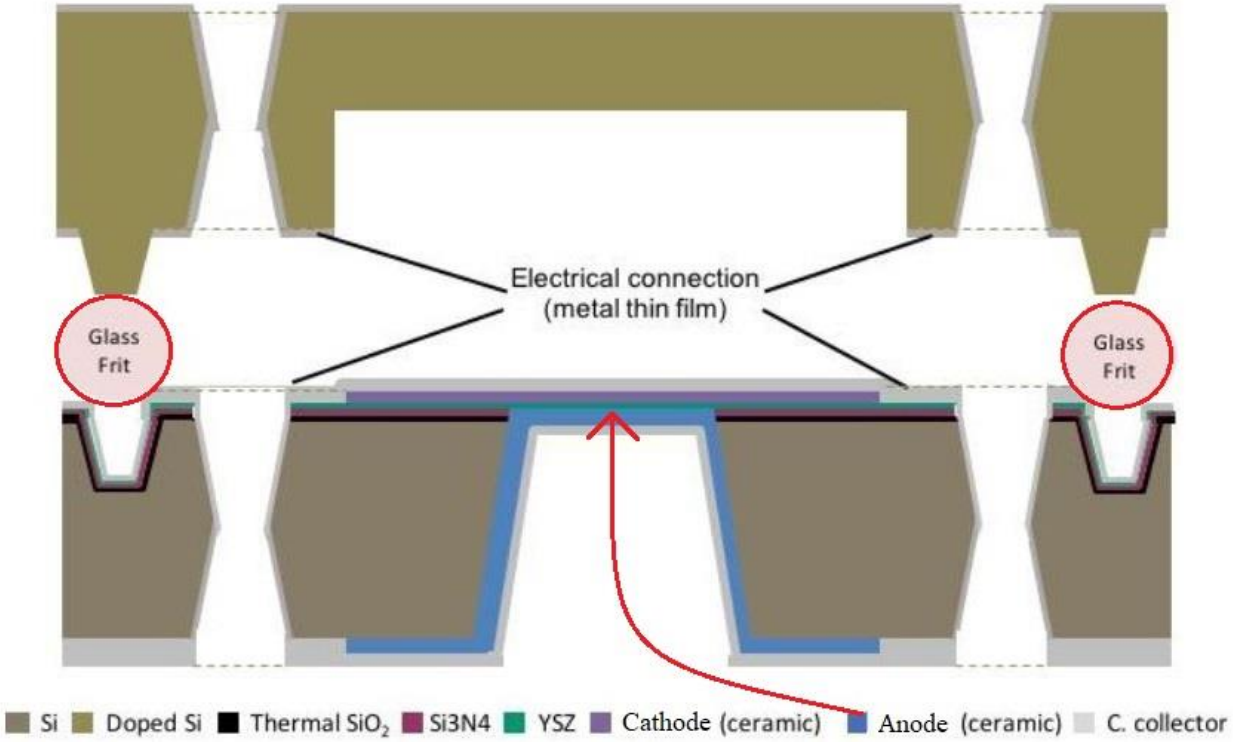

Figure 1-16. Schematic cross-section representation of the µ-SOFC, showing the glass frit application and the anode deposition.

In the following chapters, the complete routes of characterization of both studies will be developed:

I) First, the state-of-art of anodes and main bonding used for µ-SOFCs are proposed with the characteristics to be satisfied;
II) Furthermore, the experimental method adopted is described with the corresponding instruments used;
III) Finally, the main conclusions are resumed by matching the different results obtained.

2 STATE OF THE ART

2.1 Joining techniques

A joining process is used to mechanically fix two or more chips/wafers to each other. In this way it is possible to obtain three-dimensional devices by integrating different components. Moreover, it allows high flexibility of the process and a controllable chamber environment (pressure, gasses). Generally, the joining surfaces must be co-planar, flat, clean and mirror-polished [42]. Bonding technologies are commonly differentiated in two groups: *(i) Direct bonding*, like fusion bonding, anodic bonding, plasma enhanced bonding; *(ii) Indirect bonding* (an intermediate layer is used), like adhesive bonding, thermo-compression bond, solder bonging, eutectic bonding and glass seal bonding. Table 2-1 resumes the main wafer bonding techniques.

Table 2-1. Different types of wafer bonding techniques (matching [42, 43, 44, 45, 46, 47, 48, 49]).

Wafer bonding technique	Bonding conditions	Advantages and disadvantages	Applications
Fusion bonding [42, 44]	800-1100°C Small or no bond pressure	+} High bond strength, hermetic, high temperature resistant; -} High surface flatness required, high bond temperature.	Silicon-on-insulator (SOI) wafer fabrication
Anodic bonding [17, 42]	180-450°C 200-1000 V No bond pressure	+} High bond strength, hermetic, high temperature resistant; -} High temperature and high voltage not always compatible with electronic wafer.	Sensor packaging
Plasma enhanced bonding [42]	RT-150°C Plasma treatment	+} Hermeticity with annealing; -} Thermal void generation, need to investigate the impact on electrical properties.	SOI wafer fabrication
Adhesive bonding [42]	RT-350°C Low to moderate bond pressure	+} High bond strength, low temperature, it works with any substrate material; -} No hermeticity, limited temperature stability.	MEMS. Sensor packaging. Temporary bonds
Thermo-compression, metal-to-metal bonding [42]	200-400°C 100-800 MPa High bond pressure	+} Hermetic, compatible with electronic wafer; -} Very high-pressure bonding and high surface flatness required.	Wire bonding. Bump and flip-chip bonding
Solder bonding [42]	150-450°C Low bond pressure	+} High bond strength, hermetic, compatible with electronic wafer; -} Solder flux.	Bump and flip-chip bonding
Eutectic bonding [42]	200-400°C Low to moderate bond pressure	+} High bond strength, hermetic, compatible with electronic wafer; -} Sensitive to native oxide at surfaces.	Hermetic packaging. Bump and flip-chip bonding
Glass frit bonding [45, 46, 47, 48, 49]	400-1100°C Low to moderate bond pressure	+} High bond strength, hermeticity; -} Bond temperatures not always compatible with electronic wafers.	Sensor packaging. SOI wafer technology

In MEMS, the packaging protects the sensitive internal structures from the influences of the environment, such as moisture, temperature, pressure and oxidizing species. Therefore, the long-term stability and reliability of these devices depends on the encapsulation process, which must satisfy these requirements: (i) protection against environmental influences; (ii) heat dissipator or insulator (depending on the purposes); (iii) integration and compatibility with different materials; (iv) hermeticity.

Fusion bonding is based on intermolecular interactions, including Van Der Waals forces, hydrogen bonds and strong covalent bonds [44]. Depending on the joining surfaces and the bond strength wanted, the temperature can be raised up to 1100°C, causing some technological issues. In fact, the surface energy between the bonded wafers is strongly dependent on the annealing temperature [42]. Furthermore, a deep cleaning from impurities is mandatory [44].

Anodic bonding uses an electric field (200-1000 V), temperature (180-450°C), no mechanical force, under vacuum or atmosphere pressure [42]. It is usually adopted to bond glass wafers and metals or Si wafers. In this case, the CTE of the substrates must be comparable (for instance, glasses from HOYA OPTICS are commonly designed to be bonded with Si). At moderate temperature, the glass becomes a conductive solid electrolyte and the high electrical field between silicon and the glass results in an electrostatic force that pulls them into intimate contact, resulting in an oxidation procedure, to form covalent bonds [42]. Figure 2-1 shows the ions migration during the anodic bonding. The advantages are reasonable low process temperature, low residual stress, hermetic seal and less stringent requirements on surface quality than fusion bonding. However, for microfabrication processes, the need of absolutely clean and smooth surface limited the application of this type of technique.

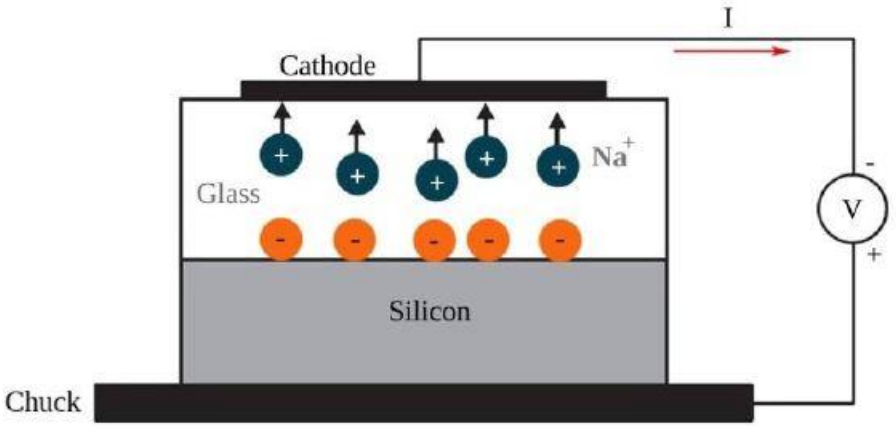

Figure 2-1. Anodic bonding fundamentals between glass and silicon (extracted from [17]).

Plasma enhanced bonding (for instance, Reactive Ion Etching, RIE) shows an increasing bond strength of fusion bonded wafer at RT. A wide variety of materials can be bonded to each other using low temperature plasma enhanced wafer bonding, such as Si, SiO_2, glass, quartz and sapphire [42]. Despite the advantages related to a low-temperature operation and high bond strength, some drawbacks are still challenging such as thermal void generation; besides, the impact of the plasma treatment on the electrical properties of the bonded surfaces is still unclear [42].

The previously described methods are called *direct bonding methods*, because no intermediate layers to bond two substrates are needed. On the other hand, several *indirect bonding methods* are used in MEMS technology and Integrated Circuits (IC), as described below.

Adhesive bonding uses polymers, allowing a free choice of wafer material with different CTE [42]. These materials are mainly deposited by spinning (obtaining uniform coating), then patterning by lithography and annealing at low temperature (below 350°C) to form low-stress stack with quite good bond strength [42]. Polymer bonding does not produce hermetic seal, so they required an additional metallization step. However, they are quite used as temporary bonding.

Solder, **Eutectic** and **thermo-compression bonding** are included in the **metallic bonding** group. They have the advantages of achieving easily a hermetic seal, using medium process temperature (200-400°C) and high bond strengths (up to 20 MPa), but there are demands on wafer topography and the realisation of electrical feedthroughs may be difficult [42]. Au-Si compound is usually considered as the most promising combination for the eutectic bonds, because of its low eutectic temperature. However, it is difficult to obtain a large bonding area. Au-Au thermocompression bonding takes place at 300-400°C and pressures of 10 to 800 MPa, obtaining strong bonds, but with possible thermomechanical issues.

Finally, **glass seal joining** is the last indirect method for wafer level encapsulation and packaging. The glass seal is a viscous paste consisting of glass powders, an organic binder, inorganic fillers and solvents. The Seal based glass is usually deposited on the cap wafers and then heat treated by applying pressure. The glass material softens during the thermal treatment and wets the surfaces. After cooling down process, a continuous hermetic bond is then formed between the two surfaces [45].
The advantages of this joining technique can be resumed as follows:

- Simple process technology;
- Connection of different type of materials;
- Bonding of rough surfaces;
- No voltage required;
- High bonding yield;
- Hermetic encapsulation;
- Easily workable at room temperature;
- Chemically inert (it depends on the interaction with Si substrate).

For all these reasons the glass sealing has been chosen as a primary candidate to ensure the encapsulation at high temperature for the μ-SOFC system. At the same time, it should allow the access for the gases (oxygen and hydrogen) through micro channels, requiring thus a very well controlled deposition technique that could easily be adapted to different shapes. Finally, an important advantage is the possibility of using metallic wires passing through the bond and still ensuring gas tightness.

2.1.1 Glass seal joining and its integration on µ-SOFCs

Glass-based sealing technique is based on glass technology. Figure 2-2 illustrates the route of glass ceramic formation starting from a glass. Borosilicate, boron-free alkaline earth silicates and phosphor-silicate glass-ceramics are commonly used for making SOFC seals [2] conferring different properties. As defined by the *American Society for testing Materials (ASTM)*, the glass is "an inorganic product of fusion which has been cooled to a rigid condition without crystallizing". It has an amorphous structure i.e. atomic disorder as evidenced by an x-ray diffraction (XRD) analysis.

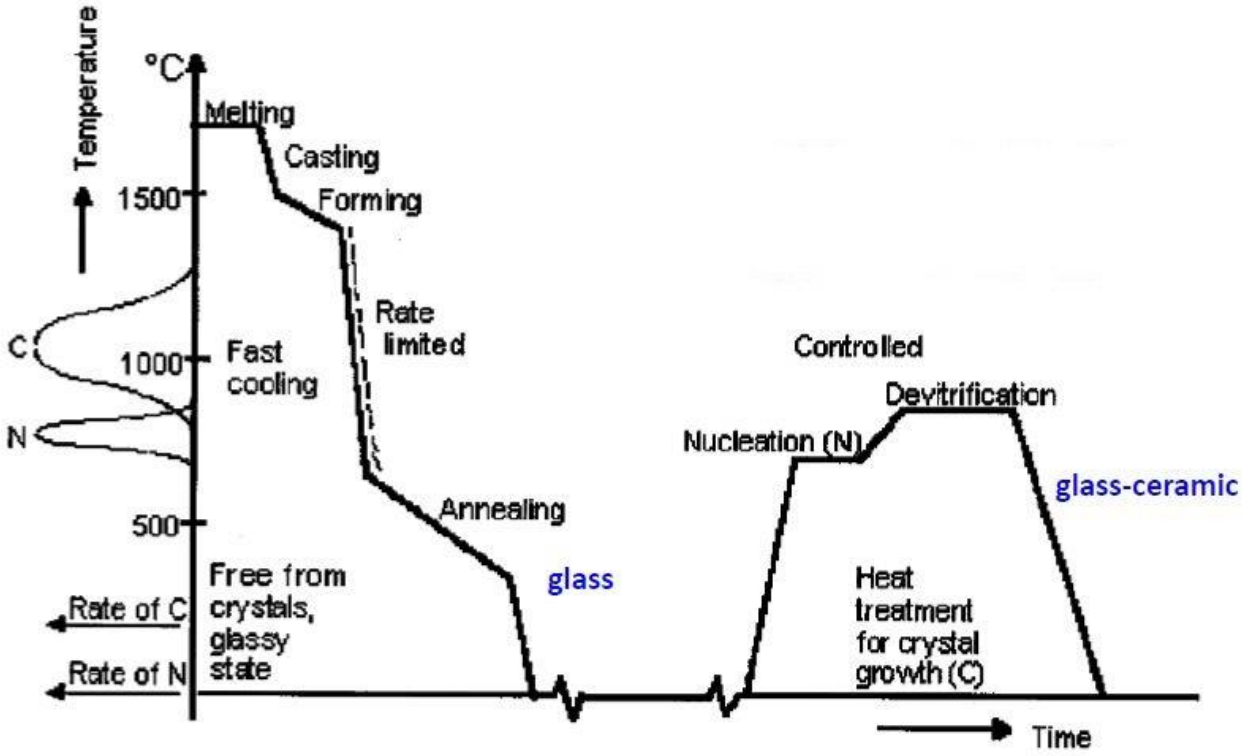

Figure 2-2. From melting glass to glass ceramic formation (extracted from [46]).

Each glass is characterized by a V-T diagram (see figure 2-3) which establishes the necessary cooling rate to adopt in order to obtain a *glassy state*, where the molecular groups have not completely rearranged their volume at the specific temperature.

The softening and the working temperatures described above are characteristics of each type of glass, but the fundamental one is the **glass transition temperature** T_g. The intersection of the extrapolated super cooled liquid line and the fast cooling line on the V-T diagram (figure 2-3) represents the glass transformation range, where the glass viscosity is of the order of 10^{12} Pa·s.

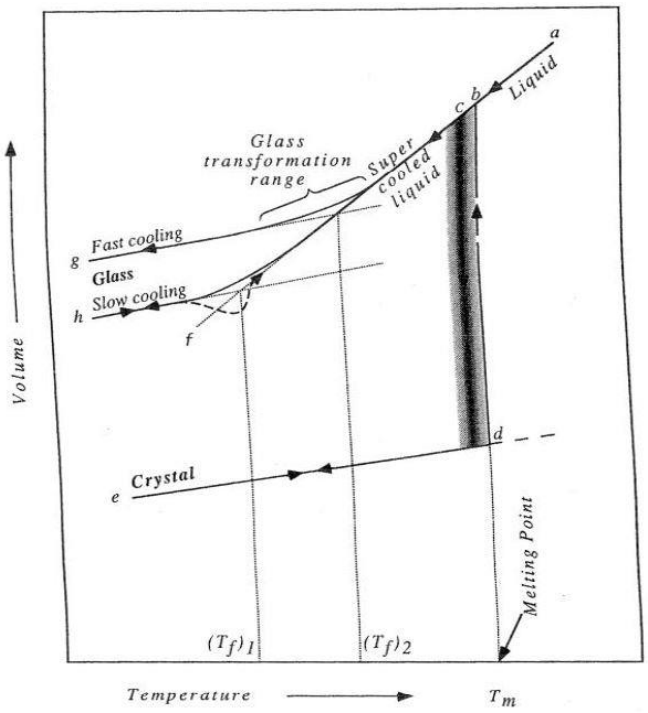

Figure 2-3. Volume-Temperature diagram, glass transformation range (extracted from [47]).

The process of glass formation is described by two types of theories: (i) **structural theories** and (ii) the **kinetic theory** [47].

Zachariasen's theory belongs to the first group. It describes the relative glass-forming ability of oxides and it states that a substance can form extended random three-dimensional networks lacking periodicity but with energy comparable with that of the corresponding crystal networks. Accordingly, he laid down the rules for glass formation in a compound A_mO_x [47]. Based on single-bond strength (τ), it is possible to identify three types of oxides groups: (i) *glass formers* with $\tau > 80$ kcals (e.g. Silica, Germania, Boron and Phosphor oxides, …) which form the basic amorphous network; (ii) the *intermediates,* with 60 kcals $<\tau<$ 75 kcals, which do not form glass alone, but in a limited amount they can take part of the glass former amorphous network (Alumina, Zirconia, Titanium oxide, …); (iii) the *modifiers* with $\tau<$ 60 kcals (e.g. alkali oxides, earth-alkali oxides, zinc oxides, …) which can cause a breakdown of the network and hence reducing the characteristic temperatures.
The kinetic theory states that all liquids can be vitrified with a suitable cooling rate rapid enough to avoid crystallization (also called devitrification) below the freezing point [47]. There are two types of nucleation: homogeneous and heterogeneous. The former occurs away from a surface while the latter occurs at nucleation sites on surfaces in the system.
The key of making a successful glass-ceramic is the control of the nucleation and crystallization process.
In general, the **glass-ceramic** process (glass-ceramic devitrification) enhances the mechanical properties of a glass, because of a very uniform particle size distribution and near-zero porosity [47]. The common nucleating agents are TiO_2, ZrO_2, fluorites, phosphates, Ag, Au, etc. From them, a homogeneous nucleation usually occurs, then they become sites for heterogeneous nucleation for other crystalline phases to growth.

The glass-ceramic process changes the thermal and physic properties, for instance the viscosity, the CTE and the characteristic temperatures.

The viscosity is the inverse of fluidity and it is a measure of the resistance to shear deformation with time. The time rate of deformation ($\dot{e}$) is linearly related to the shearing stress through Newton's law of viscosity:

$$\sigma_{xy} = \eta \dot{e} \qquad (2.1)$$

Where η is the coefficient of viscosity (measured in Pa·s). The viscosity is strongly dependent on temperature (T). The η-T relationship is weak at high temperature (around 1500°C) where the viscosity has not relevant changing (around 10 Pa·s in the melted stage). As the temperature decreases, the viscosity increases of several order of magnitude. At around 750°C, a typical soda-lime glass reaches the **softening point** ($10^{6.5}$ Pa·s), at which the mass would slump under its own weight [47]. With a value of η higher than 10^{15} Pa·s, it is difficult to distinguish the glass from a solid form.

A fundamental parameter related to the glass operation during thermal cycles is the thermal expansion coefficient (CTE). The volume expansion coefficient can be expressed by:

$$\beta_m = \frac{V_2 - V_1}{V_1(T_2 - T_1)} \qquad (2.2)$$

Where V_i is the volume at temperature T_i. The corresponding linear expansion coefficient (α or CTE) is obtained by replacing the volume V with the length L, and it is usually measured in K^{-1}. The dilatometry measurement is one of the experimental methods used to obtain the CTE values. Exposing a glass product to a sudden change in temperature and observing whether the glass fails or not is the basis of **thermal shock** test. A high CTE is a negative contribution of the thermal shock resistance (TSR) which can be approximated by the following formula:

$$TSR \cong \frac{\sigma_f k}{E\alpha} \qquad (2.3)$$

Where σ_f is the flexural strength, k is the coefficient of thermal conductivity, E is the elastic module and α the CTE.
In general, it is always possible to control the previous described properties (viscosity, CTE, characteristic temperatures) by a proper choice of the glass components and the glass-ceramic process. Anyway, finding a good composition and a suitable thermal treatment is not immediate. The idea of the glass sealing joining applied to a μ-SOFC membrane is to deposit a layer of a glassy paste between two wafers ensuring wettability and thermal compatibility with various substrates, such as silicon with hydrophobic and hydrophilic surface, silicon dioxide, silicon nitride, aluminium, titanium. Before the deposition, the glass must be transformed into a viscous paste. Therefore, it must be reduced in powder with a ball milling process and mixed with an organic binder forming a printable paste [45]. It is interesting to notice how the particle size could change some glass-ceramic properties. Smeacetto et al. [48] proved that decreasing the

particle size of a barium-free silica-based glass sealing would shift the crystallization peaks, obtained with a DTA analysis (Differential Thermal Analysis), to lower temperatures. This result could be associated with surface crystallization of the glass.
Adding some fillers could vary the properties of the melted glass paste. During thermal conditioning of the glass paste, the organic binder must be burned out, hence it is usually heated to an intermediate temperature, where the glass does not yet fully melt, to allow outgassing of the organic additives. Reaching the "melting temperature", a compact glass without any inclusions and with the fillers incorporated is formed [45]. To ensure the alignment accuracy during the bonding, a mechanical pressure (depending on the design) is applied on the soft material without any electrical biasing. This process guarantees a good wettability i.e. a complete covering of the wafer surface with glass.

There are several types of deposition methods and each one differs for its precision and controllability. For instance, the electrophoretic deposition (EPD) from an aqueous suspension containing glass powders has been used [48]. Slurry coating is a common and simpler way than EPD to deposit a glassy paste, but it could be less precise and difficult to optimize [48]. However, screen printing is probably the most used technique [45]. It derives from serigraphy and it is a space controlled deposition onto a substrate, by using a mesh, which is impermeable to the material. A blade is moved across the screen to fill the open mesh apertures and then with a reverse stroke the excess material is pulled out of the mesh. Without doubts, screen printing technique can guarantee a fine line deposition and a controlled height of the paste but for the sensible application we are dealing with, it could be disruptive. In this work a liquid deposition modelling (LDM) has been adopted. It is an additive deposition, layer by layer, and its shape, height and width can be controlled by a software [78]. A complete description of the system and its implementation on our purpose is deeply described in chapter 3-1 and 4-1.
Figure 2-6 shows the schematic diagram of the glass sealing bonding substrate. The micro-etching steps have allowed the formation of grooves which do not permit the glass spreading, and the walls can control the height of the deposited paste.

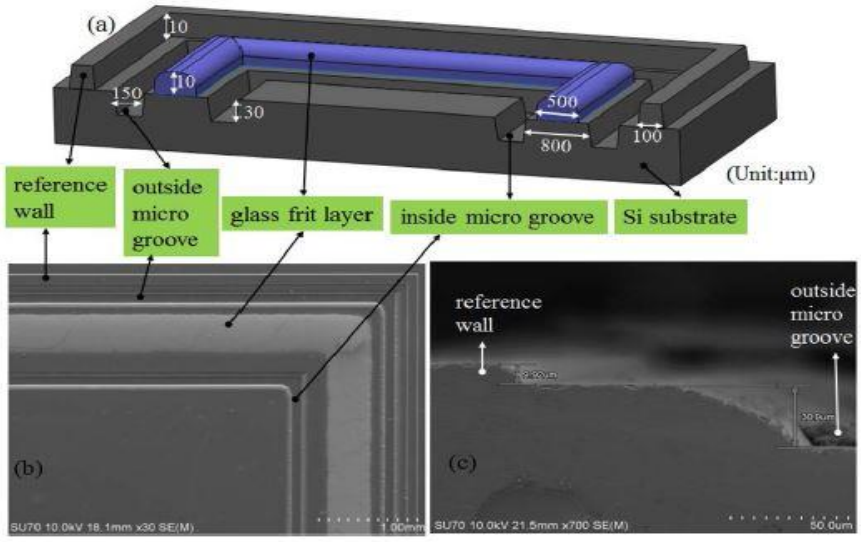

Figure 2-6. a) Schematic diagram of the substrate; b) top view of SEM image on the bonding structure; c) cross-sectional SEM view of height reference walls and grooves (extracted from [49]).

Even though the glass sealing technology is adaptable to different systems and its characteristics could be designed, there are some considerations to take into account: the CTE must be compatible with the other components, especially in these kinds of systems characterized by several thermal cycles; some oxides (e.g. SiO_2 and B_2O_3) could form volatile species at high temperature, which could react with other materials [2]; the lack of MEMS hermeticity testing standards do not assure an intermediate bonding checking, except on the final device which is not fully developed yet.

2.2 Thin film anodes for micro-SOFC

Platinum is the state-of-art of thin film anodes for micro-SOFCs but, as explained in section 1-2, the use of stable, fully ceramic anode materials is the most promising on-going strategy to allow chemical and thermal stability and hence durability of the device. Among the different stability requirement, anode materials must be able to handle fuel flexibility, tolerating carbon deposition and sulphur poisoning is mandatory. Also, anode materials must be stable in a wide oxygen partial pressure (pO_2) range [53]: in the low-oxygen pO_2 with the fuel inlet gas as well as in the more oxidizing conditions at the fuel outlet. Considering the thermal stability, a minimal CTE mismatch with other adjacent components is preferred.
Anode materials must also fulfil many different electrochemical requirements, such as enough electrocatalytic activity with H_2, high surface exchange kinetics and high electrical (≥100 S/cm) and ionic conductivity. In-plane conductivity and electrochemical impedance spectroscopy (EIS) measurements are used for thin films characterization as deeply described in the next chapter (section 3-2).
One interesting approach to replace platinum is to introduce a MIEC perovskite oxide (general formula ABO_3) whose structure is shown in figure 2-5.

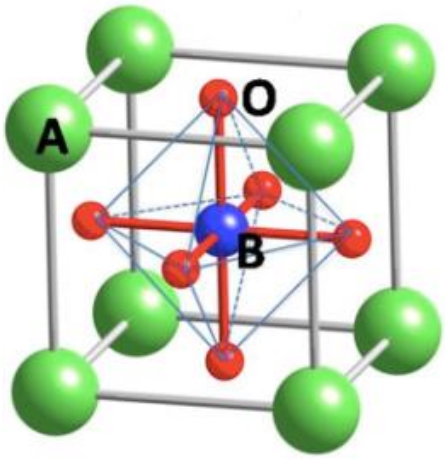

Figure 2-5. Perovskite structure ABO_3 (extracted from [51])

Perovskite materials have the B-element centred among oxygen atoms placed in the face centres and the A-element on the corners. This crystalline structure displays a large flexibility in the relative occupancy of the cationic and ionic species. Indeed, perovskites oxides exhibit oxygen excess ($ABO_{3+\delta}$), oxygen deficiency ($ABO_{3-\delta}$), and A-site deficiency ($A_{1-x}BO_3$), where A is a large radius cation and B a small radius cation [52]. One of the most interesting aspects of the perovskite structure is the possibility of doping both A and B site with different aliovalent atoms, which may give rise to the creation of charged defects for electronic compensation (e.g. oxygen vacancies, electronic holes and electrons), facilitating electrocatalytic processes and providing mechanisms for electronic conductivity [52]. In particular, when a perovskite oxide present both electronic defects and mobile oxygen vacancies, they behave as MIEC materials, able to conduct both oxygen anions and electrons (or holes) inside the crystal.
When a MIEC is used as electrode in SOFC, the active area may ideally extend to the whole material's surface, greatly enhancing the device electrochemical properties. This can also avoid

the undesired effect of electrolyte electrical constrains, because its active surface assures a homogenous distribution of the ionic conduction [16].
As regards the micro-structure, MIEC anodes should be porous in order to allow enough gas exchange at the gas-anode interface. Clearly, the choice of deposition method has an influence on the crystallinity and the microstructure of the thin film. Both vacuum deposition methods, such as sputtering and PLD and non-vacuum deposition techniques, such as ALD and spray pyrolysis, are frequently used. Non-vacuum methods usually result in amorphous thin films which can be transformed into crystalline films via annealing; vacuum methods usually lead to crystalline thin films forming during deposition already. The microstructures are mostly bricklayer-type for non-vacuum methods and columnar following the annealing of vacuum-deposited thin films [18].
Porous ceramic thin films can be easily deposited by PLD with an annealing process and a high background pressure during the whole deposition. The increasing of temperature causes an opening of the structure porosity, which is desired to increase the active surface [16]. The high pressure deposition decreases the mobility of species on the ablation plume and allows the formation of separated clusters that generates a porous network [22].

In section 1-2, table 1-3 resumes the performances and materials of the main research groups dealing with micro-SOFC fabrication. Therefore, it is evident the lack of study on thin film anodes, since platinum deposited with sputtering is often adopted. Cermet materials, for instance Ni-YSZ [34], have been used and tested in a membrane, but as in the bulk SOFCs, these types of materials cause carbon deposition at high temperature when hydrocarbons are used as fuel. Although complex ceramic oxides present lower anode performance than cermet materials (when tested in bulk SOFCs) there exist some promising options apparently suitable for their transferability to thin film. For instance, ceria-based oxides (Gadolinia-doped, CGO, or Samaria-doped, SDC) commonly used in SOFC technology for their high ionic conductivity, have been tested also in thin film applications [15]. I. Garbayo et al. [15, 22] fabricated a porous $Ce_{0,8}Gd_{0,2}O_{1,9-\delta}$ (CGO) thin film deposited over a dense YSZ film electrolyte. Anyway, a low electronic conductivity in the IT range limits the applicability of CGO as a full ceramic anode for micro-SOFCs. Therefore, CGO-Pt cermet was alternative fabricated and demonstrated its applicability as anode thin film thanks to good electrical and electrochemical performances at 700°C.
By a direct comparison with bulk SOFCs, other oxides such as chromites ($Sr_{1-x}La_xCrO_{3-\delta}$), titanates ($Sr_{1-x}La_xTiO_{3-\delta}$) and molybdates ($Sr_2MgMoO_6$) or their derived B-site doped materials are considered as the most promising thin film anodes for the next future. Since properties of thin films are rather different from those of bulk materials, big research efforts are necessary. PLD has been proven to be highly effective for depositing thin films with tuned microstructures. Therefore, this works aims to study and characterized a novel thin film anode, lanthanum-doped strontium titanite, deposited with PLD technique.

2.2.1 LST thin film anode

The perovskite $La_{0,3}Sr_{0,7}TiO_3$ (LST37) anode has been chosen from a direct analogy of the bulk SOFC materials. Several groups indicated that strontium titanate based materials ($SrTiO_3$) possess certain advantages over the Ni-YSZ cermet anodes, as phase stability in a wide pO_2 range, as well as resistance to coking and sulphur poisoning [13, 54]. Indeed, it was shown that an LST-based anode can operate without significant degradation with sulphur contents as high as 5000 ppm [55].

The average thermal expansion coefficient of $SrTiO_3$ (STO) calculated in the temperature range 50-1000°C is $10{,}8 \cdot 10^{-6}$ K^{-1} [53]. While the CTE measured for $La_xSr_{1-x}TiO_3$ is between 11 and $12 \cdot 10^{-6}$ K^{-1} [53]. $La_xSr_{1-x}TiO_3$ sintered on yttria-stabilized zirconia was found to be dimensionally and chemically stable when subjected to oxidation-reduction cycling [34,53]. Moreover, if this material is mixed with YSZ, both good compatibility and nano-porous microstructure can be obtained due to limited sintering or grain growth [34].

STO is a wide band gap insulator (Ea ≈ 3,2 eV) but can easily be made conductive through n-type doping using Nb, La or oxygen vacancies [56]. The substitution of La for Sr renders STO highly conductive, hence it could be a valid candidate as anode for micro-SOFC. In this case, partial substitution of La^{3+} into Sr^{2+} sites should result, per each La atom, in donating one electron to the conduction band of STO [56]. The resistivity of bulk LSTO is reported to range from 0.001 to 1 Ω·cm at room temperature, making it a promising conductive layer in oxide electronic devices [56]. It has been established that strontium titanite exhibits n-type semiconducting behaviour when it is donor-doped (e.g. with La^{3+}) and/or exposed to a reducing atmosphere, i.e., its electrical conductivity increases with increasing donor content and/or decreasing pO_2 [53].

The perovskite structure of $SrTiO_3$ is stabilized in a cubic unit cell with space group Pm-3m at room temperature. Therefore, the ionic radii of the doping elements play an important role in order to maintain a cubic structure [54]. Lanthanum is an appropriate donor dopant because its ionic radius (0,132 nm) is similar to that of Sr^{2+} (0,140 nm). It is stable in the trivalent state ensuring its incorporation in the perovskite lattice as La^{3+} [53]. Due to the difference in valence between La^{3+} and the Sr^{2+}, the introduction of La into the lattice requires a modification of the lattice defect structure, to maintain electro-neutrality [53]: (1) under oxidizing conditions (i.e. high oxygen partial pressures), the compensation occurs by the formation of Sr vacancies in the lattice coupled with the formation of SrO layers within the structure; (2) under reducing conditions (low pO_2), it was concluded that, as lattice oxygen is lost to the atmosphere, the Sr vacancies and the SrO layers are eliminated; therefore the charge compensation for the La^{3+} becomes electronic in nature through the formation of electrons in the conduction band or (if the electrons are localized) conversion of Ti^{4+} to Ti^{3+} [53].
However, the high temperature conductivity value of n-doped $SrTiO_3$, cited by different authors, varies significantly [13, 52, 53, 56, 57].

As a reference, figure 2-6 shows the electrical conductivity variation with temperature and under oxidizing and reducing atmosphere of $La_{0,3}Sr_{0,7}TiO_{3-\delta}$ bulk anode [57]. The higher

conductivity in reducing atmosphere is evident, especially at high temperature (≥ 800°C) where the gap between the corresponding conductivity in air is huge.

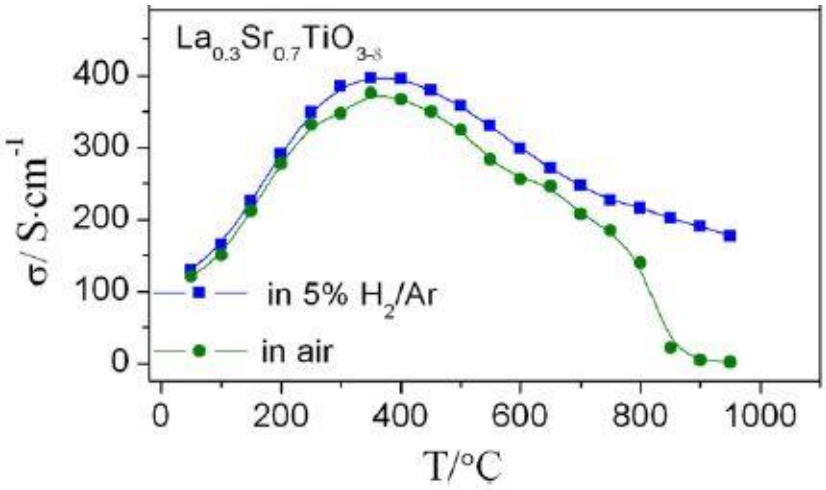

Figure 2-6. Temperature and atmosphere dependences on electrical conductivity of perovskite $La_{0,3}Sr_{0,7}TiO_{3-\delta}$ (extracted from [57])

Figure 2-7 shows the thermal-cyclic performance of a $La_{0,3}Sr_{0,7}TiO_{3-\delta}$ anode for bulk SOFCs [57]. The sample was heated in 5%H_2/Ar for a conductivity measurement and then cooled in air within a furnace. This process has been repeated three times. The electrical conductivity was slightly lower than the uncycled sample, mainly due to the incorporation of oxygen vacancies from the surrounding oxygen during cooling process. Anyway, the electrical conductivity in the third cycle was almost overlapped with that in the second cycle, demonstrating a good thermal-cycling performance.

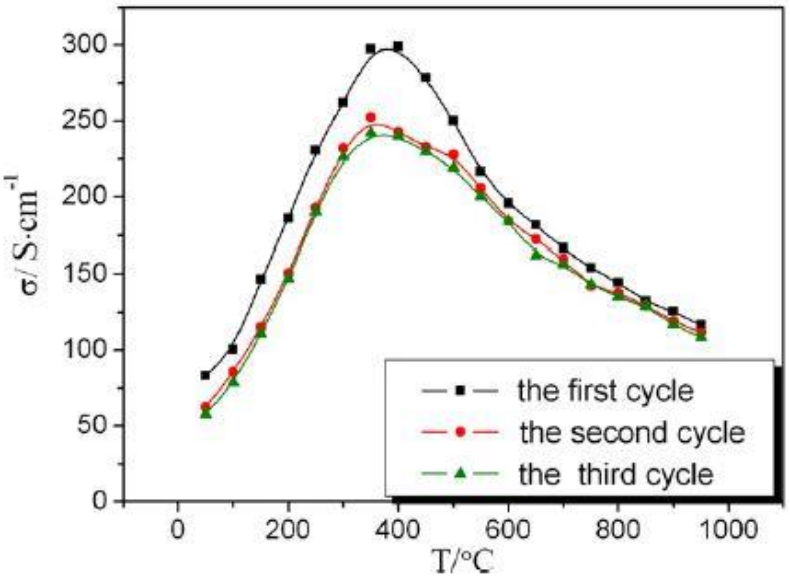

Figure 2-7. Thermal-cyclic performance of $La_{0,3}Sr_{0,7}TiO_{3-\delta}$ (extracted from [57])

There are several works which studied the thermo-electrical properties of an A-site deficient LST anode [52, 53, 55, 57]. They are becoming interesting since the deficiency can lead to

increased conductivity values. In addition, A-site deficient perovskite has a lower tendency to react with the zirconia electrolyte and to form secondary phases such as insulating $La_2Zr_2O_7$ or $SrZrO_3$, as it is well known from several cathode materials containing lanthanum and strontium [55].

Furthermore, the exsolution technique was adopted by using composition of (La, Sr) – (Ti, Ni) O_3 (LSTN) to improve electrical conductivity and catalytic activity [34].
In the following sections 3-2 and 4-2, the complete characterization route of $La_{0,3}Sr_{0,7}TiO_3$ (LST37) will be proposed. Despite the already known advantages of a porous structure (it would increase the TPB, enhancing the electrochemical performances), the aim of this preliminary analysis is to obtain dense thin films. The main reasons are:

- They allow an easier characterization of electrical in-plane properties (indeed the porosity increases the resistivity);
- They allow a more reproducible electrochemical characterization of the true properties of the anode due to the controlled area (surface) and to the absence of TPBs, permitting to extract the real behaviour of LST in reducing atmospheres;
- They may offer a better mechanical stability in micro-SOFC membranes.

Increasing the porosity of the films will be a further step, whereas in this work the main purpose is the extraction of the real electrochemical properties of LST thin films.

3 EXPERIMENTAL METHOD

3.1 Joinining experimental procedure

As described in section 2-1 the joining material chosen for the micro-SOFC encapsulation is a glass-ceramic seal. The chosen glass powder was low melting, lead free and passivation glass (G018-197), provided by SCHOTT AG. The composition of the glass is reported in section 4-1. A suggested joining profile was provided by SCHOTT AG as well.
A preliminary study was carried out on the G018-197 glass in order to determine the characteristic temperatures and optimize the sintering parameters:
To this purpose, the following characterization technique were used:

- Differential Scanning Calorimetry (DSC) and Thermogravimetric Analyses (TGA);
- Temperature X-Ray Diffraction (XRD);
- Hot Stage Microscopy (HSM).

Based on the obtained results, different sintering procedures were proposed, and the quality of the obtained glass-ceramic sealant was evaluated by:

- Thermal Expansion Coefficient (CTE) measurement;
- Scanning Electron Microscopy (SEM) and Energy Dispersive X-Ray analysis (EDS).

In particular, the crystalline structure of the final glass-ceramic sealant (after thermal treatment) had to be studied, to understand if the obtained sealing layer could present a glassy or a glass-ceramic composition (which includes crystalline domains) and its influence on the stability of the bonding.
Moreover, a printability study was necessary to optimize deposition of the glass paste. Consequently, working on the viscosity and on extrusion parameters was fundamental.
For all these reasons, the experimental procedure on the joining can be divided in two topics:

1. The optimization of the thermal treatment for the sealant;
2. The optimization of the glassy-paste deposition.

3.1.1 Thermal treatment optimization

Firstly, Differential Scanning Calorimetry (DSC) and Thermogravimetric Analyses (TGA) were performed at IREC, to study the phase transition behaviour of the glass powders. The instrument measures the enthalpy variation due to physical and chemical changes in a material as a function of temperature.
Inside the instrument, there are two furnaces, one with the sample and the other with a reference material, separated with an insulated heat sink. Platinum resistances and thermometers are placed in both furnaces measuring the difference in the amount of heat required to increase the temperature of the sample and reference as a function of temperature. The exothermic peaks are generally directed upwards and they represent crystallization formation, since this process releases heat flow. On the other side, the “melting” phenomenon of a glass is an endothermic

process, where the sample absorbs the heat flow, as shown in figure 3-1. This process is characterized by a peak directed downwards. The DSC has been performed together with a TGA, which can weigh the sample mass variation over time and temperature.

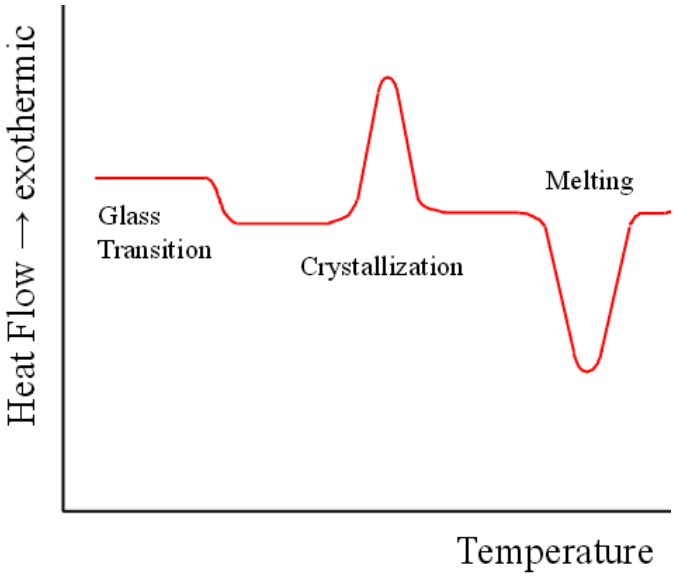

Figure 3-1. DSC behaviour on glasses. (extracted from [59]).

Next, X-ray Powder Diffraction (XRD) analyses were performed both at POLITO and IREC, trying to identify the possible crystalline phases present in the glass sealing after the thermal treatment. The sample is placed in the path of an X-ray beam. X-rays diffract through the crystal structure (if present) and they are received by the detector. The beam source and the detector are rotated through a range of angles which allows the detection of crystalline planes. In particular, the distance between planes of atoms that generate the diffraction peaks is called d-spacing. Each peak in a diffractogram corresponds to a specific d-spacing and hence crystal orientation. Figure 3-2 explains the physic principle of the XRD. The instrument detects the angle (2θ) of the diffracted beam. Knowing the wavelength (λ) of the incident X-ray beam (usually generated from Cu filament), it is possible to calculate the d-spacing with the Bragg's law:

$$n\lambda = 2dsin\theta \qquad (3.1)$$

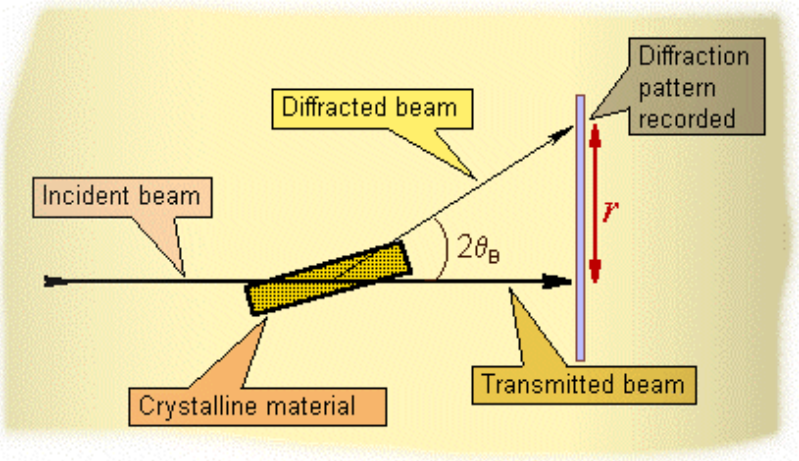

Figure 3-2. XRD scheme of functioning. (extracted from [60]).

In general, an XRD analysis could give several results: it can measure the average spacing between layers of rows of atoms; it can determine the orientation of a single crystal or grain; it can find the crystal structure of an unknown material; it can measure the size, the shape and internal stress of small crystalline regions. In this study, XRD was used to follow the phase transition from amorphous to crystalline behaviour of the glass powders, while increasing the temperature. Indeed, the *XRD Bruker-D8* advanced equipment used in this work, located at IREC, was able to perform in-situ temperature XRD experiments. This technique is based on a heating stage mounted on an *Anton PAAR XRK 900* chamber coupled with the XRD equipment. As shown by figure 3-3, the sample is closed into the chamber which can be controlled in temperature. The beam rays are ejected from the left and detected from the right arm.

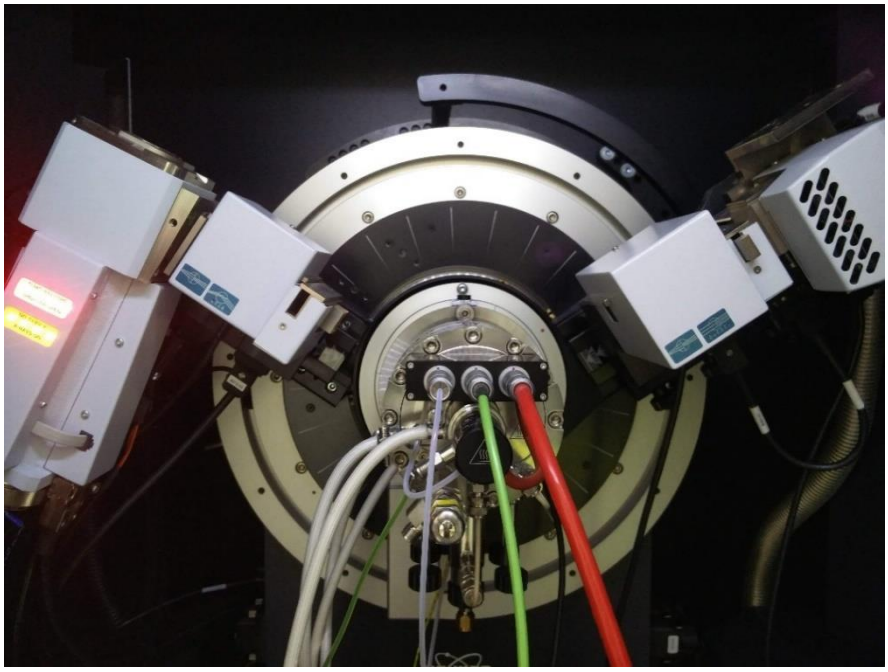

Figure 3-3. Temperature XRD equipment at IREC.

The results obtained were elaborated with the *X'Pert HighScore Plus* software, which allows a chemical identification of the peaks, through the matching with several references uploaded.

Hot Stage Microscopy (HSM) measurements were performed at POLITO to study the shrinkage behaviour of the glass during the sintering. The experiment consists on heating a small pellet of glass powders and controlling constantly its specific volume variation. Figure 3-4 shows the setup adopted at POLITO.
The sample is placed in the chamber, in the centre of the figure 3-4. Then a lamp, placed at the left side, illuminates the sample through a window of the chamber. On the right a camera records the shape variation with sequential pictures. The main parameters controlled are the temperature and the heating rate, time of the frame, the total area of the pellet, the height and the width of the sample and a form factor.

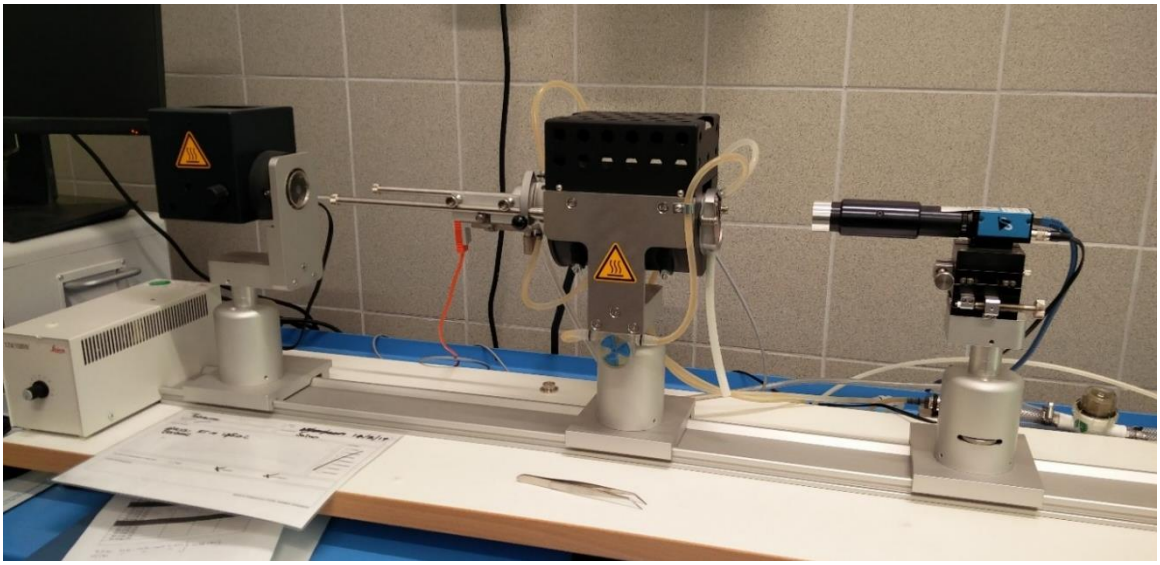

Figure 3-4. HSM setup adopted at POLITO.

Two different thermal treatments for the sealant have been considered. Therefore, Scanning Electron Microscopy (SEM) together with Energy-dispersive X-ray spectroscopy (EDS) measurements were performed on Si wafer/sealant/Si wafer joints, at both POLITO and IREC. A SEM uses a high-energy beam of electrons, focused on the surface of a sample. The kinetic energy of the accelerated electrons is dissipated by the electron-sample interactions. These interactions generate: secondary electrons (used to produce SEM images), backscattered electrons (used to determined chemical composition), X-Ray photons (used to determine the elemental composition, EDS) visible light and heat. *INCA* software was used to detect and evaluate the chemical composition of the glass per each thermal treatment considered.

As a final characterization, dilatometry measurements were performed at POLITO showing different CTE accordingly to the different thermal treatments adopted. The dilatometer measures dimensional changes caused by temperature. The measurements were performed between RT to the T_g, where the glass begins to soften. A pellet of the glass-ceramic material is placed inside a retractable, tubular furnace. A spring-loaded pushrod is positioned against the sample. The opposite end of the pushrod is connected to a linear variable displacement transducer. The dimensional change of the sample resulting from the controlled temperature program is measured as the pushrod physically transmits the length change to the transducer. The displacement is recorded in relation to the temperature recorded with a thermocouple located next to the sample. A calibration or correction curve is applied to compensate the expansion of the sample holder and pushrod [61]. Knowing the initial length of the sample (L_0), measuring the temperature changes (ΔT) as well the dimension variation (ΔL), the thermal expansion coefficient (CTE or α) can be calculated with the equation (3.2):

$$\alpha = \frac{\Delta L}{\Delta T} L_0 \qquad (3.2)$$

Figure 3-5 represents the dilatometry used at POLITO for the measurements.

The results regarding the optimization of the thermal treatment for the joining, obtained and matched from each characterization measurements, are exposed in chapter 4-1.

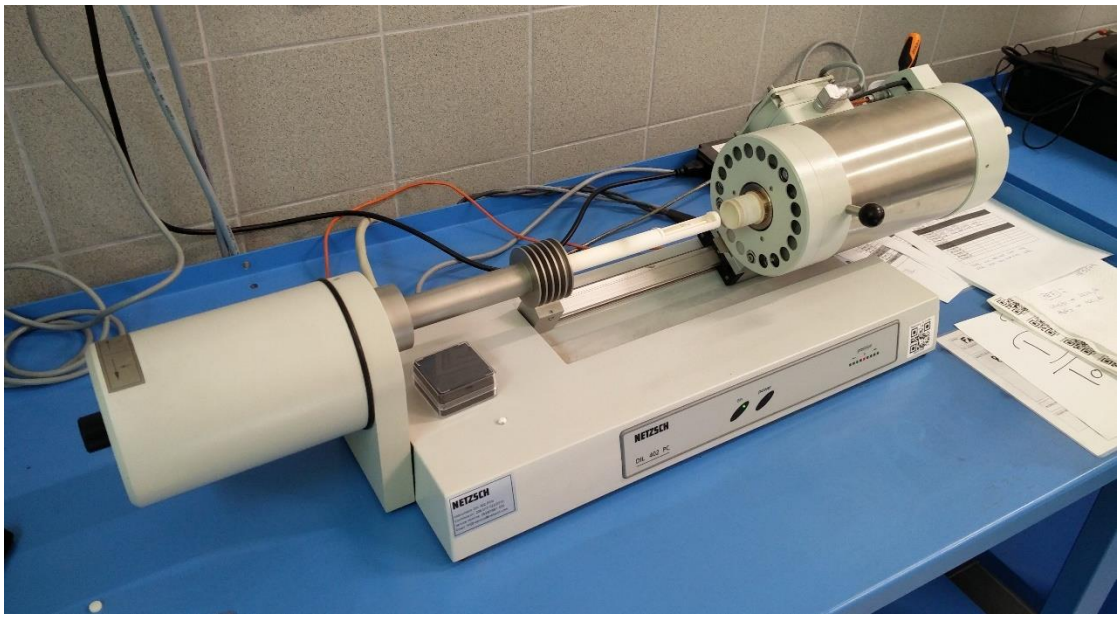

Figure 3-5. Dilatometer used at POLITO.

3.1.2 Sealant deposition optimization

The study for the optimization of the deposition parameters consisted in three steps:

1) study of the rheological properties of the glass sealant with a Bohlin viscometer;
2) wettability tests of the binder on different surfaces;
3) optimization of the LDM system.

Bohlin viscometer equipped with a spindle, plate cone head (15 mm of diameter and 5,4° of peak angle) has been used to evaluate the rheological properties. The working principle is based on the measurements of the torque on a vertical stand that moves the spindle in a rotational direction. The rotation of the spindle is usually proportional to how viscous the sample is. The viscometer placed at IREC works with a servo system, which means that a servo motor moves the shaft where the spindle is directly connected. The amount of current used to move the shaft is directly proportional to the "viscous resistance" of the sample. By setting the rotation speed of the system with a servo encoder, both the torque and the viscosity of a given sample can be determined. Two types of tests were performed: viscosity measurements variation with time at constant shear rate and viscosity variation increasing the shear rate.

The wettability tests were performed at IREC on the binder (97 wt% of Terpineol and 3 wt% of Elvacite ®) because the sealant density was too high for the sensible distribution channel of the instrument. The setup is composed by a syringe of 10 ml where the fluid is charged. the syringe is directly connected to a little tube which brings the fluid sample on the measurement plate through a final nozzle. The piston of the syringe is locked and mechanically connected to a motor which can extrude the sample with a controlled and precise step, communicated by the software.

Depending on the type of measurement, the drop is released onto the plate or it remains in contact with the nozzle. The plate is supported by a 3-axial motor which is controlled by a joystick. A high resolution camera records and measures the shape and the characteristic angles (such as the contact angle) which gives several properties.
In principle, the contact angle is the angle where a liquid-vapor interface meets a solid surface. It quantifies the wettability of a solid surface by a liquid via which is directly related to the molecular interaction between solid, liquid and vapor phases. The shape of the liquid-vapor interface is determined by the Young-Dupré equation:

$$\gamma_{SV} = \gamma_{SL} + \gamma_{LV} cos\theta \qquad (3.3)$$

Figure 3-6 resumes the parameters of the Young-Dupré equation and represents the drop equilibrium between the three phases.

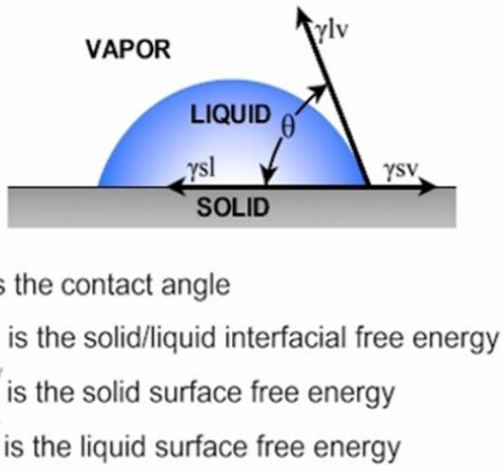

Figure 3-6. Drop equilibrium and characteristic parameters. (extracted from [62]).

With a sessile drop test is possible to measure the contact angle (θ). The work of adhesion (W_A) can be determined experimentally because:

$$\gamma_{SL} = \gamma_{SV} - \gamma_{LV} cos\theta$$

$$W_A = \gamma_{SV} + \gamma_{LV} - \gamma_{SL} = \gamma_{SV} + \gamma_{LV} - \gamma_{SV} + \gamma_{LV} cos\theta = \gamma_{LV}(1 + cos\theta) \qquad (3.4)$$

Therefore, evaluating the liquid surface tension γ_{LV}, which is proportional to the density of the fluid, it is possible to determine the work of adhesion. γ_{LV} has been measured with the pendant drop test, in which the drop remains in contact to the nozzle and in the meanwhile the spherical shape of the drop is measured by the camera.

Once the liquid surface free energy is measured, the wettability and hence the spreading work can be determined. The spreading work (W_S) is related to W_A, with this formula:

$$W_S = W_A - W_C = \gamma_{LV}(1 + cos\theta) - 2\gamma_{LV} = \gamma_{LV}(cos\theta - 1) \qquad (3.5)$$

In conclusion a new LDM system has been tested. The main aim was to guarantee a controllable and thin extrusion, since the sealant continued flowing also without any pressure of the piston. A retraction type of system has been adopted as descripted in chapter 4-1. Moreover, a new strategy to control the paste height has been adopted and an optimization of the deposition parameters have been performed. Two software were used to design the extrusion:

1. *Cura:* it can create the deposition shape as well as the quantity of the paste extruded;
2. *Pronterface*: it is used to connect the software and the hardware. It is also necessary to set the initial position (x_0, y_0, z_0) of the syringe and can control manually the extrusion as well as the retraction of the piston.

3.2 Anode characterization experimental procedure

The perovskite strontium doped lanthanum titanate ($Sr_{0,7}La_{0,3}TiO_3$, LST37) was studied as alternative anode for micro-SOFC devices. Different thin films were produced with pulsed laser deposition (PLD) and tested with the aim of extracting the real properties of the material in reducing atmosphere. This section resumes the experimental method adopted as well as the techniques and the physical principles behind the measurements.
First, a description of PLD technique is given, with the effects of its main deposition parameters; afterwards, the optical (ellipsometry) and microstructural (XRD, SEM, EDS, Atomic force Microscopy, AFM) characterization techniques are proposed; finally, the functional properties obtained with in-plane electrical and out-of-plane electrochemical measurements are described.

3.2.1 Pulsed laser deposition (PLD) technique

Pulsed laser deposition is a thin-film processing technique based on the laser ablation of a target material and its deposition on a substrate, in vacuum conditions. The laser pulses, ablating a small amount of material, create a plasma plume perpendicular to the target surface, which is directed to the substrate placed just on top of it. The general layout of the system is shown in figure 3-7.

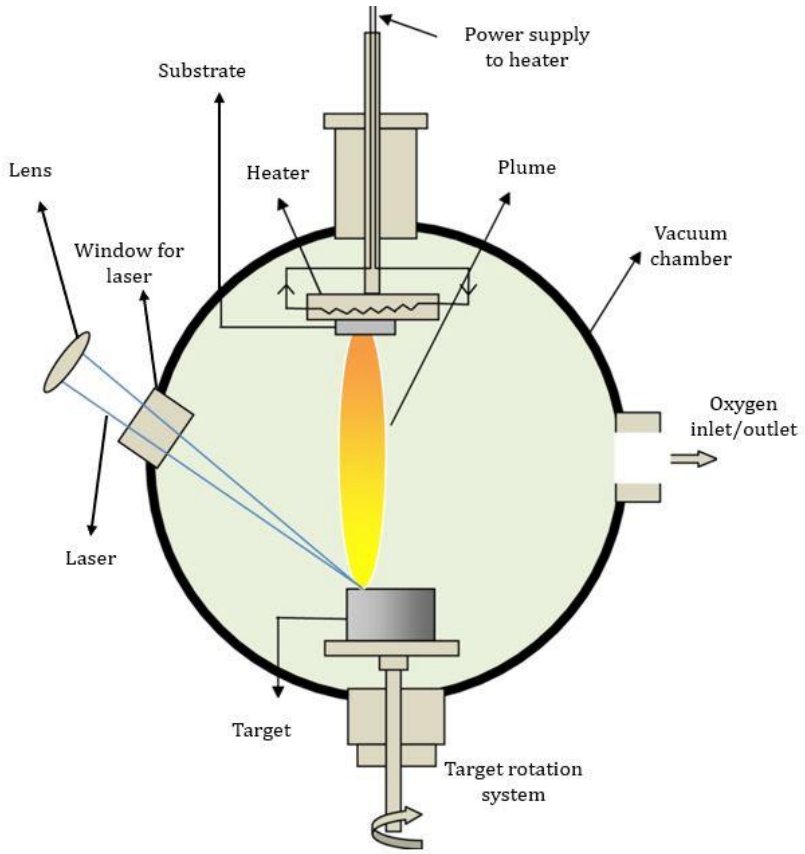

Figure 3-7. Illustration of a PLD system. (adopted from [65]).

The PLD system placed at IREC and used in this work is represented in figure 3-8. The KrF excimer laser (Lambda Physik COMPex PRO 205) produces the laser beam which enters through the window of the ultra-high vacuum (UHV) chamber, thanks to the optical system. The motions of the lens allow the radial ablation of the circular target, which is usually rotated to guarantee the whole surface exposure. The substrate can be fixed or not, depending on the deposition type. A heater is used to keep the substrate at desired temperature, which can determine the films structure, as described after. The substrate is loaded through the loadlock chamber which is directly connected to the UHV chamber through an intermediate valve. When the necessary vacuum in the loadlock is reached, the valve is opened, and the sample is carefully inserted with the arm and left on the substrate plate.

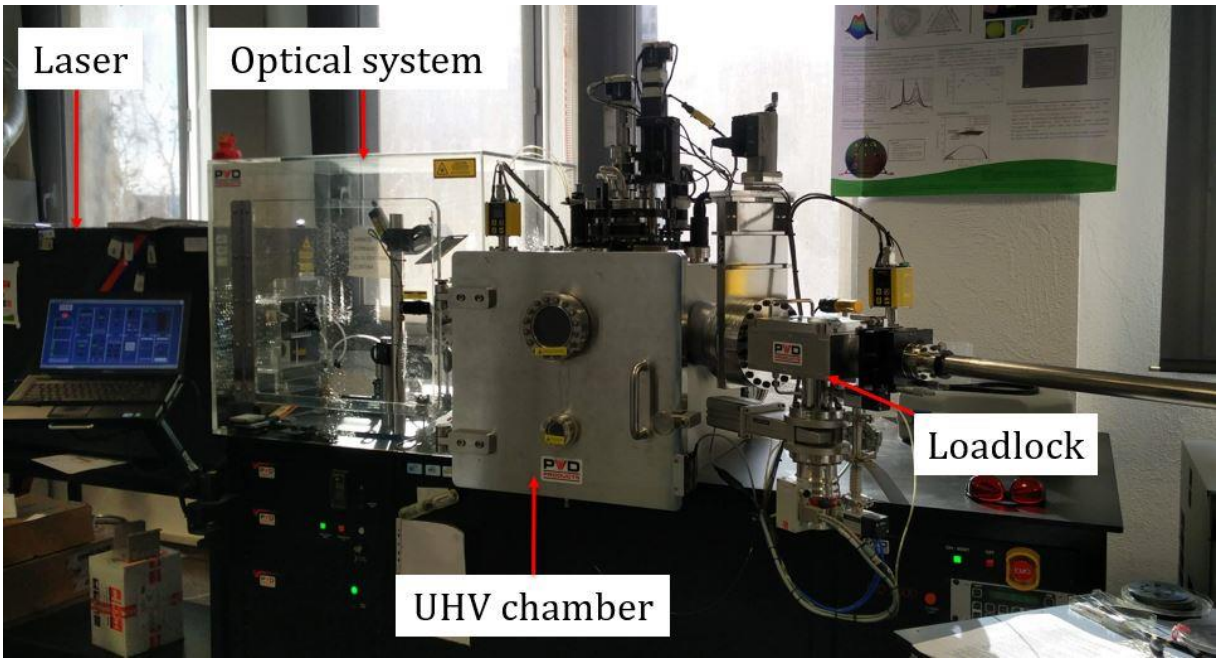

Figure 3-8. PLD5000 from PVD ®, located at IREC.

To transfer the stoichiometry from the target to the grown film is fundamental to study the desired material and the preparation of targets is a key point to deposit high quality films. The target could influence the films with several properties which must be controlled: (1) stoichiometry of the target; (2) the relative density; (3) the surface roughness [15]. Usually the target used are pellet type, produced with conventional sintering (CS). In this work, the powders of material are compacted by uniaxial die on a press machine and heated up to the sintering temperature.

The microstructure, the homogeneity and the film thickness are strongly influenced by the PLD parameters such as temperature, background pressure, working distance and laser fluence.

- The influence of substrate temperature: low substrate temperature does not allow surface diffusion and hence the columns films growth preserve a random orientation which lead to a porous structure; with high substrate temperature, instead, polycrystalline dense columnar microstructures are obtained [17].
- The background pressure influence: the small flux (generally O_2 for oxides deposition) introduced into the UHV chamber aims to maintain the atmosphere in a constant pressure

which is able to tune the film porosity. In general, a high pressure allows more interactions of ablated material with background species and hence a porous structure is obtained [15]. The combined effect of pressure and temperature is represented in figure 3-9.

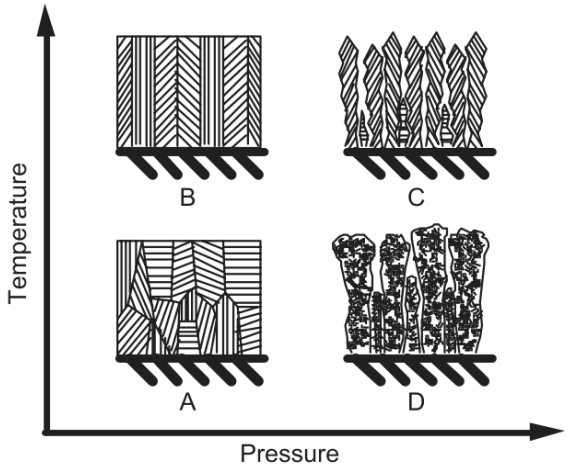

Figure 3-9. Combined effect of temperature and pressure in ceramic oxide thin-film microstructure growth by PLD (extracted from [17]).

- Influence of working distance: in general, as much far the substrate is from the target, the lower is the growing rate, since less material arrive with enough energy for film growth [15].
- Influence of laser fluence: the laser fluence is defined as the laser energy per unit area (mJ/cm^2). The plume diameter depends on the spot size of the laser beam; the higher the laser fluence, the higher volume is ablated [17].

Other parameters influence the microstructure of the films and the ablation of the target: the laser phonon energy (must be higher than the target material bandgap), the pulse frequency, the total number of pulses, the wavelength of the laser and the substrate material. Table 3-1 resumes the main parameters adopted in this work:

Table 3-1. main PLD parameters adopted in this work

Target material	LSTO37	[-]
Substrate chip	MgO	[-]
Target rotation	15	[rpm]
Substrate rotation	0	[rpm]
Laser energy on target	165 – 175	[mJ]
Frequency	10	[Hz]
Pressure	**5 – 60 – 120 – 200**	[mtorr]
Gas flow (O_2)	5 – 10	[cm^3/min]
Substrate temperature	650	[°C]
Heating rate	12	[°C/min]
Target substrate distance	90	[mm]
Pulses	**5000 – 7000 – 11000 – 15000**	[-]

Since the study was performed to obtain the real material properties, dense and columnar films were deposited, which correspond to high substrate temperature and low background pressure. The substrate temperature (650°C) and material (MgO) were taken from the experimental setup of Eom et al. on the $Sr_{0,75}La_{0,25}TiO_3$ thin films study. The background pressure was varied discretely in four trials: 5/60/120 and 200 mtorr which correspond to 0,0067/0,08/0,16 and 0,27 mbar. The number of pulses has been incremented each deposition following the increasing value of background pressure, as shown in table 3-1, guaranteeing a film thickness almost constant. The target was rotated at 15 rpm, with a fixed substrate-target distance of 90 mm. The material characterization was performed in chip level and hence homogenous thickness and structure were obtained in the same deposition. Since PLD5000 is designed for large area depositions (LA-PLD), a specific chips holder was adopted as represented in figure 3-10. Therefore, the substrate was kept fixed during the whole deposition.

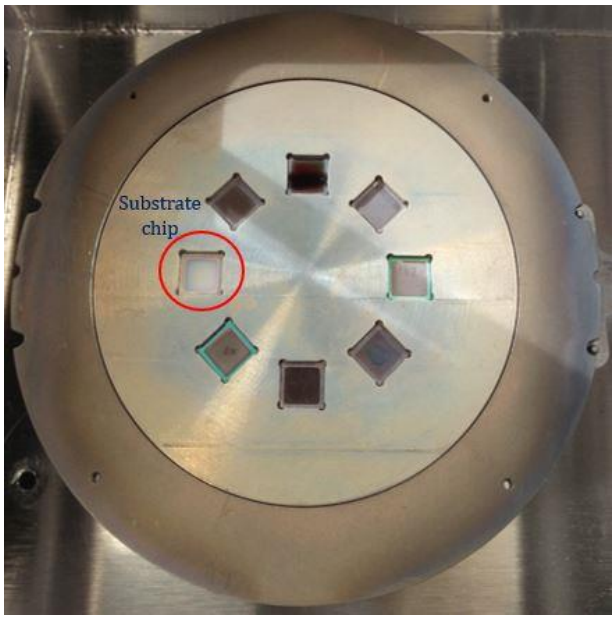

Figure 3-10. Holder for chip deposition, in the loadlock chamber.

3.2.2 Optical and structural properties

Once the depositions were performed, ellipsometry measurements provided the thickness and the optical constants of the films. This technology is attractive for its precision, low or no sample preparation and the fact of being non-destructive. The measurement is based on the study of the polarization variation of a light beam reflected on a thin film. The interface between two films or between the film and the substrate can be detected by the discontinuity in the light optical constants, i.e. *n (the refractive index)* and *k (the extinction coefficient)*. The instrument is composed by a light source (a lamp) emitting electromagnetic waves which are linearly polarised by a sequent polarizer. The waves reflect on the sample which change the polarization into elliptical by reflecting the beam. Finally, a modulator and an analyser restore the linear polarization of the waves which have changed during the whole path. This difference in measured by the detector and gives the optical properties of the film.

In this work, the analysis has been performed in the visible range of light spectrum (from 0,6 to 5 ev) with a step-measurement of 0,05 ev. The spectra measured has been fitted with *DeltaPsi2* software by using a certain number of optical oscillators. Practically, by leaving as free some parameters like thickness, roughness and some optical oscillators, it has been possible to optimize the fitting step by step.

X-Ray Diffraction (XRD), Scanning Electron Microscopy (SEM) and Energy dispersive X-ray Spectroscopy (EDS) were performed to each film to highlight the structural differences between them. The instrument setups as well as the measurement principles are described in section 3-1. A Zeiss Auriga SEM was used to study the morphology of the film top views. The film and pellet stoichiometry were measured with EDS. A Brucker-D8 Advance XRD was used to detect the polycrystalline structure of each film and its variation with the pellet one. In particular, the parameters adopted for the XRD analysis are resumed in table 3-2.

Table 3-2. XRD parameters used.

Detector aperture	5	[mm]
Source aperture	1	[mm]
Range 2θ	20-80	[°]
V	40	[kV]
I	40	[mA]
Offset	1,5	[°]
Time measurement each	0,5	[s]
Increment	0,01	[°]

When measuring a thin film over a single crystal (like MgO or YSZ used in this work), some peaks of the substrate, which have high intensity, can cover peaks of the top layer. To avoid the diffraction of the single crystal, an offset is applied so that the substrate planes do not satisfy the diffraction condition [67]. The offset adopted in these measurements has been set at 1,5°.

Atomic Force Microscopy (AFM) was used to study the surface of the samples. It is a non-destructive technique, composed by a sharp probe which measures the topography of the surface by calculating the z displacement between the tip and the grains. The Van der Waals interactions between tip and surface cause the variation of the resonance frequency, directly related to the distance between them. The XE15-AFM from Park systems was used to study the roughness of the films.

3.2.3 Electrical and electrochemical properties

The functional properties of the films, determined with in-plane electrical measurements and electrochemical impedance spectroscopy (EIS), are significant for the materials characterization and hence their adoption as anode for micro-SOFC.

Van Der Pauw method was used to determine the electrical resistivity in-plane of the films. Figure 3-11 shows the setup adopted. It is composed of four point contacts (A, B, C, D in the

figure), which are directly connected to the electrical circuit, able to dispense a current and measure a corresponding voltage. The measurements were performed varying the temperature between RT to 500 – 550°C and the oxygen partial pressure (pO_2). The sample was positioned on a heating plate of a temperature-controlled Linkam probe station (THMS600).

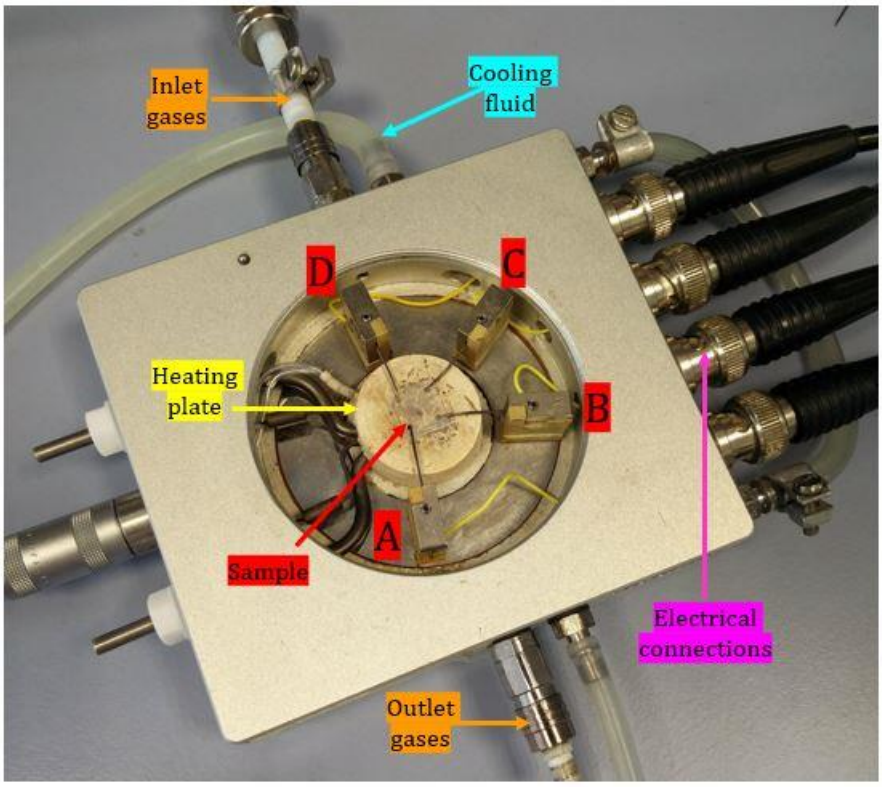

Figure 3-11. Linkam stages used for the electrical measurements.

Van Der Pauw method is based on the calculation of film resistance, by applying a current between two consequent contacts (for instance A and B, I_{AB}) and measuring the voltage in the opposite side (in this case C and D, V_{CD}). The resulting resistance R_O is simply calculated with the Ohm's law, $R_O = V_{DC}/I_{AB}$. The sheet resistance of the film can be measured by changing alternatively the polarity and the contacts side, resulting in two different resistances R_V and R_O, which can be calculated for symmetry reasons as:

$$R_V = \frac{V_{AD}}{I_{BC}} = \frac{V_{DA}}{I_{CB}} = \frac{V_{BC}}{I_{AD}} = \frac{V_{CB}}{I_{DA}} \qquad (3.6)$$

$$R_O = \frac{V_{AB}}{I_{DC}} = \frac{V_{BA}}{I_{CD}} = \frac{V_{DC}}{I_{AB}} = \frac{V_{CD}}{I_{BA}} \qquad (3.7)$$

Therefore, the sheet resistance (R_S) can be evaluated with the equation (3.8):

$$e^{-\frac{\pi R_V}{R_S}} + e^{-\frac{\pi R_O}{R_S}} = 1 \qquad (3.8)$$

In a perfectly square and homogeneous sample R_V and R_O are identical and hence the equation (3.8) can be analytical solved. Nevertheless, it is common to find a small difference between them

and hence the sheet resistance can be calculated with some simplifications with the equation (3.9):

$$R_s = \frac{\pi}{ln2} \cdot \frac{R_O + R_V}{2} \qquad (3.9)$$

Finally, the resistivity (ρ) is simply obtained multiplying R_S with the thin film thickness, while the conductivity (σ) is the inverse of ρ.
This method can be applied only when the film is homogeneous in composition and thickness, the electrical connections are ideally point contact and the thickness of the film is smaller than the lateral sizes. Therefore, the structure obtained from the PLD must be controlled and manage.

The electrochemical properties of the thin films were studied by Electrochemical Impedance Spectroscopy (EIS). This measurement can separate the contribution of each component of a cell to the total resistance. An AC voltage is applied to the system in a certain frequency range which allows separating the different impedance contributions depending on the characteristic time constant (τ) of each process occurring in the system [15]. The voltage and the current can be expressed in sinusoidal form:

$$E(t) = E_0 \cdot e^{i\omega t} \qquad (3.10)$$

$$I(t) = I_0 \cdot e^{i\omega t + \theta} \qquad (3.11)$$

Where E_0 and I_0 are the corresponding amplitudes, ω is the variable angular frequency and θ the phase shift. Therefore, impedance can be defined as:

$$Z(\omega) = \frac{E(t)}{I(t)} = |Z| \cdot e^{(-i\theta)} = |Z|cos\theta - i|Z|sin\theta = Z'(\omega) - iZ''(\omega) \qquad (3.12)$$

The applicability of this final expression requires a linear dependence between current and voltage, which is not always present (for instance with charge transfer phenomena). Therefore, small AV voltages must be applied to keep this pseudo-linear regime [15].
There are different ways to plot the impedance. Usually the Nyquist plot is used, with Z' placed in the real axis and Z'' in the imaginary axis. In a system with only a conduction mechanism, a semicircle of diameter R (the material's resistance) appears with the center on the Z' axis at the position (R/2; 0). When complex system such as an electrode/electrolyte/electrode multilayer is measured, several different mechanisms take place. Each of them contributes to the total resistance on the system and so different semicircles appear in the Nyquist plot, separate as their time constant (τ) differ. τ can be defined as:

$$\tau = \frac{1}{RC} \qquad (3.13)$$

Where C is the capacitance associated to the process. If the processes are well defined the semicircles have their distinct time constant which can be associated to a precise phenomenon, otherwise, the semicircles overlapped, and the phenomena are difficult to identify. The values of

τ are temperature dependent, hence the range of frequency in which a certain phenomenon appears can change with temperature.

The impedance spectroscopy measurement is obtained by varying the frequency of the signal ($f = \frac{\omega}{2\pi}$) in a large range (from 10^6 Hz to 0,05 Hz) while recording the impedance. The tests are performed at constant temperature and atmosphere before being changed for the following measurement. To analyse a spectrum obtained with the Nyquist plot, an equivalent electrical circuit is associated. The sub-circuit is usually composed by a resistance (R) and a capacitance (C), connected in parallel, representing a single phenomenon. In the case of multiple phenomena, the fundamental circuit is coupled in series with the others. Figure 3-12 represents a schematic equivalent circuit associated to a Nyquist plot of a fuel cell.

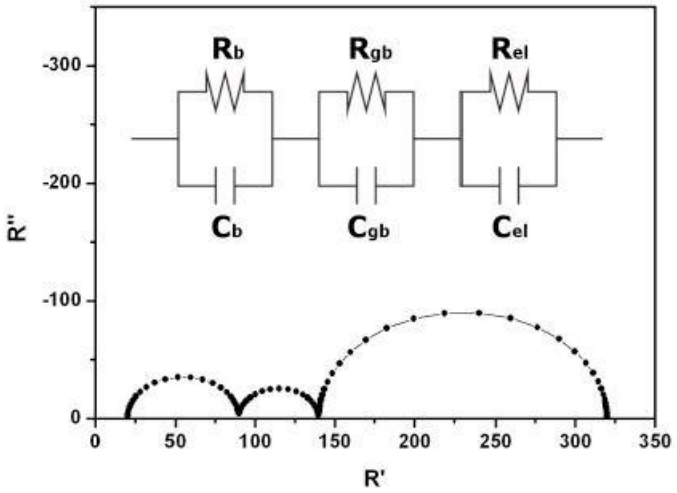

Figure 3-12. Nyquist plot and the corresponding equivalent circuit of a simple electrolyte cell (extracted from [15]).

In conclusion, different values of capacitance (C) can give information on the different processes present, as shown in table 3-3.

Table 3-3. Typical capacitance values for different processes on a ceramic material (extracted from [68]).

Process type	C [F/cm]
Bulk	10^{-12}
Secondary phases	10^{-11}
Grain boundary	10^{-8} - 10^{-11}
Bulk in ferroelectrics	10^{-9} - 10^{-10}
Surface layer	10^{-7} - 10^{-9}
Interphase sample-electrode	10^{-5} - 10^{-7}
Electrochemical reactions	10^{-4}

In this work, to better fit the EIS measurements, Constant Phase Elements (CPE) were used in parallel to the resistance, instead of the capacitance. The impedance (Z_{CPE}) and the time constant (τ) of this element can be calculated as:

$$Z_{CPE} = \frac{1}{Q(j\omega)^p}; \qquad \tau = \left(\frac{1}{RQ}\right)^{1/p} \tag{3.14}$$

Where Q is a pseudo-capacitance and p is the dispersion element with value 0<p<1.

To measure the out-of-plane electrochemical properties of LST, thin films were deposited on Yttria Stabilized Zirconia (YSZ) (001) single crystals, obtaining a symmetrical cell (LST/YSZ/LST) and measure the electrochemical performances of the anode. Porous gold paste was applied on LST to effectively measure the entire thin film surface and enhance the electron percolation. Au was chosen for its poor reduction properties [69, 70]. Gold nets and gold wires were used for the electrical connections.
Figure 3-13 shows a schematic cross-section of the symmetric cell prepared for the experiments.

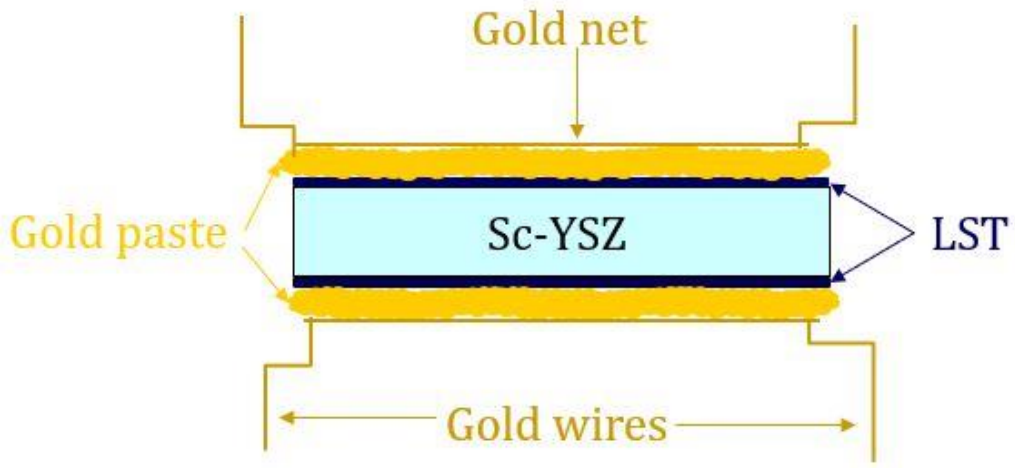

Figure 3-13. Schematic cross-section of the setup applied to the symmetrical cell.

The EIS measurements were performed in a ProboStat stage, varying the temperature from 600 to 700°C, using a tubular oven as shown in figure 3-14. The impedance spectroscopy was measured with a Novocontrol system (Alpha-A High performance frequency analyser) and a ZIROX oxygen pump was used to vary the atmosphere inside. Finally, the impedances were fitted by *ZView* software.

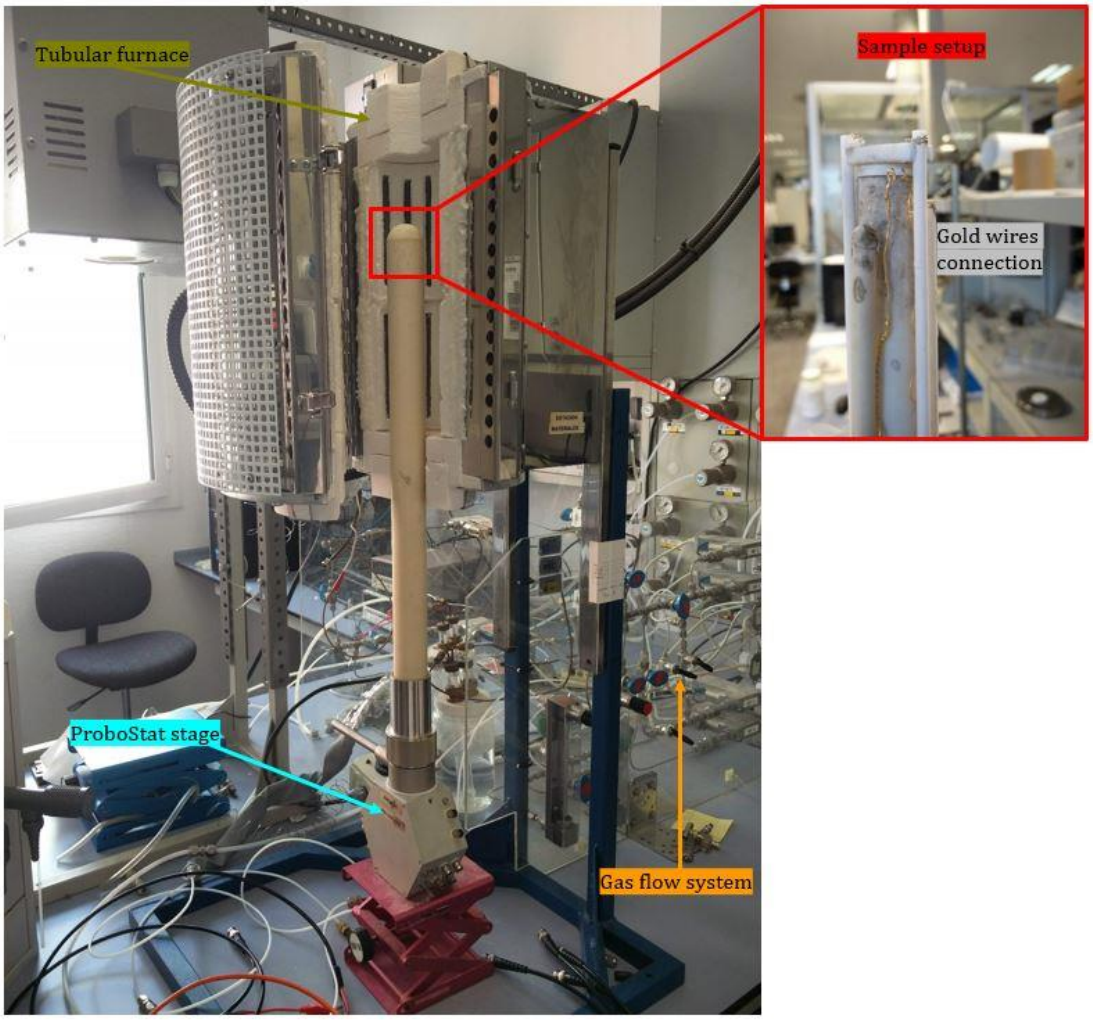

Figure 3-14. Experimental setup used for the electrochemical characterization.

4 RESULTS AND DISCUSSION

4.1 Glass sealant joining results

The glass powder (G018-197) chosen for the sealing is provided by SCHOTT AG and its main properties are resumed in table 4-1, taken from the glass data sheet [58].

The glass sealing procedure has been optimized following the experimental details described in section 3-1. Here, the development of the glassy paste characterization as well as its deposition enhancement are reviewed and discussed. In the final part of this section, after the main conclusions of the study, possible developments of the joining system are proposed.

Table 4-1. Main properties and chemical composition of G018-197 glass.

CTE [10^{-6} K^{-1}]	**T_g [°C]**	**Density at 25 °C [g/cm³]**	**Firing temperature [°C]**	**Holding time [min]**
4,4	557	3,8	675	10
	Oxide		**wt%**	
	ZnO		> 50	
	B_2O_3		10 – 50	
	SiO_2		1 – 10	
	Bi_2O_3		1 – 10	
	CeO_2		0,1 – 1	
	Sb_2O_3		0,1 – 1	

The choice of the glass powder has been taken to satisfy the following requirements:

- ✓ Lead free glass, to avoid the possibility of poisoning paste;
- ✓ CTE compatibility with silicon (2,6 – 4,2·10^{-6} K^{-1} in the temperature range of 300–900 K);
- ✓ The necessity of a printable paste, which means that can be extruded without relaxing too much after the deposition.

The ideally operating temperature of the membrane is around 600°C and the provided transition temperature (T_g) is 557°C.
The glass powder was mixed with an organic binder composed of 97 wt% of Terpineol and 3 wt% of Elvacite ® (isobutyl methacrylate), defining the weight ratio of powder and binder as:

$$\theta = \frac{weight\ of\ powder\ (G018{-}197)}{weight\ of\ binder} \qquad (4.1)$$

the maximal value of θ which allows to achieve a uniform paste is around 4 (hence 80 wt% of powder and 20 wt% of binder); while, values of θ lower than 2,5 could lead to a too low viscosity paste. Once the weight ratio is achieved, the paste was put in a container and mixed in a centrifugal mixer at 1500 – 2000 rpm for 2 – 3 min. Next, the paste was collected in a syringe and fixed in a liquid deposition modelling (LDM) system, based on 3D printing technique. The initial LDM system was composed by a little motor with 3-axial degree of freedom which could control the piston of the syringe and hence to extrude the paste through a needle, which size is in the range of 300 – 400 micrometres. The system is represented in figure 4-1.

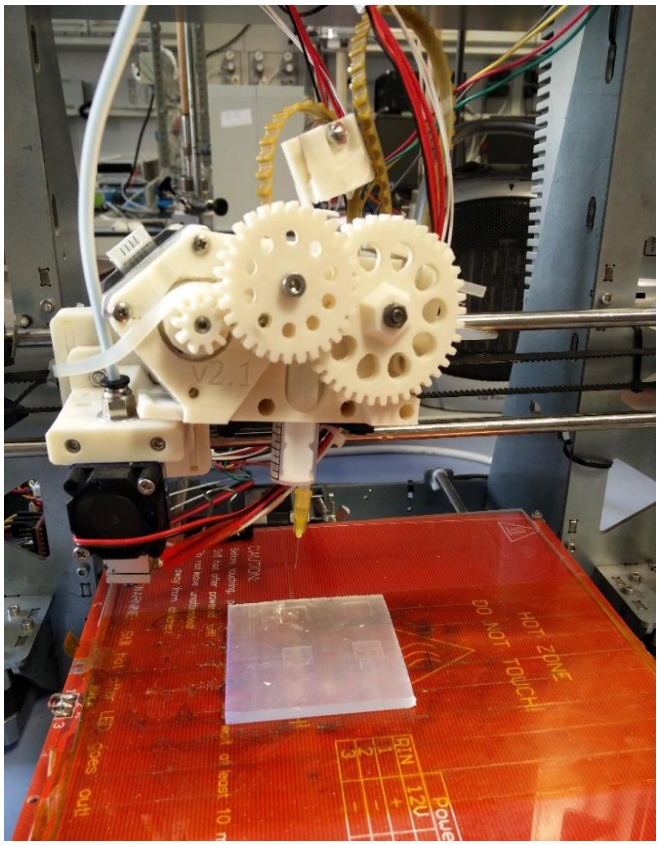

Figure 4-1. Initial LDM system.

Figure 4-2 shows a line of paste deposited on a silicon chip (a square of 1 cm). A second chip was carefully left on top and then, the obtained joining was thermal treated in an oven.

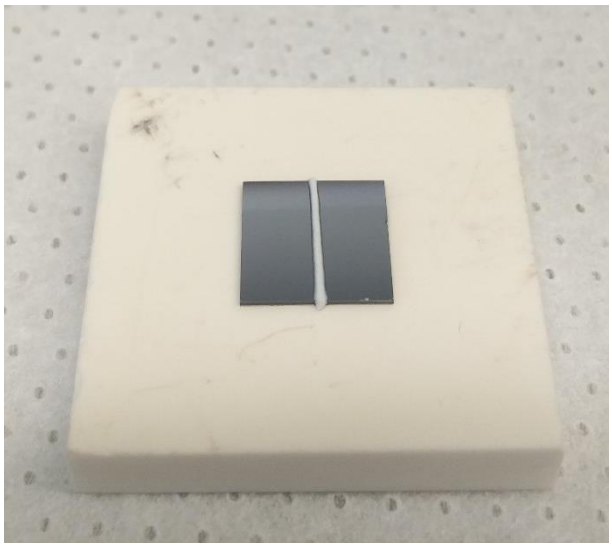

Figure 4-2. A line of paste on silicon chip, 1 hour after the deposition.

Controllable deposition (in terms of thickness and fluidity of extrusion) is difficult to obtain because of the proper balance of rheological properties, which, by Bohlin viscosimeter, are discussed later.

Initially, the thermal treatment adopted for the joining had the trend represented in figure 4-3. A constant and moderate heating rate of 3°/min was used, until an intermediate temperature around the Tg, with a holding time of 60 minutes, to complete firing and degassing of the organic vehicle. Then the temperature was raised up to 675°C (the firing temperature suggested by SCHOTT) with a holding time of 10 minutes. The cycle is completed with a cooling step down to the room temperature (RT). No vacuum neither external pressure were used for the joining.

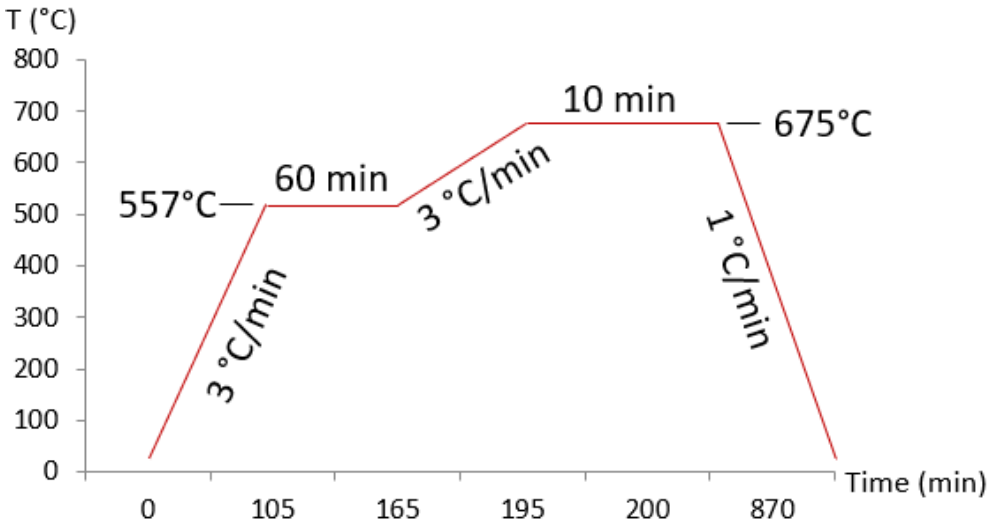

Figure 4-3. Thermal treatment used with SCHOTT suggestions.

Figure 4-4 represents the joining of two silicon chips with the glass sealant. A good adhesion was obtained, while void spaces (black holes) were present. The grey ones were amorphous-glass phases, which would ensure gas-tightness of the sealing. The image was obtained with a scanning electron microscopy (SEM) measurement described in section 3-1.

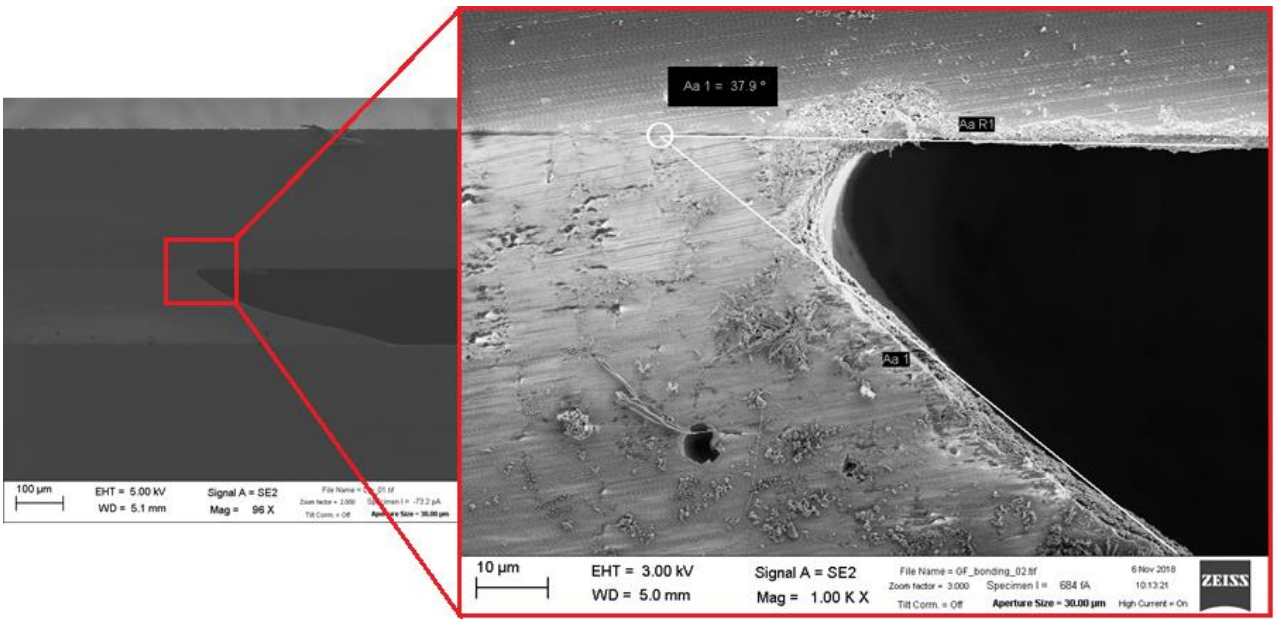

Figure 4-4. Cross section of the glass sealant joining. The bond was performed after drying the paste and with no external applied pressure.

In principle, the choice of glass powder and the sealing procedure were sufficient to guarantee a good wettability between the sealant and the silicon substrate. Despite this, a detailed study of the thermal and thermomechanical properties of the glass was carried out at POLITO and IREC, in order to optimise the joining thermal treatment and possibly to maximise the sinter-crystallization synergy, with the final aim of obtaining a reliable joining able to operate at 500 – 550°C.
Moreover, the printability and the optimization of the glassy paste were also a matter of study, since this kind of system needs precise and controlled encapsulation, difficult to obtain with a classical screen printing.

4.1.1 Optimization of the joining thermal treatment

The thermal treatment for the joining has been deduced and developed according to the following characterization: (1) differential scanning calorimetry (DSC) and thermogravimetric analyses (TGA); (2) temperature x-ray powder diffraction (XRD); (3) hot stage microscopy (HSM); (4) evaluation of the partial results and choice of two main strategies; (5) scanning electron microscopy (SEM) together with (6) energy dispersive x-ray spectroscopy (EDS); (7) dilatometry.

4.1.1.1 Differential scanning calorimetry

Figure 4-5 shows the DSC and TGA obtained from the glass powder at IREC. The measurements have been performed with a constant heating rate (3°C/min) from room temperature (RT) to 800°C, the maximum value achievable by the instrument. The weight of the powders has reduced of only 0,132 mg due to the volatile species. The first exothermic peak of 50 J/g is related to the glass transition phenomenon; indeed, the ending temperature is the T_g (around 560°C).

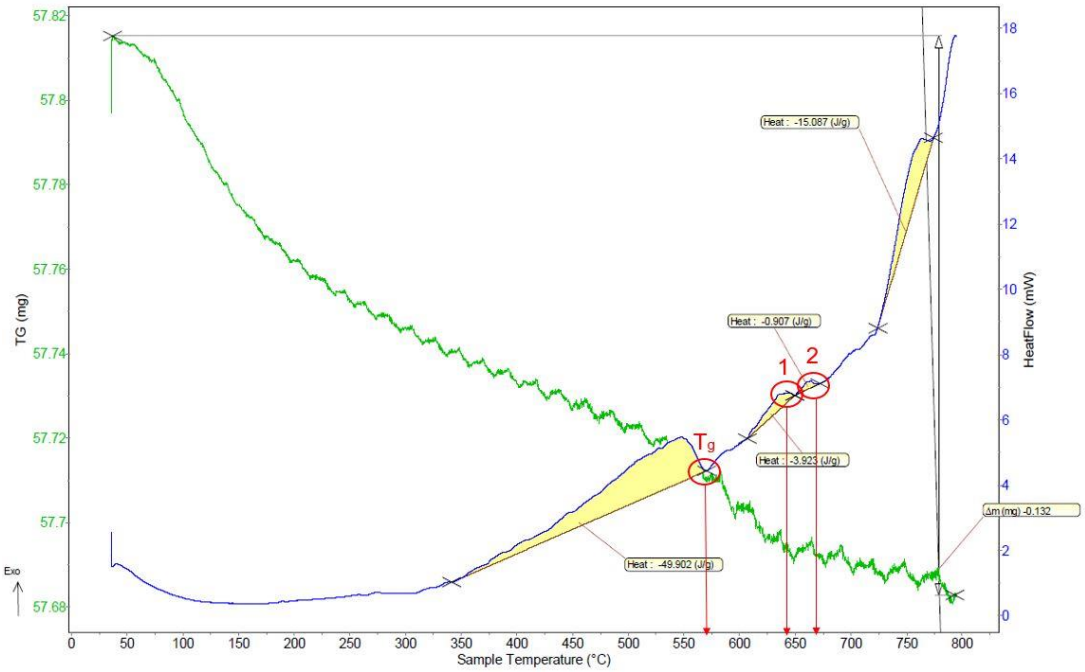

Figure 4-5. DSC results on glass powder.

The following exothermic peaks, T_p around 650°C and 675°C could be related to crystallization formations within the glass, but since their associated energy is low, an XRD has been performed. At the end of the measurement, the exothermic peak reveals another crystallization which would be probably greater than the previous ones.

4.1.1.2 Temperature x-ray powder diffraction

Firstly, an XRD analysis has been performed on glass powder to verify the amorphous behaviour at room temperature (RT). Indeed, figure 4-6 does not show any peaks. The measurement has been limited between 30° to 65° of 2θ (diffraction angle) to avoid the silicon peak around 28°.

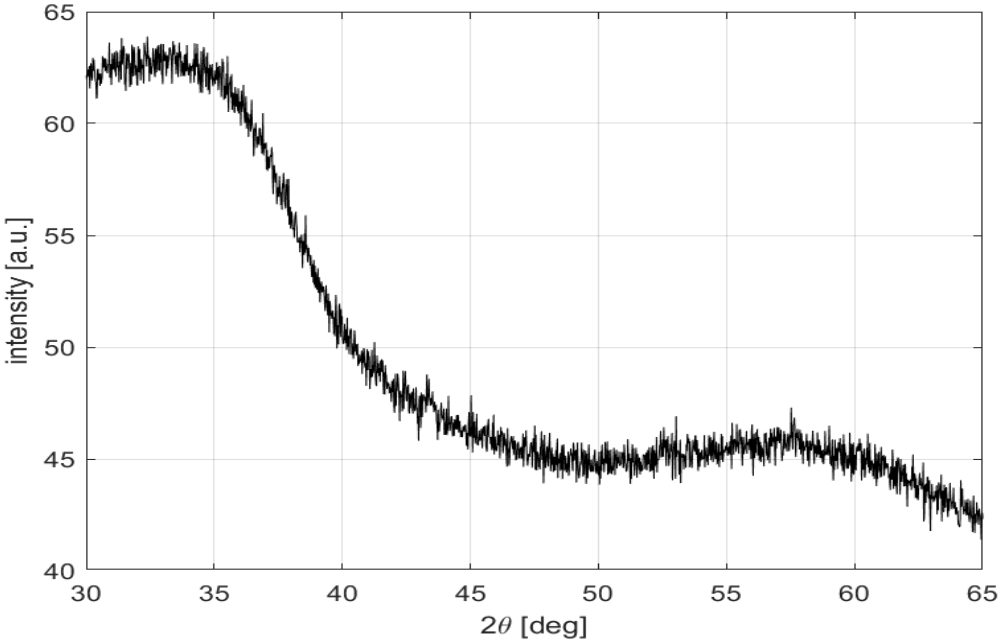

Figure 4-6. XRD on glass powder.

Afterwards, a high temperature XRD on the glass has carried out in order to verify the possible crystallization phenomena highlighted from the DSC analysis. To study the glassy paste (powder + binder) sealant post-treated, it was necessary to find a deposition technique able to leave the sample completely flat. Spin coating was tried but a non-homogeneous distribution of the paste was obtained (with a higher amount of material in the edges). Therefore, a doctor blade was adopted to spread a thin layer of sealant on 1 cm silicon chip, as shown in figure 4-7.
Since the measurement needs a perfect flat surface of the sample, a doctor blade was used, spreading a thin layer of paste on 1 cm square silicon chip. After dried, the sample has been positioned in the heating stage of the XRD, then a thermal cycle has been set as follow:

- XRD measurement at RT;
- Rapid rump up (10°C/min) until 600°C;
- Tests performed every 25°C from 600°C to 725°C with a heating rate of 3°C/min;
- Final measurement at 800°C;
- Cooling down to RT;

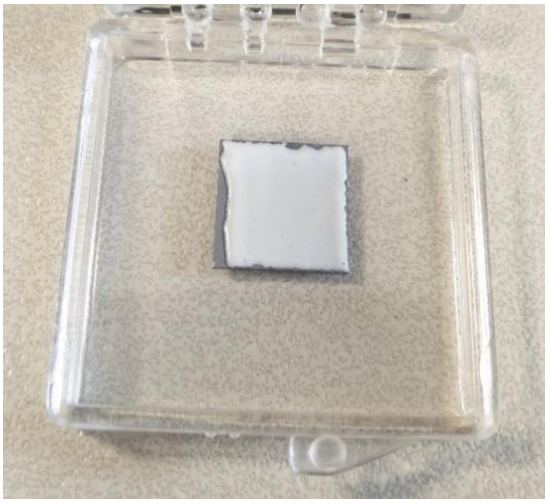

Figure 4-7. Glass sealant deposited with doctor blade.

Figure 4-8 shows the results. Until 600°C (blue curve) – 650°C (red curve) the glass sealant maintains an amorphous structure. From 675°C, the measurement revealed some diffraction peaks which probably represents crystallization forms. As the temperature increases the intensity and the number of peaks increases. During the cooling, no differences were noticed respect the highest temperature measurement.

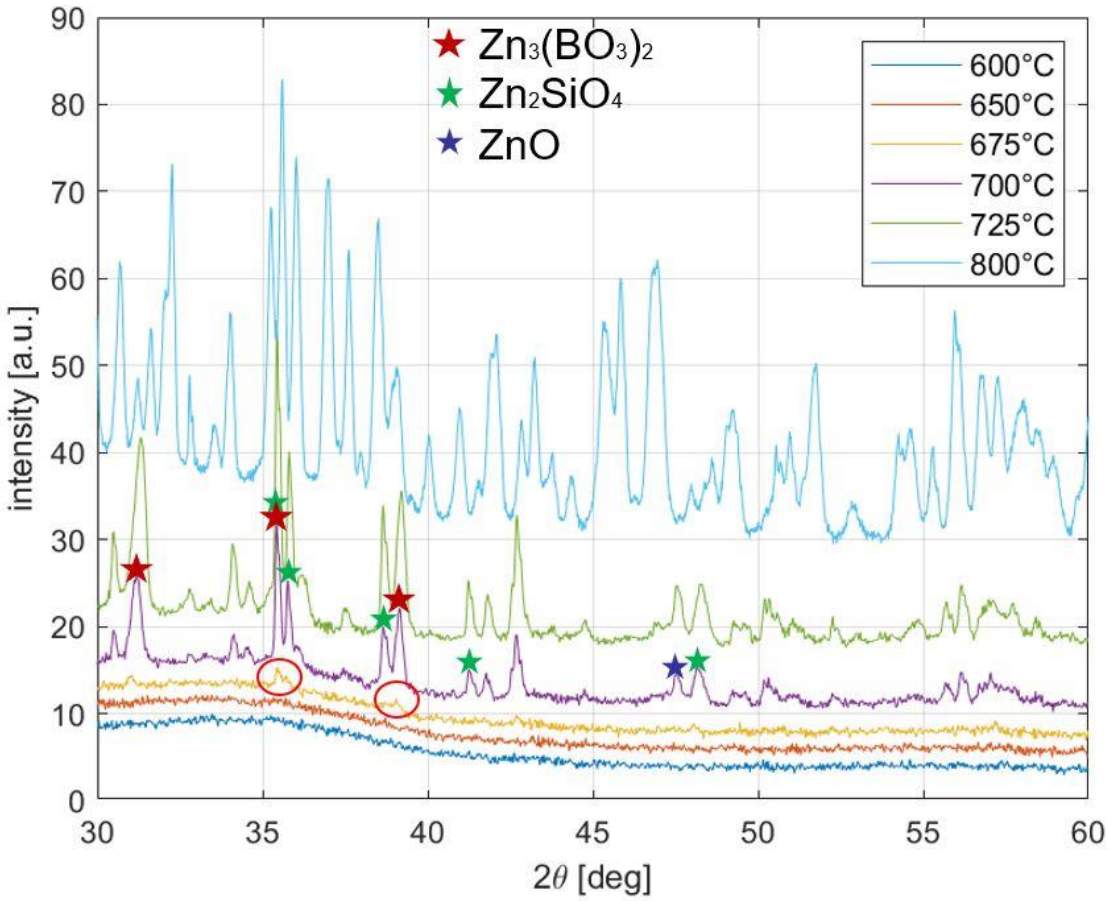

Figure 4-8. High temperature XRD.

The peaks analysis with *X'Pert HighScore Plus* software was complex, because of the huge amount of crystallizations as well as the several possible crystalline phases (from the initial chemical composition given by SCHOTT). As primary evaluation, the following phases are considered:

- Triclinic or tetragonal SiO_2 (ref code: 01-081-0067);
- Boron oxide, B_2O_3 (ref code: 00-003-0888);
- Zinc oxide, **ZnO** (ref code: 00-003-0888);
- Zinc silicates, $ZnSiO_3$ or $\mathbf{Zn_2SiO_4}$ (Ref code: 00-019-1479);
- Zinc borate, $\mathbf{Zn_3(BO_3)_2}$ (Ref code: 00-027-0983).

Figure 4-8 represents only the highlighted species, because a following SEM analysis, which will be describe later, showed a huge amount of zinc in the crystalline conglomerations. As a final comment, a variation of colour was observed on the treated sample, probably due to its structural change.

4.1.1.3 Hot stage microscopy

HSM was performed at POLITO on glass powder, adopting a heating rate of 3°C/min from RT to 800°C. The main parameters measured during the analysis are summarized in table 4-2.

Table 4-2. Main HSM parameters.

Symbol	Meaning	Measurement unit
T	Temperature	°C
t	Time	S
A	Area object	%
F_1	Form factor	-
h	Height	%
w	Width	%

Figure 4-9 shows a constant specific volume (% shrinkage) of the sealant until the *sintering temperature* (SIN), where the first shrinkage appears (the width of the sample decreases). Then, a fast decreasing of area object occurs until the *deformation temperature* (DT), i.e. around 620°C, where the pellet begins to soften. In this phase, at list 25% of specific volume undergoes a decreasing step. Afterwards, the volume remains constant up to 660°C where a deep volume decreasing follows. The so called *sphere temperature* (ST), at 666,5°C, shows the first variation of sample shape, acquiring a spherical geometry.

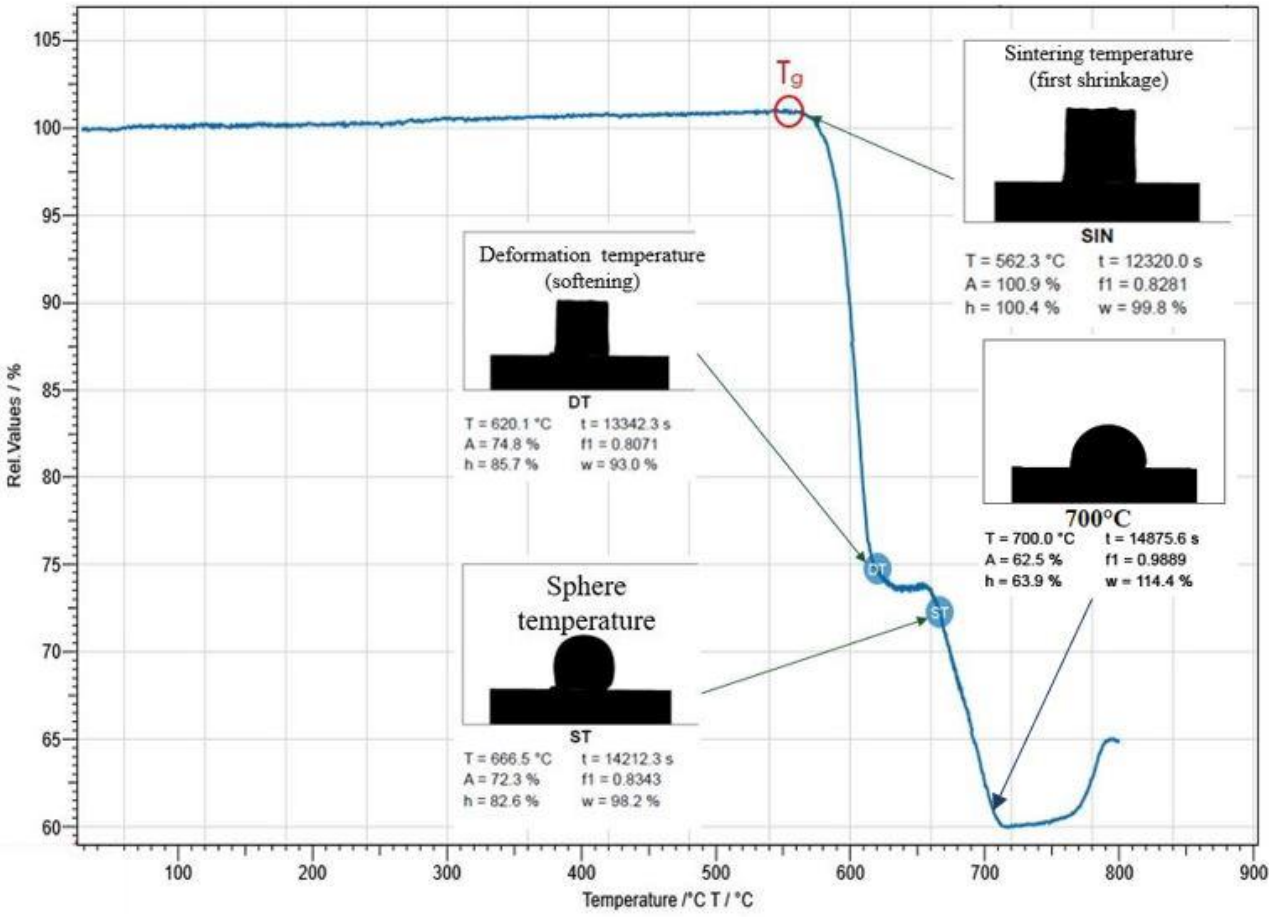

Figure 4-9. HSM results.

Reaching 700°C, the sample lost almost 40% of specific volume and hence it should be considered during the joining procedure. Increasing the temperature up to 800°C does not lead to a further volume decrease, instead the volatile species originated from the pellet cause a detrimental increase of volume which could determine bubbles and hence porosities in the final glass-ceramic.

4.1.1.4 Individuation of two strategies

The thermal treatment for the sealant joining adopted at the beginning is described in figure 4-3. Basically, it had two dwelling temperature as suggested by SCHOTT, one at 557°C and the other at 675°C. However, the analysis described before gave important results on the sealant crystal structure before and after being thermal treated and the shrinkage behaviour dependence with temperature. The temperature XRD showed possible crystalline formations from 675°C, while the HSM proved two significant specific volume decreasing, from 560°C to 620°C and from 660°C to 710°C. Therefore, two different strategies for the thermal treatment were considered, as shown in figure 4-10.

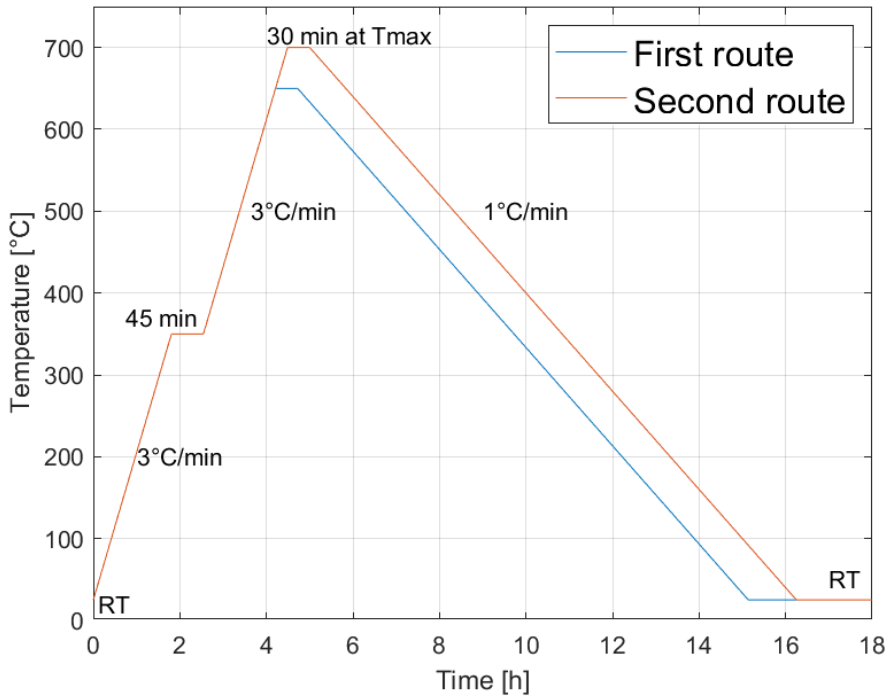

Figure 4-10. Two different strategies tested for the thermal treatment.

First, a dwelling time (45 min) at lower temperature (350°C, lower respect the previous one, 557°C) has been chosen. This step should lead to the binder decomposition thus allowing its degassing from the sealing. Next, the strategies differ as follow:

1. First route adopts a T_{MAX}=650°C, between DT and ST. It should guarantee a good adhesion between the silicon wafers and prevent the formation of any crystallize phases;
2. Second route adopts T_{MAX}=700°C, reaching the crystalline formation field and obtaining a higher shrinkage respect the first route.

In both cases/routes, it was decided to skip the dwelling at 557°C.

In order to guarantee a hermetic joining a suitable thermal treatment (TT) as well as a reproducible thickness of the sealant and its homogeneity throughout all the perimeter of deposition are necessary. Since the thickness scale of the single chip composing the device is around 500 µm, the sealing should be around 100 – 200 µm. To control the thickness by limiting an excessive shrinkage due to the viscous flow, some spacers were used, placed between the silicon chips. Afterwards a built-in step design in the silicon chips has been considered, obtained by micro fabrication etching process [49]. Figure 4-11 resumes the joining process and shows the 100 µm chips used as spacers. In the final setup the micro etched silicon chips will be used. It is worth to mention that it is necessary to leave the solvent drying before performing the joining, making the process compatible with clean-room regulations.

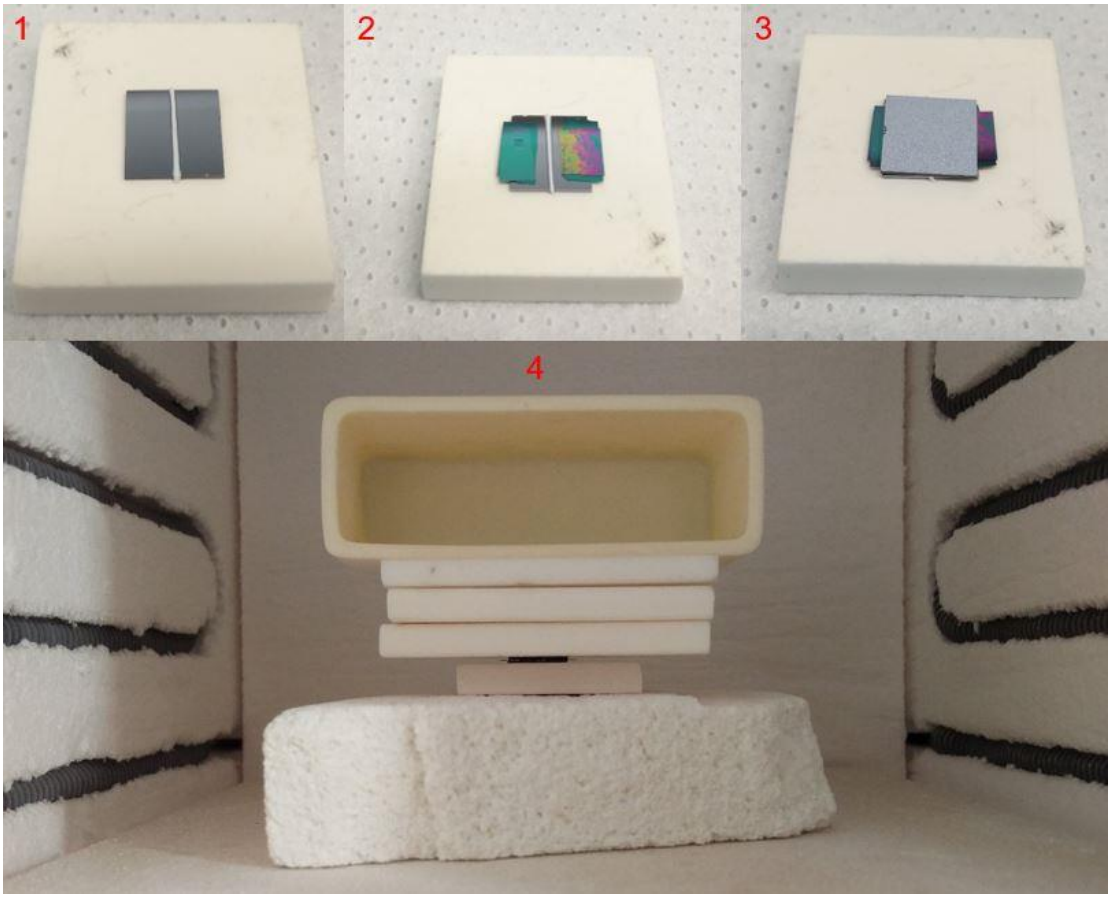

Figure 4-11. Joining steps.

Subsequently, a joining pressure has been adopted to ensure levelling of the chips and a homogeneous contact with the sealing. The pressure has been estimated in the range of 200-300 mbar applied between the two substrates by evaluating the scaled-up process. Experimentally, a g weight was placed on top of a silicon chip.

Comparing the following characterizations of the different strategies chosen, relevant results were obtained regarding the glass evolution into a glass-ceramic sealant for the joining. Indeed, crystallization in the glass matrix could guarantee stability in terms of viscosity variations, but of course it would also modify the CTE. So, it is important to handle as much as possible these two parameters by considering both the joining temperature and the operational temperature of the final micro-SOFC device.

4.1.1.5 Scanning electron microscopy

SEM images, performed both at POLITO and IREC, confirmed the DSC and temperature XRD analyses in terms of micro-structural and compositional differences of the two routes used for the joining TT. The paste was deposited with LDM technique on the samples, which are cut transversely with a diamond saw, after being thermal treated. Figure 4-12 and figure 4-13 shows significantly the absence of crystallization formations in the former (sealing heat treated at 650°C) and the presence of crystal clusters in the latter (sealing heat treated at 700°C). The

conglomerations measured are in the range of 3 – 5 µm to some tens of µm. Looking at the closed porosities present in figure 4-12 (a), 4-13 and 4-14 (b), the difference between the two thermal treatments is clear. In both cases, a good wetting and adhesion with the silicon surfaces were obtained, revealing the quality of the joining procedure.

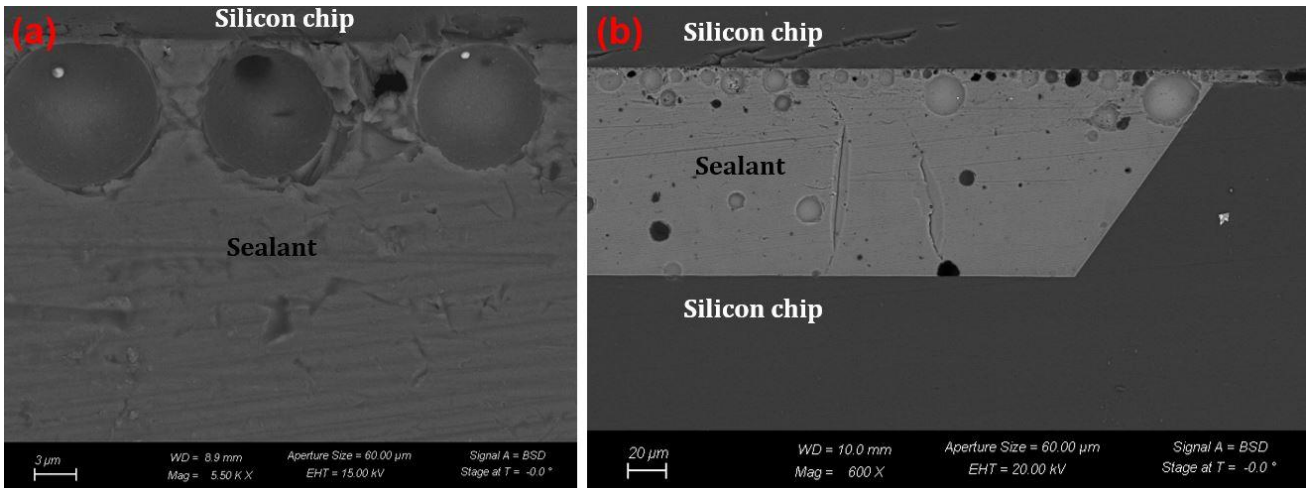

Figure 4-12. SEM images performed at POLITO to the joining post-treated sealant at T_{Max}=650°C.

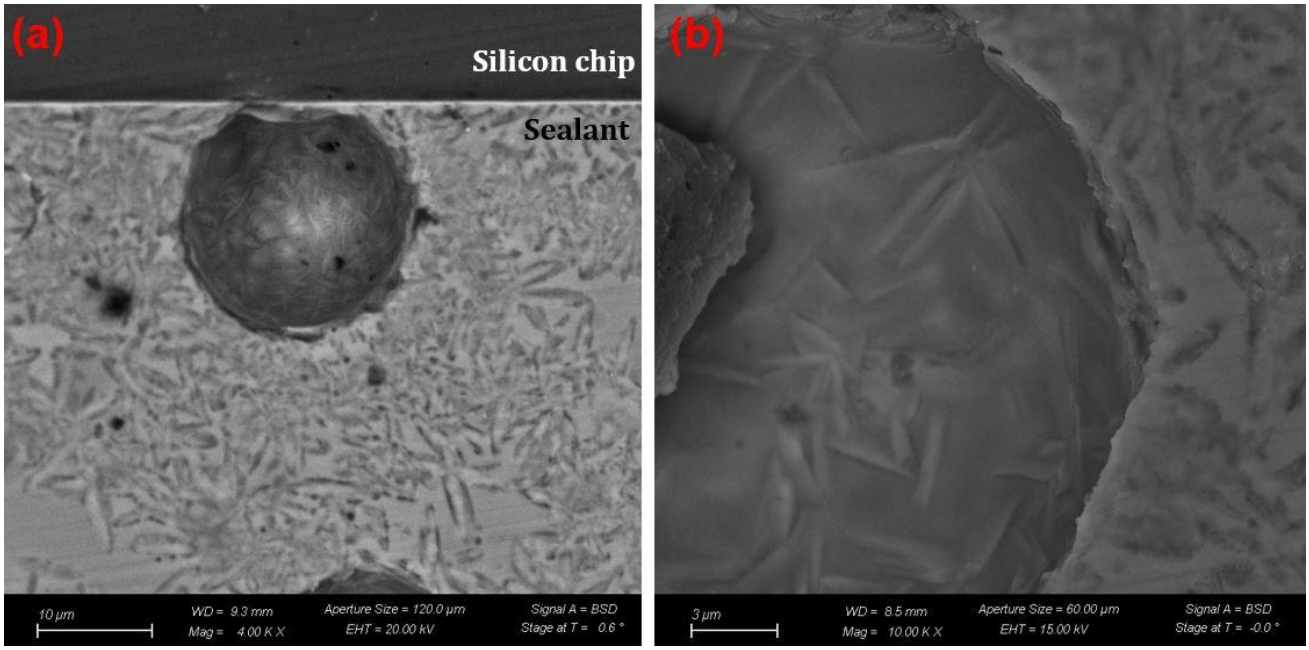

Figure 4-13. SEM images performed at POLITO to the joining post-treated sealant at T_{Max}=700°C

The thickness, around 100 µm, was controlled both with the micro etched shoulder, as shown in figure 4-12 (b), and with the spacers, as shown in figure 4-14 (a).

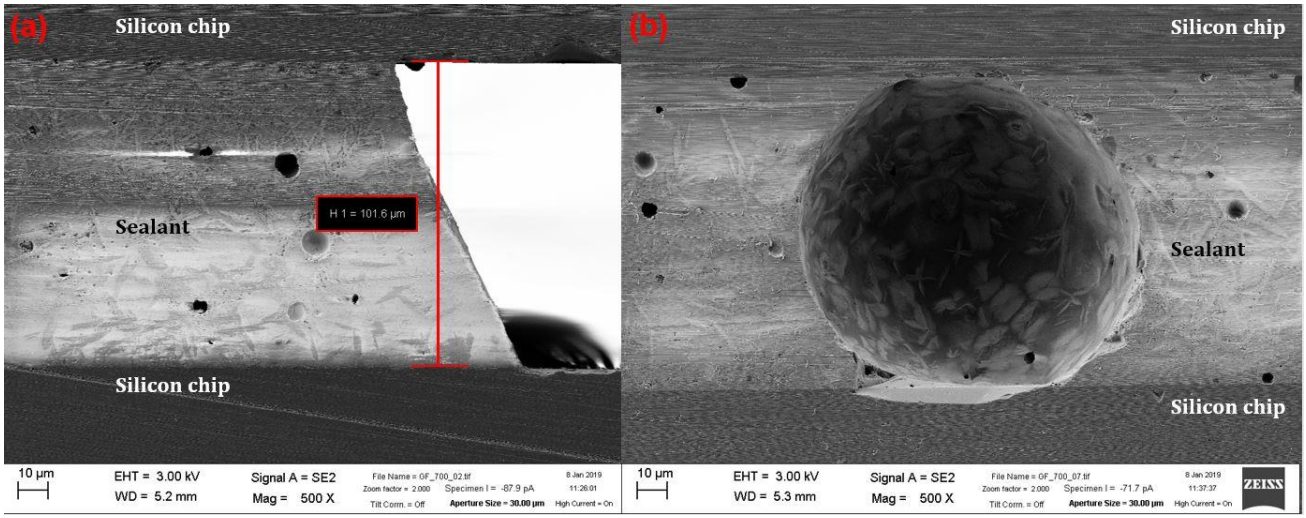

Figure 4-14. SEM images performed at IREC to the joining post-treated sealant at T_{Max}=700°C

4.1.1.6 Energy dispersive x-ray spectroscopy

EDS analyses performed at POLITO showed some differences between the thermal treatments adopted and also between closed porosity sites and bulk composition in the same joining sealant. Figure 4-15 shows the spectra analysed on the sealant treated at 650°C. Through *Inca* software, all the possible elements in the glass were considered. The results are resumed in tables 4-3 and 4-4, for the closed porosity analysis, and table 4-5, for the bulk composition. The measurements on bulk composition revealed a negligible presence of boron despite of a higher amount of zinc respect to the porosity detections, while the atomic presence of boron in the closed porosities is higher with respect the atomic percentage of zinc.

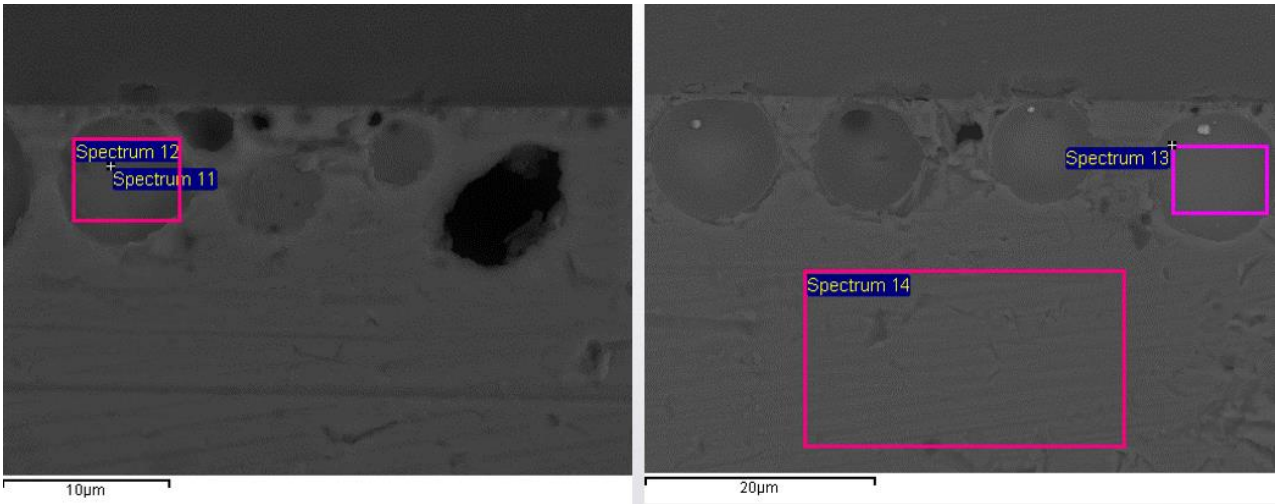

Figure 4-15. EDS analysis on sealant post-treated at T_{Max}=650°C, performed at POLITO.

Table 4-3. EDS on closed porosity sites, in the sealant heat treated at 650°C.

Spectrum 11			Spectrum 12			Spectrum 13		
Element	Weight %	Atomic %	**Element**	Weight %	Atomic %	**Element**	Weight %	Atomic %
B	14,73	27,61	**B**	11,4	23,93	**B**	13,89	26,58
C	8,37	14,12	**C**	7,14	13,49	**C**	7,67	13,21
O	34,89	44,2	**O**	30,75	43,64	**O**	31,08	40,18
Si	3,33	2,41	**Si**	3,54	2,86	**Si**	12,86	9,47
Zn	37,07	11,49	**Zn**	45,77	15,9	**Zn**	32,8	10,38
Ce	0,27	0,04	**Ce**	0,37	0,06	**Ce**	0,21	0,03
Bi	1,34	0,13	**Bi**	1,04	0,11	**Bi**	1,48	0,15

Table 4-4. Average EDS results on closed porosity sites, in the sealant heat treated at 650°C.

	Average (11;12;13)		Standard deviation	
Element	Weight %	Atomic %	Weight	Atomic
B	13,34	26,04	1,41	1,55
C	7,73	13,61	0,50	0,38
O	32,24	42,67	1,88	1,78
Si	6,58	4,91	4,44	3,23
Zn	38,55	12,59	5,40	2,38
Ce	0,28	0,04	0,07	0,01
Bi	1,29	0,13	0,18	0,02

Table 4-5. EDS results on bulk composition, in the sealant heat treated at 650°C.

Spectrum 14		
Element	Weight %	Atomic %
B	0,00	0,00
C	0,00	0,00
O	35,51	61,78
Si	19,79	19,61
Zn	43,24	18,41
Ce	0,00	0,00
Bi	1,46	0,19

A different chemical composition was found on the post treated sealant at 700°C. Figure 4-16 shows the spectra analysed both on closed porosities and bulk sites, as before. Tables 4-6 and 4-7 refer to the porosity sites analyses, while table 4-8 resumes the results on bulk composition. The atomic content of zinc and boron changed respect the previous results. As a comparison, the average atomic percentage of zinc in the closed porosities has increased four times respect the heat treatment at 650°C. Moreover, the difference between bulk composition and porosity sites, in the post treated sealant with 700°C, consists on the different distribution of B and Zn. The quantity of these two elements varies significantly in these analyses, highlighting a directly connection with the DSC, the XRD and the SEM measurements.

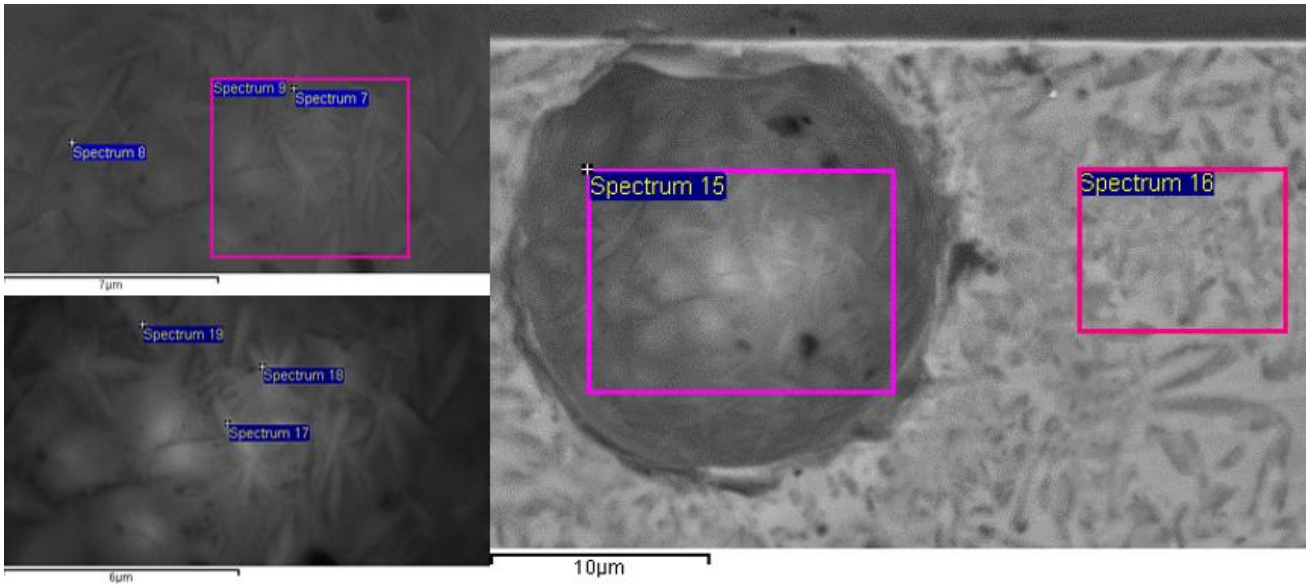

Figure 4-16. EDS analysis on sealant post-treated at T_{Max}=700°C, performed at POLITO.

It is possible to conclude that the glass-ceramic obtained from the thermal treatment at 700°C is basically composed of Zn and B compounds with the other elements present in the sealing structure, giving raise to the following crystalline phases: zinc oxide (**ZnO**), boron oxide ($\mathbf{B_2O_3}$), zinc borate ($\mathbf{Zn_3(BO_3)_2}$).

Table 4-6. EDS results on closed porosities, in the sealant heat treated at 700°C.

Spectrum 7			Spectrum 8			Spectrum 9		
Element	**Weight%**	**Atomic%**	**Element**	**Weight%**	**Atomic%**	**Element**	**Weight%**	**Atomic%**
B	0,00	0,00	**B**	4,85	10,62	**B**	0,00	0,00
C	0,00	0,00	**C**	0,00	0,00	**C**	0,00	0,00
O	9,51	29,56	**O**	47,40	70,08	**O**	10,41	31,72
Si	1,58	2,80	**Si**	4,23	3,56	**Si**	1,68	2,92
Zn	88,91	67,64	**Zn**	43,52	15,75	**Zn**	87,51	65,27
Sb	0,00	0,00	**Sb**	0,00	0,00	**Sb**	0,00	0,00
Ce	0,00	0,00	**Ce**	0,00	0,00	**Ce**	0,00	0,00
Bi	0,00	0,00	**Bi**	0,00	0,00	**Bi**	0,40	0,09
Spectrum 17			**Spectrum 18**			**Spectrum 19**		
Element	**Weight%**	**Atomic%**	**Element**	**Weight%**	**Atomic%**	**Element**	**Weight%**	**Atomic%**
B	3,76	13,89	**B**	0,00	0,00	**B**	2,96	11,09
C	3,66	12,16	**C**	0,00	0,00	**C**	3,37	11,37
O	8,87	22,12	**O**	10,72	32,48	**O**	9,52	24,10
Si	1,18	1,68	**Si**	1,53	2,64	**Si**	1,85	2,66
Zn	81,93	50,00	**Zn**	87,25	64,72	**Zn**	81,63	50,60
Sb	0,08	0,02	**Sb**	0,10	0,04	**Sb**	0,17	0,06
Ce	0,30	0,09	**Ce**	0,20	0,07	**Ce**	0,21	0,06
Bi	0,21	0,04	**Bi**	0,20	0,05	**Bi**	0,30	0,06

Table 4-7. Average EDS results on closed porosity sites, in the sealant heat treated at 700°C.

	Average		Standard deviation	
Element	**Weight%**	**Atomic%**	**Weight**	**Atomic**
B	1,93	5,93	2,00	6,02
C	1,17	3,92	1,66	5,55
O	16,07	35,01	14,02	16,13
Si	2,01	2,71	1,01	0,55
Zn	78,46	52,33	15,87	17,80
Sb	0,06	0,02	0,06	0,02
Ce	0,12	0,04	0,12	0,04
Bi	0,19	0,04	0,15	0,03

Table 4-8. EDS results on bulk composition, in the sealant heat treated at 700°C.

Spectrum 15			Spectrum 16		
Element	**Weight%**	**Atomic%**	**Element**	**Weight%**	**Atomic%**
B	10,24	22,65	**B**	46,39	60,36
C	6,19	12,33	**C**	14,04	16,55
O	29,54	44,15	**O**	21,08	18,66
Si	2,75	2,34	**Si**	1,48	0,70
Zn	50,23	18,38	**Zn**	16,26	3,52
Sb	0,25	0,05	**Sb**	0,09	0,01
Ce	0,23	0,04	**Ce**	0,15	0,02
Bi	0,58	0,07	**Bi**	0,50	0,03

Finally, a mapping of the sealant treated at 700°C has been performed at IREC, which confirmed the abundant presence of Zn, as shown in figure 4-117. In this measurement, gold was sputtered on the sample forming a conductive layer which enhance the quality of the images obtained.

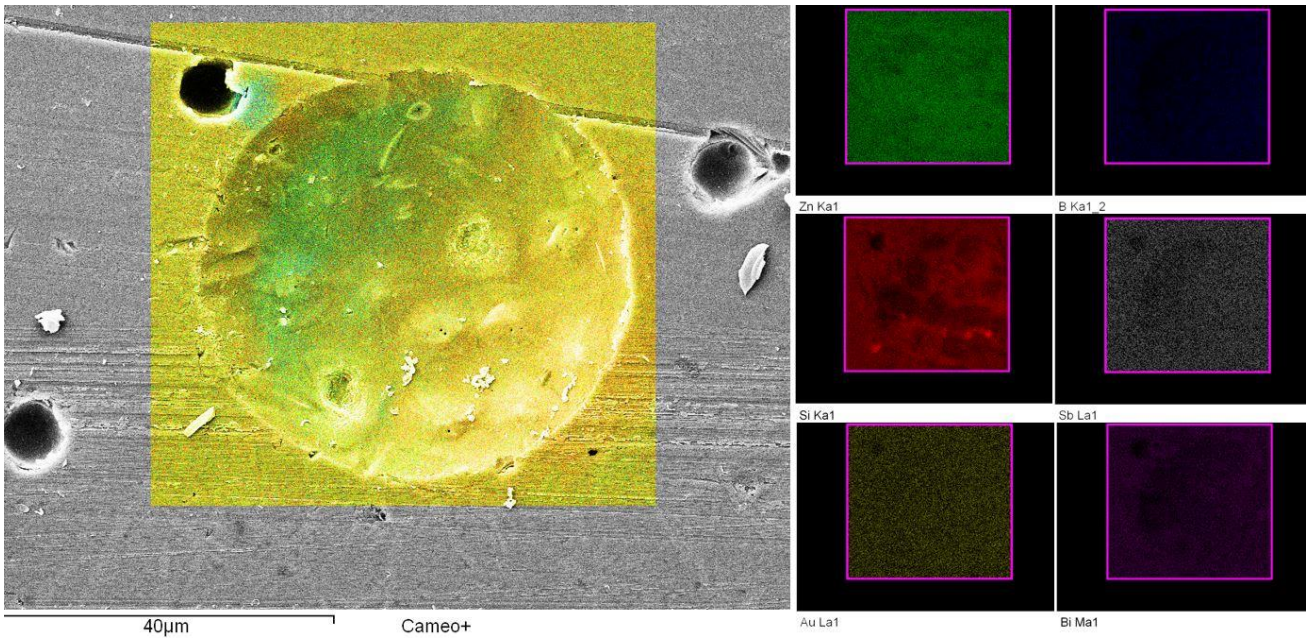

Figure 4-17. EDS analysis on sealant post-treated at T_{Max}=700°C, performed at POLITO.

4.1.1.7 Dilatometry measurements

The sealant will be applied in the final device to join different components and guarantee thermochemical integrity at the operation temperature (around 550°C) as well as during the thermal cycles due to switch on/off operation. Therefore, it is fundamental an almost perfect matching with silicon CTE, since Si is the main substrate used for the micro-SOFC. Figure 4-18 shows the variation of thermal expansion coefficient after the treatment of the three thermal routes adopted in this work. The red curve represents the initial thermal treatment used for the joining, which has been chosen following the glass data sheet. The green curve represents the first thermal treatment with a maximum temperature of 650°C while the blue curve represents the thermal treatment with a firing temperature of 700°C.

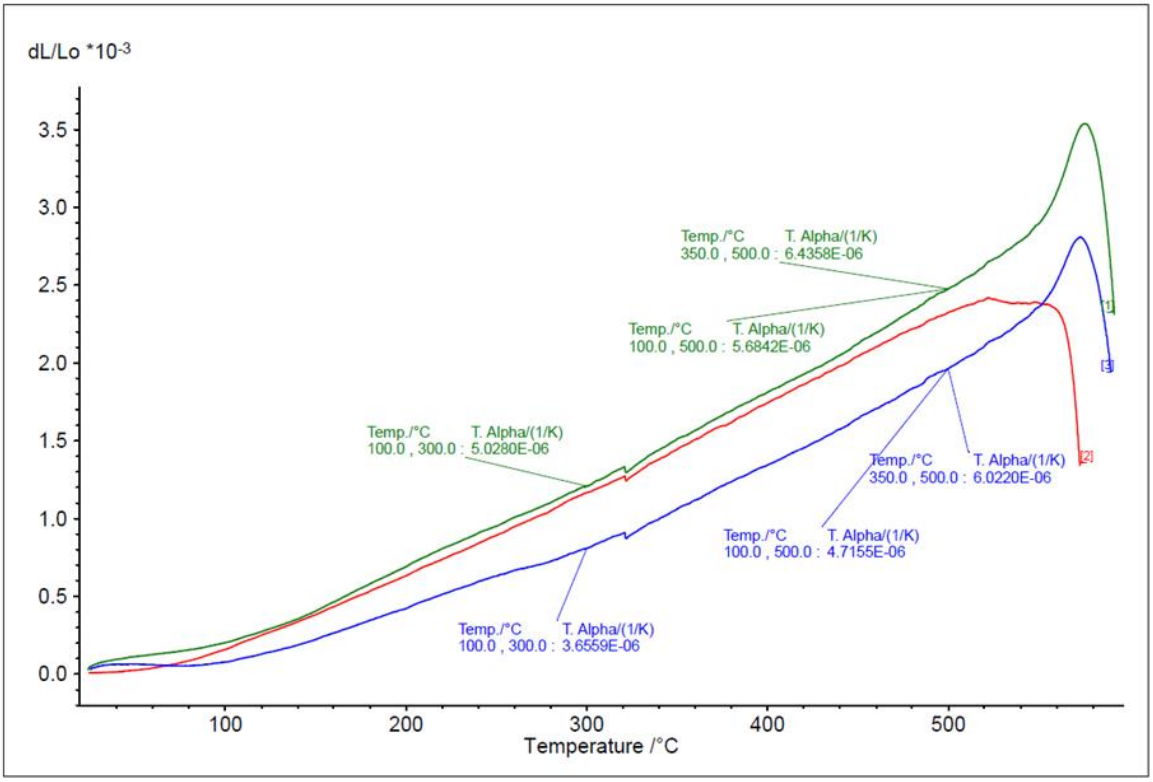

Figure 4-18. Dilatometry measurements performed at POLITO.

The results on dilatometry tests performed at POLITO are resumed in table 4-9.

Table 4-9. Different CTE obtained from post treated glass sealant.

Thermal treatment adopted	CTE [10^{-6} K^{-1}]
Initial treatment	5,41
First route (T_{MAX}=650°C)	5,68
Second route (T_{MAX}=700°C)	4,72
SCHOTT data sheet	4,4

The most interesting aspect of this graph is that two different joining treatments and the consequent crystallization could affect on the thermo-mechanical properties of the final sealant.

The thermal treatment at 700°C shows the lowest CTE, closest to the silicon one as shown in table 4-10, which tabulates the variation of silicon CTE with temperature.

Table 4-10. Silicon CTE variation with temperature.

T (K)	α (10^{-6} K^{-1})	T (K)	α (10^{-6} K^{-1})
180	1.061	700	4.016
200	1.406	800	4.151
220	1.715	900	4.185
240	1.986	1000	4.258
260	2.223	1100	4.323
280	2.432	1200	4.384
300	2.616	1300	4.442
400	3.253	1400	4.500
500	3.614	1500	4.556
600	3.842	1600	4.612

As a conclusion, zinc borates, zinc silicates and zinc oxides, detected from the XRD and EDS measurements are the crystalline phases responsible of the CTE decreasing [63].
Figure 4-18 also gives the softening behaviour after each thermal treatment. As the curves begin to increase their slopes, so loosing the direct proportionality between length variation and temperature variation, the glass or glass-ceramic begins to soften. Therefore, the sample length, after a rapid increasing, reduces quickly. Since the measurements must be stopped with this phenomenon, it is not known the CTE behaviour above 600°C, therefore it could be considered as a maximum operating temperature of the sealant.
Final considerations on CTE were done, trying the joining treatment of the sealant on different surfaces: (1) between two Hoya glass chips and (2) between a silicon chip and an alumina support. The former did not show any structural variation after the thermal cycling, while the latter caused the breaking of the silicon chip, since the CTE of the sealant and the alumina is quite different. Therefore, the alumina support, used for the connection of the stack with the micro-reformer, will be joined with silicon using the anodic bonding technique.

4.1.2 Results on sealant deposition optimization

The route of deposition optimization has followed three steps: (1) study of the rheological properties of the glassy paste; (2) wettability tests of the binder on different surfaces; (3) enhancement of the liquid deposition modelling (LDM) systems.

4.1.2.1 Rheological properties

A Bohlin viscometer has been used to measure the viscosity behaviour of the paste (powder + binder). The results are resumed in figures 4-19 and 4-20.
Increasing the shear rate of the spindle, the viscosity of the paste decreased, proved the plastic behaviour of the sample. Moreover, at constant shear rate the viscosity also decreased as a function of time. This second test, shown in figure 4-20, proved the thixotropic behaviour. The

measurement has been performed with different shear rates, confirming the major decreasing of viscosity with a higher shear rate.

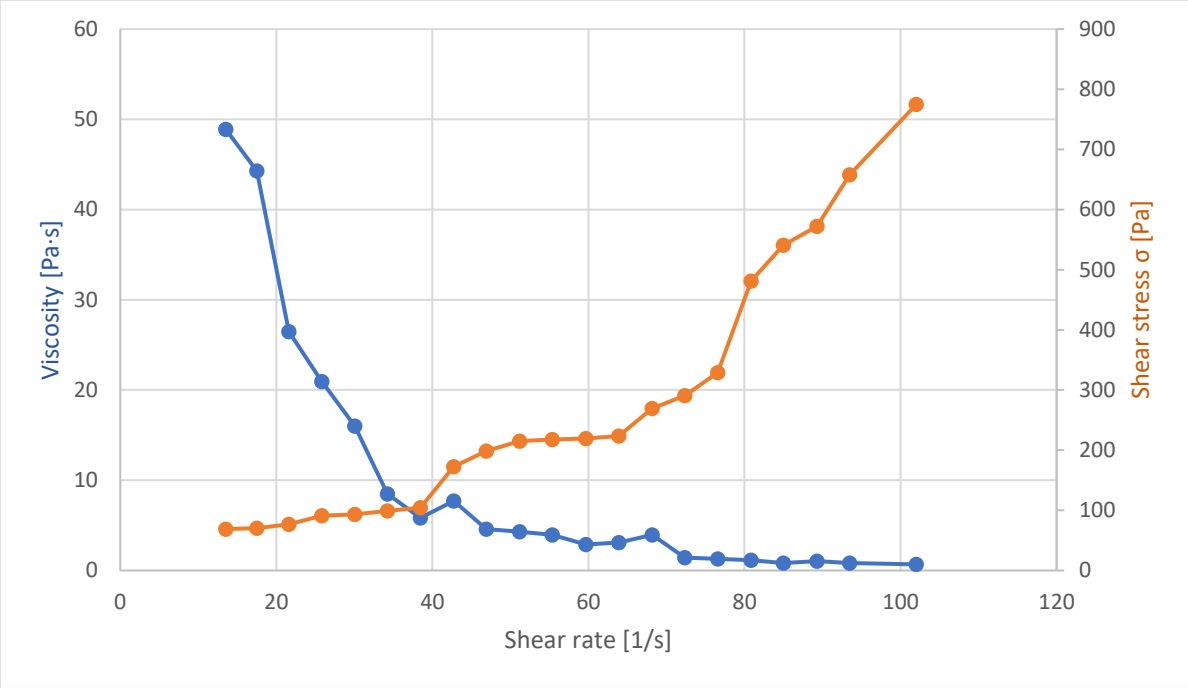

Figure 4-19. Plastic behaviour measured with a Bohlin viscometer at IREC.

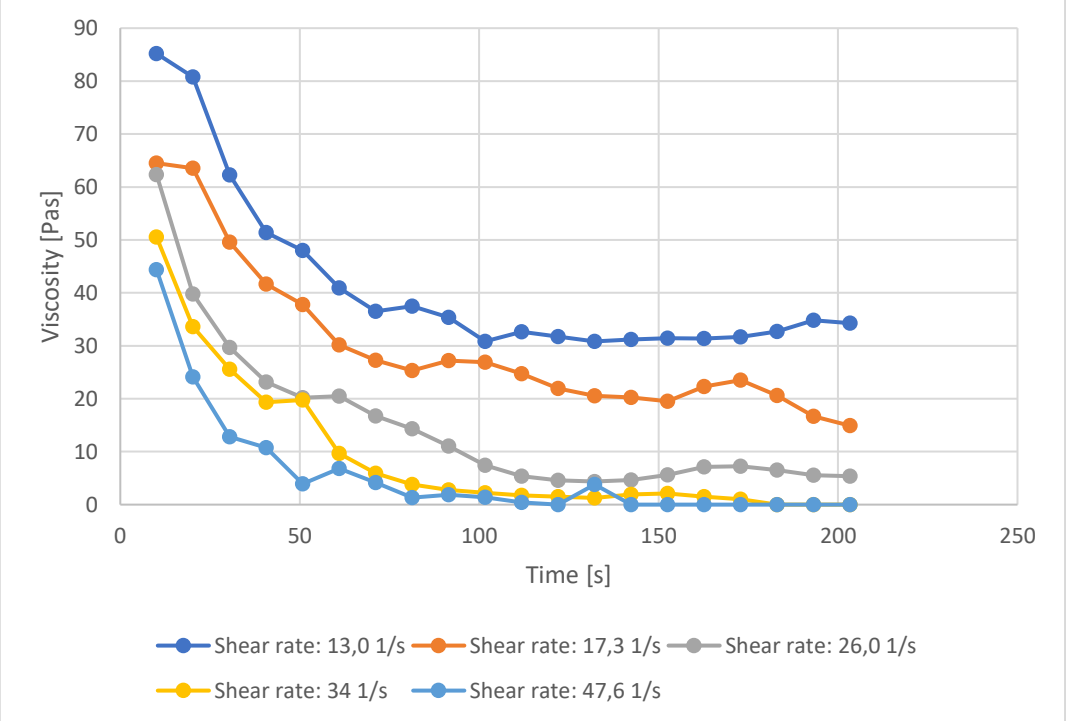

Figure 4-20. Thixotropic behaviour measured with a Bohlin viscometer at IREC.

4.1.2.2 Wettability tests

The wettability of the binder on different surfaces were tested. Figure 4-21 shows four different chips tested; since the molecule interactions occur only in the final layer of the chip, therefore the surfaces can be classified into four groups: (1) Silicon; (2) Si_3N_4; (3) Platinum sputtered; (4) HOYA glass. They represent the components which could be directly in contact with the sealant in the final device.

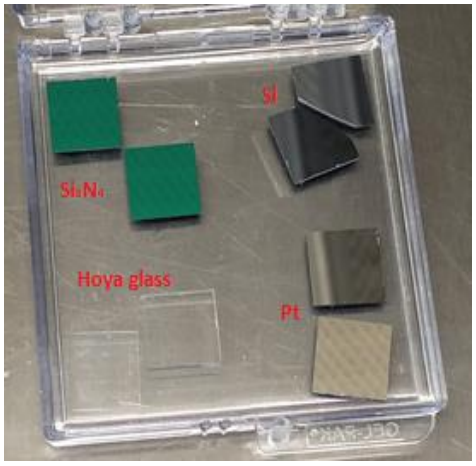

Figure 4-21. Four different surfaces tested (Silicon; Si_3N_4; Platinum sputtered; HOYA glass).

To determine the adhesion work and so the wettability, the binder surface tension (γ_{LV}) was measured through the pendant drop test, as shown in figure 4-22.

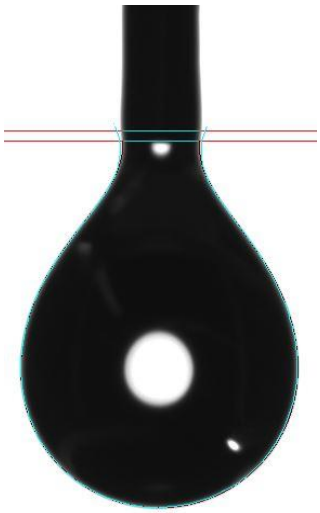

Figure 4-22. Pendant drop measurement.

The average value of γ_{LV} has been evaluated around 410 mN/m, as shown in table 4-11.

Table 4-11. Liquid surface tension measurements with pendant drop test.

Liquid surface free energy	Values	
Test 1	411,94	mN/m
Test 2	408,20	mN/m
Average	410,07	mN/m

The sessile drop tests, used to determine the wettability behaviour of the binder, were performed either with drop at rest on the measurement plate and either after 5 s of the drop contact with the plate. Table 4-12 resumes the average results, showing a good adhesion work (W_A) and low contact angles (CA) for each surface; therefore, in principle every type of chips should guarantee good adhesion and wettability with the sealing. Anyway, platinum showed the lowest value of CA and hence the highest W_A.

Table 4-12. Sessile drop results on different surfaces.

Si	**CA [°]**	**Wa (mN/m)**	**Ws (mN/m)**	**Si3N4**	**CA [°]**	**Wa (mN/m)**	**Ws (mN/m)**
After 5 s	43,00	709,47	-110,67	*After 5 s*	38,80	729,60	-90,54
Drop at rest	25,47	779,86	-40,28	*Drop at rest*	26,58	775,85	-44,29
Pt	**CA [°]**	**Wa (mN/m)**	**Ws (mN/m)**	**Hoya glass**	**CA [°]**	**Wa (mN/m)**	**Ws (mN/m)**
After 5 s	36,62	738,99	-81,15	*After 5 s*	40,11	722,55	-97,59
Drop at rest	17,44	801,24	-18,90	*Drop at rest*	25,72	779,51	-40,63

Clearly, the CA decreases with time, from the first measurement (after 5 s) to the equilibrium position at rest where the solid liquid and vapor phases satisfy the Young-Dupré equation. Figure 4-23 shows the drops after 5 minutes of dwelling time on different chips, confirming the good adhesion of all the surfaces.

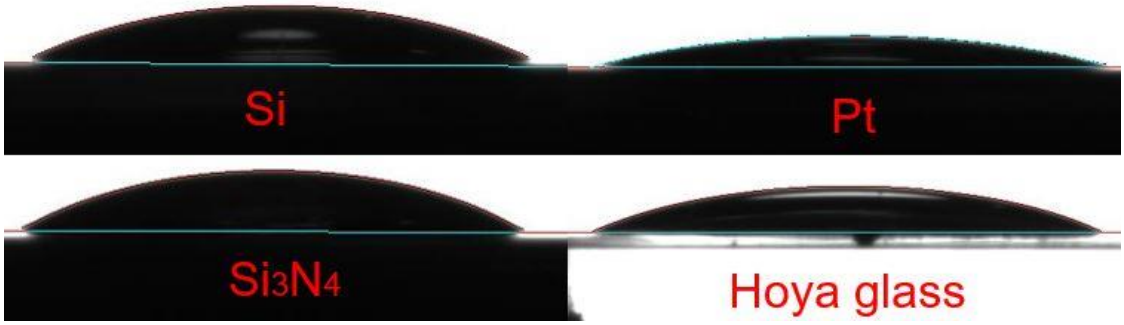

Figure 4-23. Sessile drop tests.

4.1.2.3 Liquid deposition modelling

The deposition system has been improved from the initial one, described before (figure 4-1), to the actual one represented in figure 4-24.

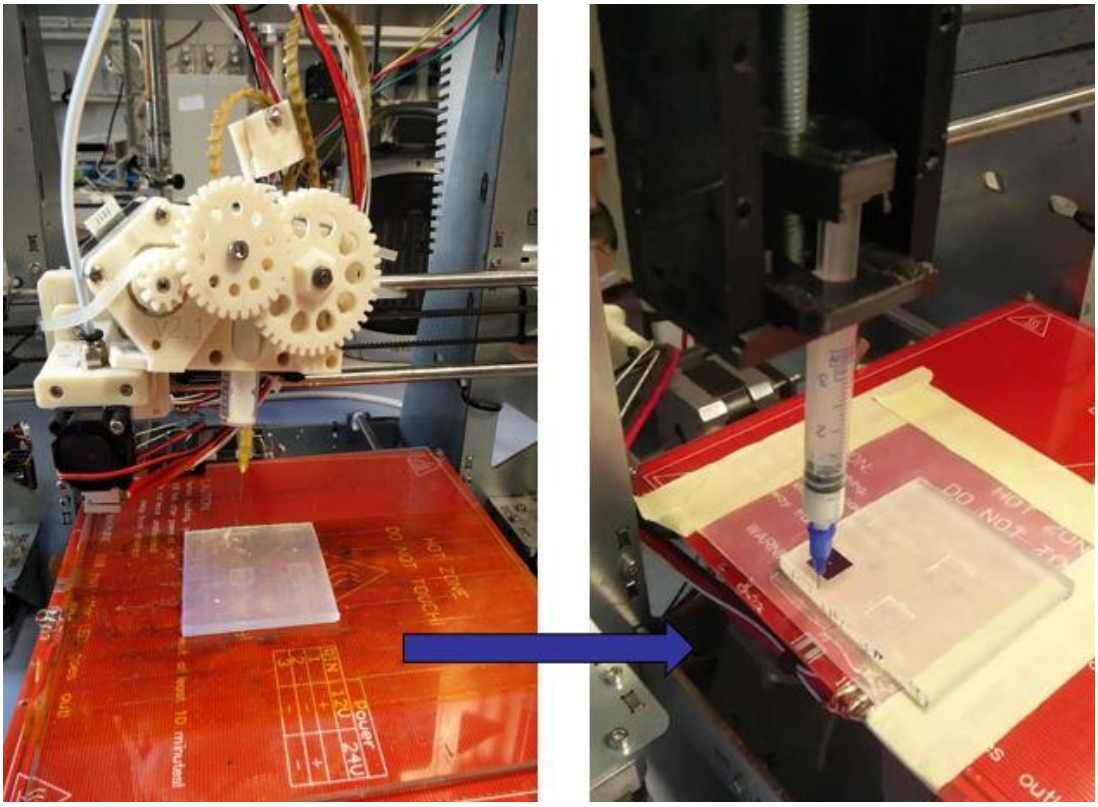

Figure 4-24. New LDM system

It is based on a retraction screw which is directly connected to the syringe piston, allowing a controllable extrusion of the paste and avoiding the continuous flowing without pressure. The quantity can be controlled with the *Cura* software as well as the perimeter path. With the optimization of the surface flatness together with the vertical axis (z direction) calibration, a fine and homogeneous line has been obtained. The deposition tests were performed with a 500 μm nozzle, varying mainly two parameters (the flow and the diameter) in the software. Each deposition was composed firstly by an external path where the paste is extruded out of the samples, in order to fill the nozzle and keep the sealant ready for the useful printing. Each chip was then registered to evaluate the parameters used and optimize them. The system velocity was set at 2 mm/s.

4.1.3 Discussion

The results obtained in this MSc thesis, related to the glass sealing, are significant in at least two major respects. First a comprehensive study of the sinter-crystallization behaviour, useful to be adopted in the sealing of the device, was carried out. Furthermore, the optimised joining heat treatment gave the possibility to obtain a glass-ceramic with a proper amount of residual glassy phase (softening point around 580°C), potentially useful to heal possible cracks formed during thermal cycles.

The sealant treated at 700°C represents the optimal joining procedure analysed in this work since it has several advantages with respect to the sealant thermal treated at 650°C.

- ✓ It confers a similar CTE with respect to the silicon one;
- ✓ Its shrinkage behaviour allows a higher volume reduction than the thermal treatment at 650°C; indeed, more than 15% of specific volume is gained by simply increasing the maximum firing temperature (about 50°C) of the treatment;
- ✓ It guarantees good adhesion and wettability with silicon as shown in the frame of figure 4-9;
- ✓ It shows low number of pores, thanks to a better degassing process during viscous flow sintering of the glass;
- ✓ Its thickness can be controlled and be reproduced with micro etched steps.

Zinc borates, zinc silicates, zinc oxides are the crystalline forms which contribute to the modification of the final properties. An operation temperature below of 600°C is recommended, since that the CTE of the sealant cannot be measured after the softening point.

A Further characterization could be considered to evaluate the sealant behaviour by changing the particle dimension. It could be measured with a Dynamic Light Scattering (DLS) and varied through a ball milling process. Other works showed different crystallization process formation by varying the particle size of the glass powders [48].
Further research should be undertaken to investigate the glass tightness of the joined area, i.e by hermeticity measurements. Despite SEM images revealed a quite uniform volume without porosities, tests in relevant conditions (with H_2 and O_2) are necessary. As a reference, the patent n. 6074891 [64] described a method to verify a hermetic sealant, based on a PN junction diode placed in a cavity encapsulated with a sealing.

4.2 Anode characterization results

Strontium doped lanthanum titanate ($Sr_{0,7}La_{0,3}TiO_3$, LST37) thin films were produced with pulsed laser deposition (PLD) to study the real behaviour and properties of the perovskite ceramic material as anode for micro-SOFC. This section resumes the results obtained as well as the possible improvements of the microstructure and functional properties of LST37.

First, a LST37 pellet of 1 inch diameter was produced by mechanical compression of commercial LST37 powder (provided by *Fuel cell materials*). In order to calculate the mass of powder necessary to produce the target with the desired dimensions, the theorical density of LST37 was calculated:

$$\rho_{th}\left[\frac{g}{cm^3}\right] = \frac{weight}{volume} = \frac{M_W[uma]}{N_A \cdot V[Å^3] \cdot 10^{-24}} \qquad (4.2)$$

Where N_A is the Avogadro number ($6{,}022 \cdot 10^{23}$ mol) and M_W the molar weight of the stoichiometric cell. The cell volume (V) was derived from the lattice parameter of the cubic perovskite structure measured by Singh et al. [54]. Table 4-13 resumes the main steps used for the calculation of pellet theorical density. In this way, knowing the desired target volume ($1{,}52 cm^3$), the minimum mass of LST powder necessary was calculated (8,437g).

Table 4-13. Theorical density and pellet mass calculation.

Calculation of theorical density		
Lattice parameter	3,9039	[A°]
Cell volume	59,501	[A°³]
La (57)	138,905	[g/mol]
Sr (38)	87,620	[g/mol]
Ti (22)	47,867	[g/mol]
O (8)	15,999	[g/mol]
Mw_{tot}	198,87	[uma] = [g/mol]
ρ_{th} (LST37)	**5,5501**	**[g/cm³]**
Dimensions PLD target		
Diameter	2,54	[cm]
Thickness	0,3	[cm]
Target volume	**1,52**	**[cm³]**
Theoric mass	**8,437**	**[g]**

The LST powder was then compressed two times by applying 8 MPa of pressure interspersed with a crumbling process with mortar and pestle, thus obtaining a compact cylindrical pellet. Afterwards the pellet was thermal treated with a firing temperature of 1400°C and a dwelling time of 8h. The sintering temperature (1400°C) was derived from literature [54, 71].

Then, the LST37 target produced was analysed by XRD, see Figure 4-25. The diffraction peaks matched with the expected cubic structure (pdf *01-079-0185*), with no evident secondary phases evinced. Considering the lattice parameter given by the pdf, the material's theorical density was

recalculated and corrected. This value was then confronted with the real density of the pellet (ρ_{real}), obtained by measuring the target's volume after the sintering and its weight. In this way, a density ratio ρ_{real}/ρ_{th}, around 76% was calculated.

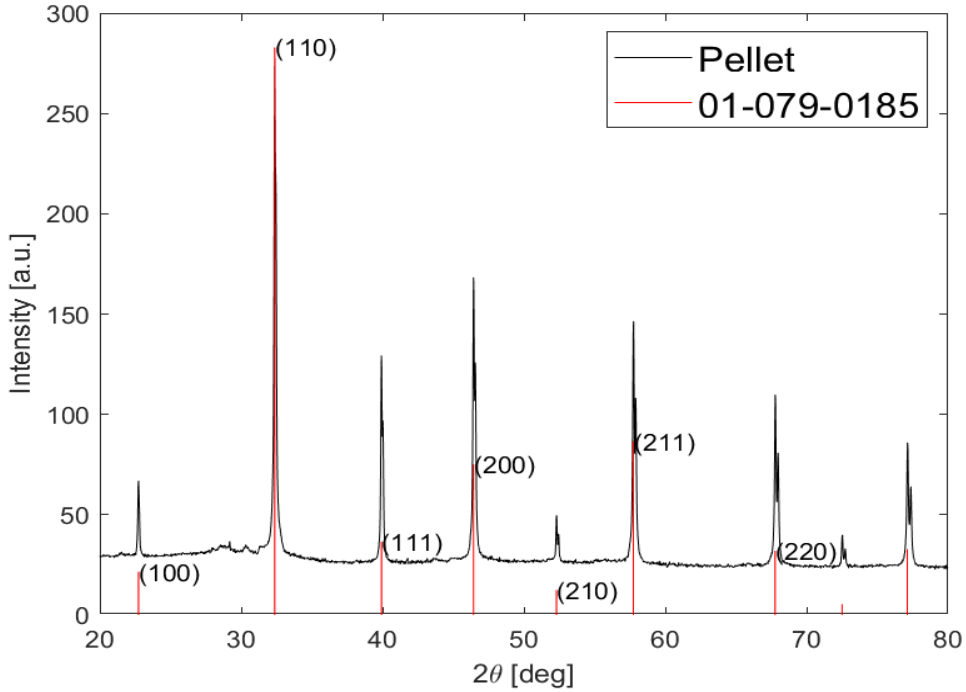

Figure 4-25. XRD of the LST pellet.

Figure 4-26 shows the pellet geometry and defects after the sintering process. The imperfect edges of the disc allowed us to consider a higher real density and hence a higher density ratio (> 80%), hence acceptable for PLD deposition. Indeed, a target density lower than 80% may results in a fast surface degradation, generating a high particle ejection during deposition [15].

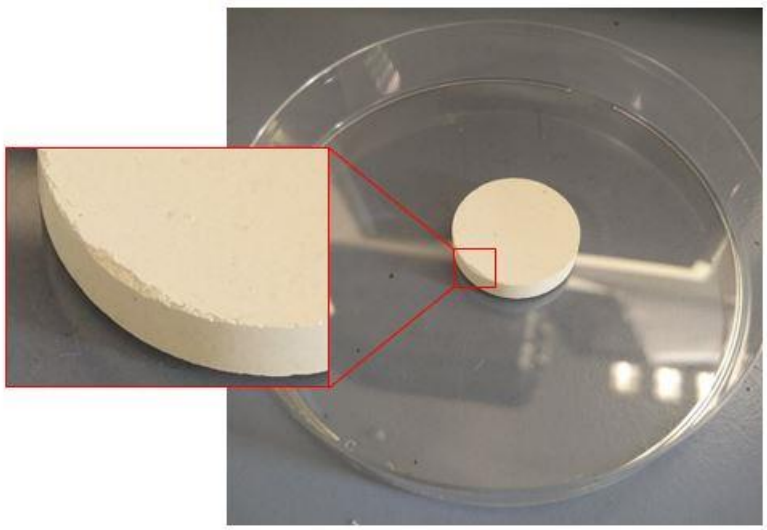

Figure 4-26. LST pellet geometry and edge defects.

As explained in section 3-2, the effect of the oxygen background pressure deposition on structural and functional film properties was investigated. Four different oxygen pressures were

adopted: 5 mtorr, 60 mtorr, 120 mtorr, 200 mtorr. The LST thin films were deposited on MgO (100) single crystals substrates at the fixed deposition temperature of 650°C, directly adapted from a previous study in literature [72]. The main deposition parameters adopted are resumed in table 3-1, section 3-2. Many efforts to fit the plume center with the substrate position were done, in order to obtain homogeneous film thickness. Since increasing the oxygen deposition pressure results in a decrease of layer's growing rate (due to a higher confinement of the plasma plume), the number of pulses was progressively increased for maintaining a constant thickness. In the next sections, the structural and electrical properties of the films are investigated.

4.2.1 Optical and structural properties

Ellipsometry measurements were performed to identify the thickness and roughness of the thin films deposited. Table 4-14 resumes the results. All the thicknesses ranged between 115 nm to 170 nm, with a considerable approximation as regard the 200 mtorr film measurement since its absolute error was considerable. As a first important comment, it is evident the huge roughness evolution measured increasing the deposition pressure in the thin films.

Table 4-14. Ellipsometry results on films size.

Pressure	Thickness [nm]	Roughness [nm]
5 mtorr	133 ± 3	0,5 ± 0,4
60 mtorr	116 ± 5	11,6 ± 5
120 mtorr	154 ± 7	14,5 ± 5
200 mtorr	171 ± 30	18,5 ± 15

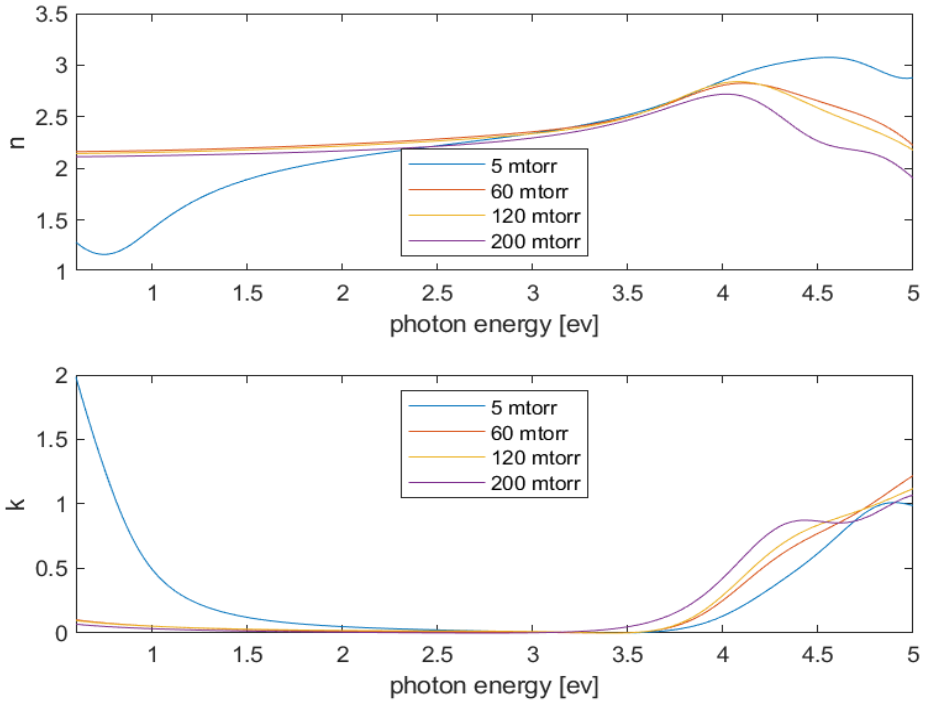

Figure 4-27. optical properties of thin films measured with ellipsometry.

Moreover, the optical properties (indexes n/k) of the films were measured with ellipsometry, as shown in figure 4-27. A difference in the low energy band gap (infrared) behaviour has been notified between the 5 mtorr film and the others. This result could be due to: (1) a higher value of electron carriers in the first deposited film; (2) the consequence of secondary phases; (3) a different structural film growth. The optical indexes difference of the purple line (200 mtorr deposition) for high energy band gap is mainly due to a non-optimal fitting of the measurement spectra with the model used, which is a direct consequence of the uncertain value of the thin film thickness and roughness.

The cationic composition of the thin films was then analysed by EDS. This is particularly important since stoichiometric films are expected to maintain the bulk electrical properties, while deviation from the correct stoichiometry may result in profound differences. Figure 4-28 resume the Ti/(La+Sr) ratio measured as a function of the deposition pressure. The red curve represents the target value (stoichiometry) while the blue curve the real trend measured. The results show that at list a 20% of titanium deficiency was detected in all the thin films deposited. Moreover, at intermediate pressures (60 mtorr) a further decrease of Ti content was measured.

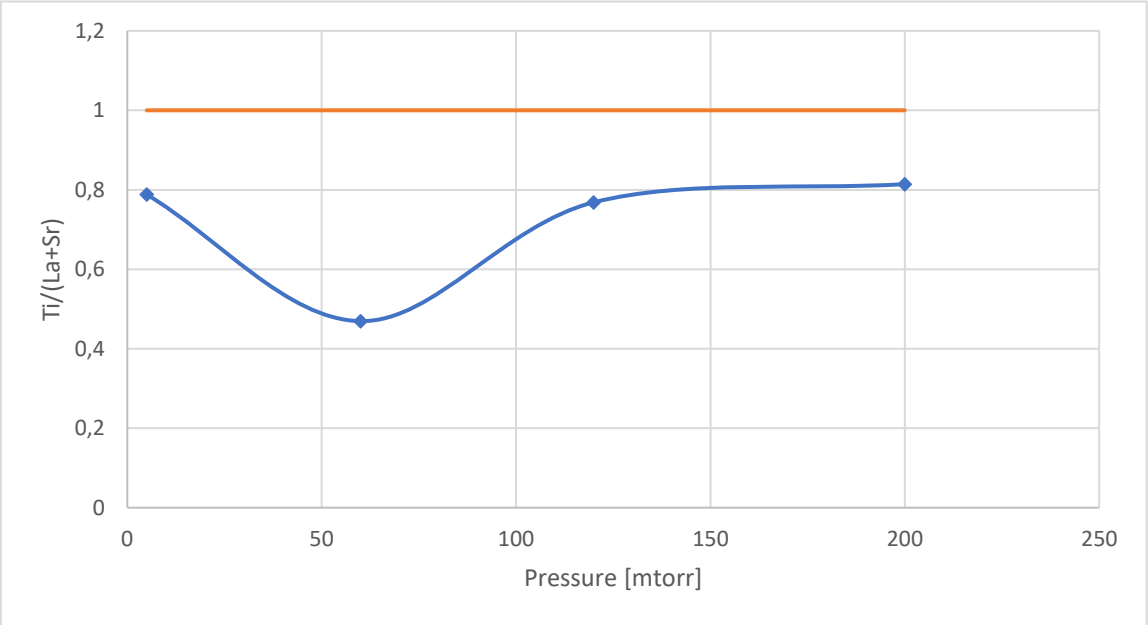

Figure 4-28. Variation of atomic stoichiometry with pressure deposition.

The decreasing atomic percentage of Ti with intermediate pressure is a direct consequence of the PLD plasma background interactions. With very low deposition pressure, the plasma plume, generated by the laser beam, is narrow and hence the stoichiometric proportion of the element should be directly transferred in the substrate chip. With the increase of background pressure, the plasma plume generated is wider and the lighter elements (*e.g.* Ti) are scattered towards higher angles than the lighter ones (*e.g.* La, Sr), giving rise to a variation of the atomic elements on the film. In such a case, the heavier elements are predominant, explaining the results obtained for p=60mtorr. As the pressure is increased enough (120 mtorr in this case) the plume diameter increases and all the elements are scattered at the same way, thus leading to the elements proportion similar to the initial one.

Anyway, since an important lack of titanium has been detected also in the high (200 mtorr) and low (5 mtorr) pressure films, further analyses were performed. Pellet stoichiometry and morphology has been tested with EDS and SEM, both in clean and ablated surfaces, as shown in figure 4-29.

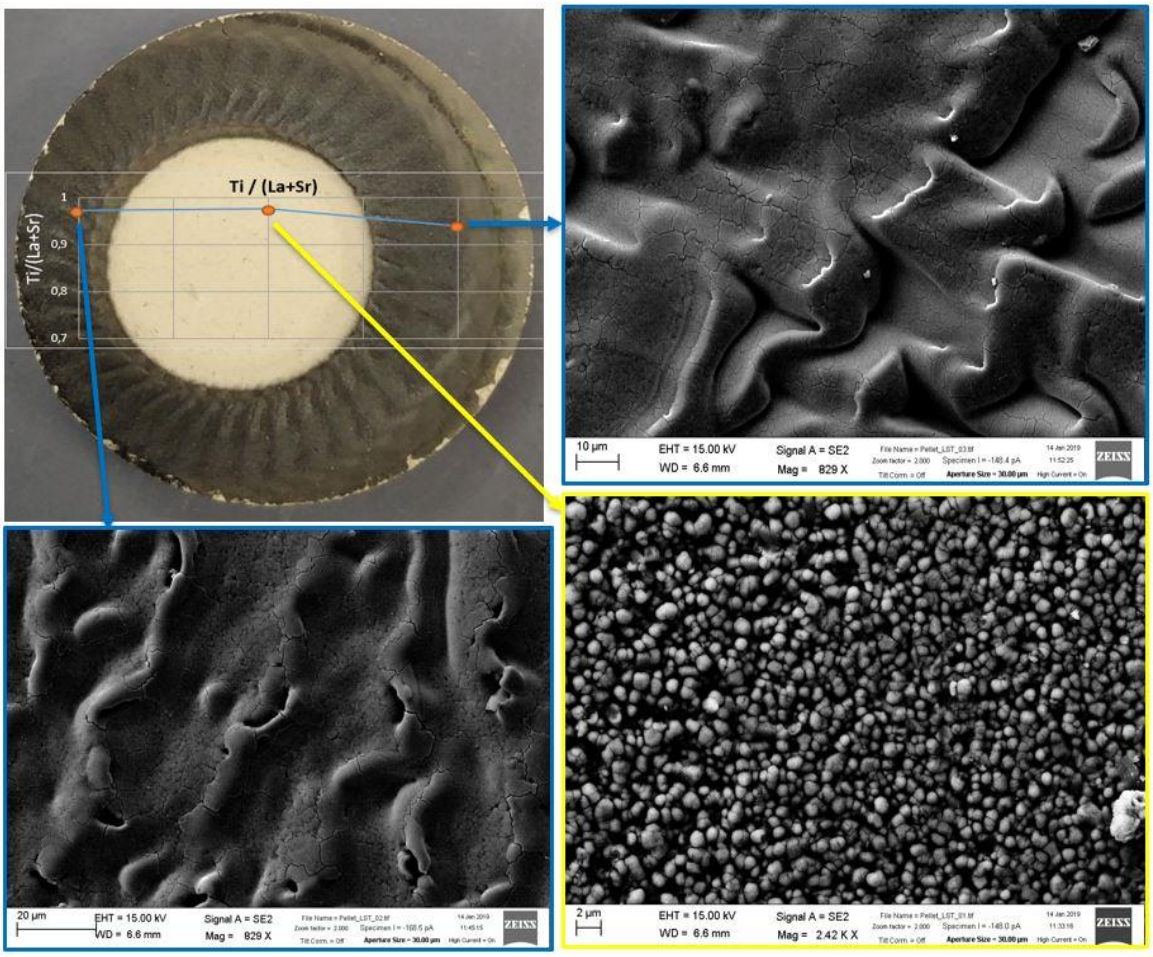

Figure 4-29. EDS and SEM analyses pellet, post PLD.

The lighter-heavier elements ratio, performed on the pellet in every significant point, did not show titanium lacks, with a minimum value of 94% in the ablated zone. Therefore, the titanium lost in the films was not caused by a non-stoichiometric pellet. It is suggested that the origin of the Ti deficiency detected for any deposition pressure is related with a non-stoichiometric ablation of the target, as shown in [74].

The different films were then analysed by XRD to verify their crystal structure and compare them with the polycrystalline pellet. Figure 4-30 shows the result obtained. In principle, every film showed a polycrystalline structure with two preferential orientations (l00 and the 110) of the cubic cell. The substrate (MgO) peak around 42,9° may cover the (111) peak of the films (except for the 200 mtorr deposition). Moreover, the XRD patterns do not show any secondary phases for all the deposition pressure apart from the 200mtorr thin films, which displayed a little anomalous peak near 40° as shown in figure 4-28. This minor secondary phase was been analysed with *X'Pert HighScore Plus* software. The possible matches found are listed in table 4-

15. Therefore, the XRD analysis shows that, despite the Ti deficiency, all the films correctly crystalized in the cubic perovskite phase.

Table 4-15. 200 mtorr probable secondary phases.

Chemical formula	Structure
La_2O_3	Monoclinic
TiO	Monoclinic

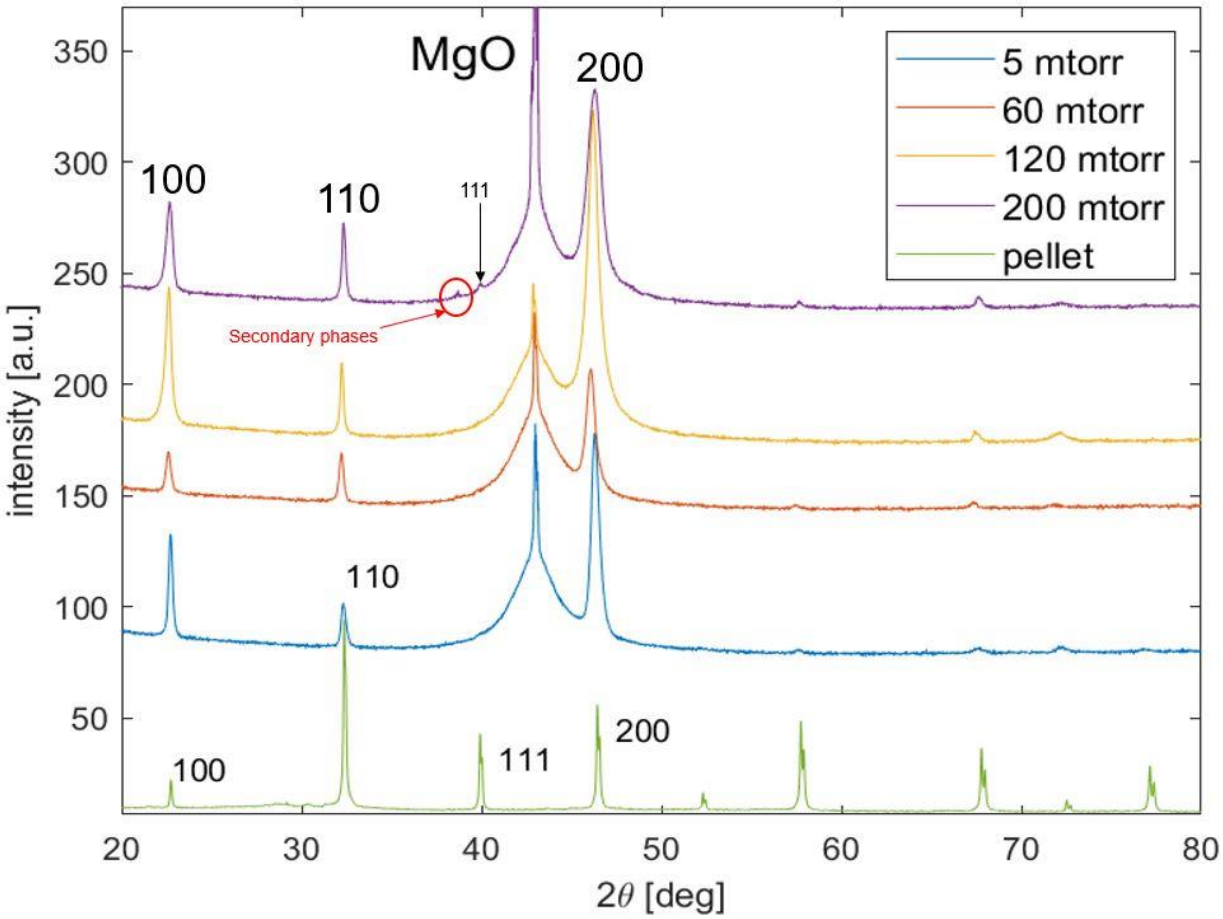

Figure 4-30. XRD results on thin films compared to the pellet XRD.

Apart from the phase analysis of the films, the XRD was also used to determine the lattice parameter variation between the films and the pellet (powder) one. Analysing the main peaks registered for each film and using the equation (3.1) in section 3-1 together with the equation (4-3), the lattice parameter (a) of every film has been calculated:

$$a = d_{hkl}\sqrt{h^2 + k^2 + l^2} \qquad (4.3)$$

The results, resumed in table 4-16, shows an increased lattice parameter, respect the pellet one, especially in the 60 mtorr deposition. This changing is also detected in the XRD, since the 60 mtorr peaks have a shift towards lower angles.

Table 4-16. Film lattice parameters.

Pellet lattice parameter [Å]			3,91
Film lattice parameter [Å]		***stan. dev.***	***Variation with Pellet (%)***
5 mTorr	3,92	$4{,}51 \cdot 10^{-3}$	0,21
60 mTorr	3,93	$4{,}20 \cdot 10^{-3}$	0,60
120 mTorr	3,92	$8{,}09 \cdot 10^{-6}$	0,43
200 mTorr	3,92	$2{,}45 \cdot 10^{-3}$	0,20

Interestingly, plotting the lattice parameters of the layer as a function of the Ti/(La+Sr) ratio an almost linear behaviour is observed, see figure 4-31. This behaviour is in agreement with the trend observed in other B-site deficient perovskite oxides [75, 76, 77].

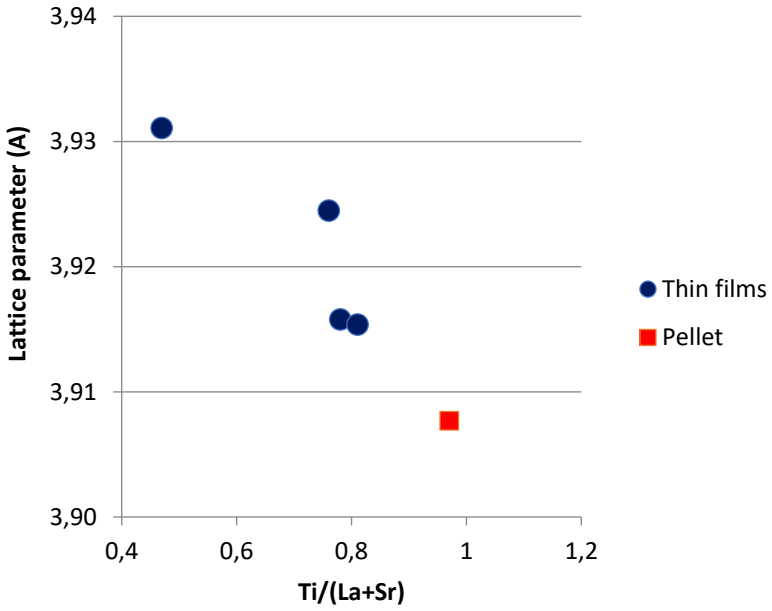

Figure 4-31. Lattice parameters obtained by XRD as a function of the Ti content in the structure.

The structure of the thin films was then analysed by top view SEM, see figure 4-32. All the films present a dense structure with no apparent cracks, as required for a correct analysis of the electrical properties. On the other hand, a huge structural evolution is visible in the layers increasing the deposition pressure, consisting in both an increase of the grain size and in the appearance of surface patterns. The films deposited at the lowest background pressure (5 mtorr) showed the most regular and dense structure, in agreement with ellipsometry measurements.

Atomic Force Microscopy (AFM) measurements were performed on 5/60/120 mtorr thin films to study their topography. Figure 4-33 shows the AFM topography of each film with the corresponding dimension scale on the left. The measurements were performed in a 2µm square. The low roughness of 5 mtorr film, already observed with ellipsometry and SEM, was confirmed. The average roughness (rq) values are shown in figure 4-33. A similar microstructure with respect to the SEM pictures has been detected.

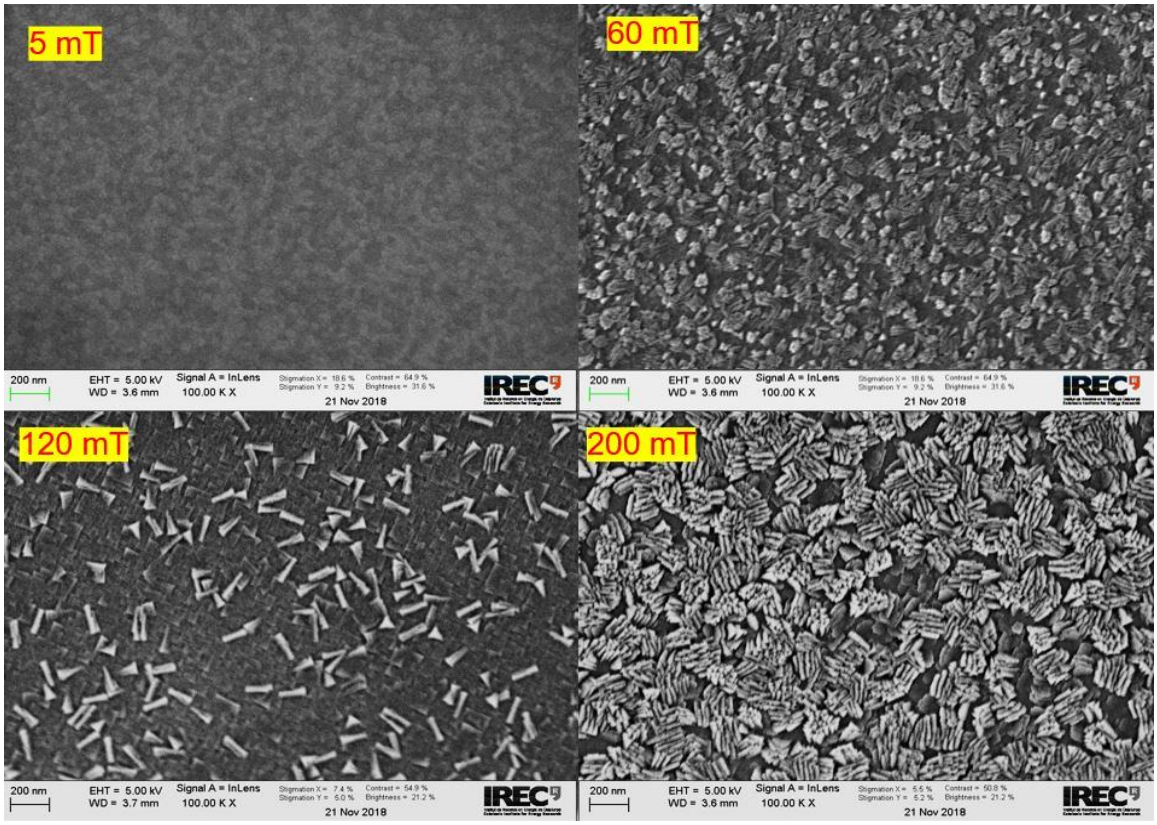

Figure 4-32. SEM images on films top view.

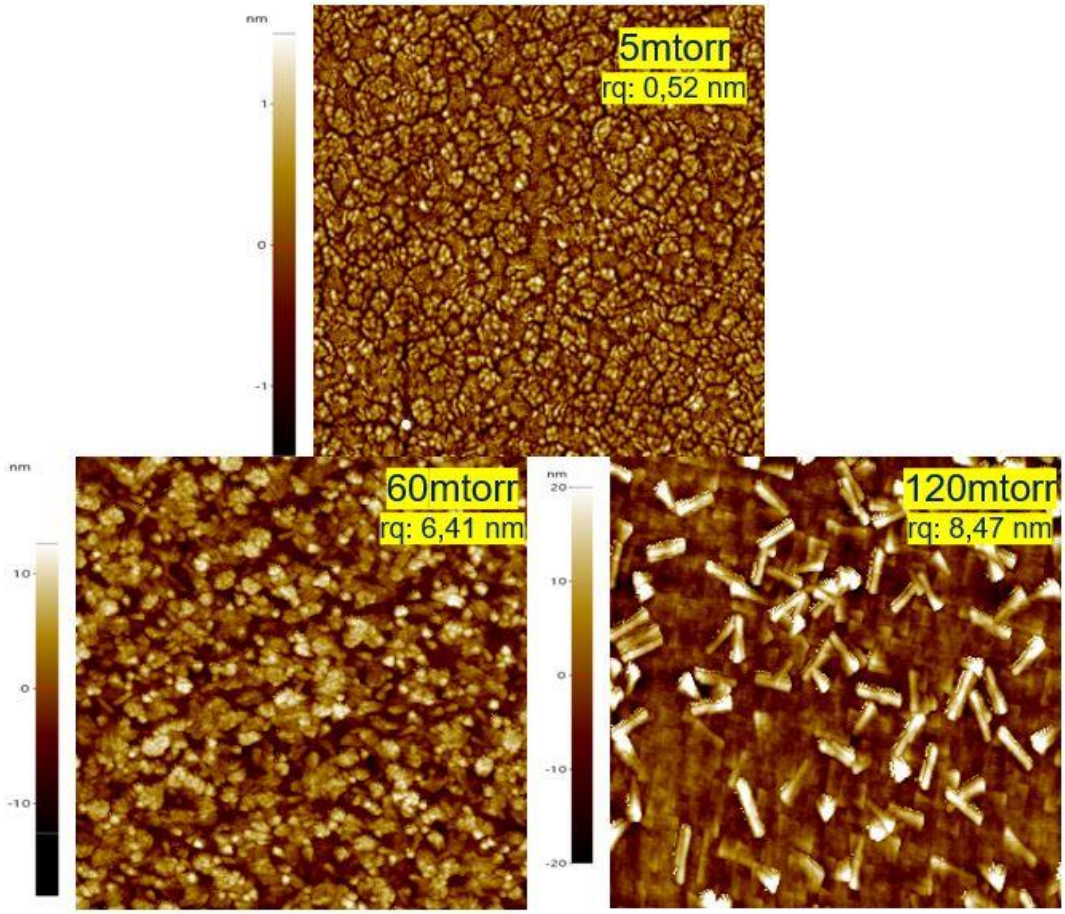

Figure 4-33. AFM measurements on 5/60/120 mtorr thin films.

Figure 4-34 shows the line topography trend of the films' roughness in 2 µm distance. The roughness of the 5 mtorr film varies only of 1,5 nm, while the other films have at list 20 nm of variation. Moreover, the higher the deposition pressure the more irregular the film.

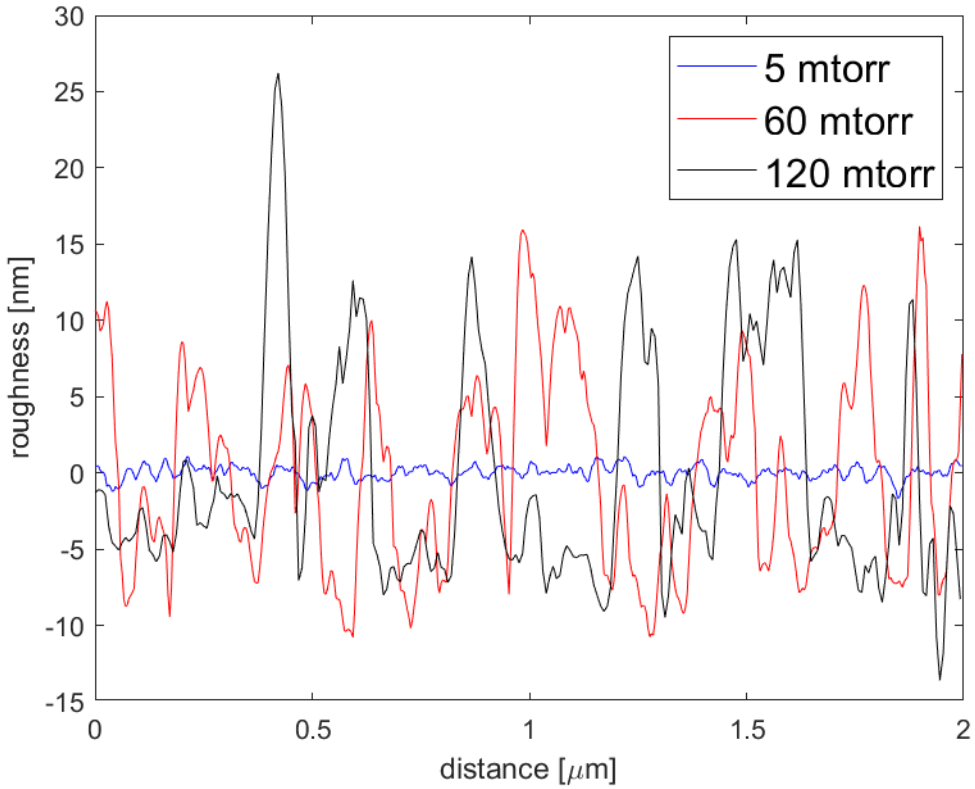

Figure 4-34. AFM line topography result.

In conclusion, LST37 thin films were correctly deposited. EDS analyses evidenced an important lack of titanium in each film which is not related to the pellet stoichiometry. The XRD patterns displayed a polycrystalline structure of all the films. A trend has been found between titanium lacks and the increase of lattice parameters (a). The SEM as well as AFM measurements detected a significant structural evolution of the films with pressure deposition and highlighted the low roughness of the 5mtorr film.

4.2.2 In-plane electrical properties

Electrical conductivity measurements were performed with a temperature-controlled Linkam probe station. A first calibration of the point contacts was done before the tests, to verify a linear behaviour between of the I-V curve, thus meaning a correct resistance measurement. Four gold points sputtered at the corner of the samples guaranteed the electrical connections with the probes. Once the contacts were verified, every measurement followed this route:

- Temperature increasing from RT to 550°C in oxidant (O_2 flow) atmosphere;
- At high temperature, once the resistance was stabilized, the atmosphere was changed from totally oxidant to inert (N_2 flow), with the intermediate steps in air (21% O_2 – 79% N_2) and then decreasing the oxygen partial pressure (1000 ppm – 100 ppm);

- Keeping constant the temperature (550°C), the atmosphere was changed again from nitrogen to a reducing atmosphere with 5% of H_2 dispersed in Argon;
- Finally, the behaviour of the films in reducing atmosphere with the decreasing of temperature from 550°C to RT was analysed.

All the films showed similar conductivity behaviour with temperature in oxidizing atmosphere, represented in figure 4-35. In agreement with literature references [57], the conductivity reached a maximum around 400°C, after which the layers start to oxidize, and the conductivity progressively decreases.

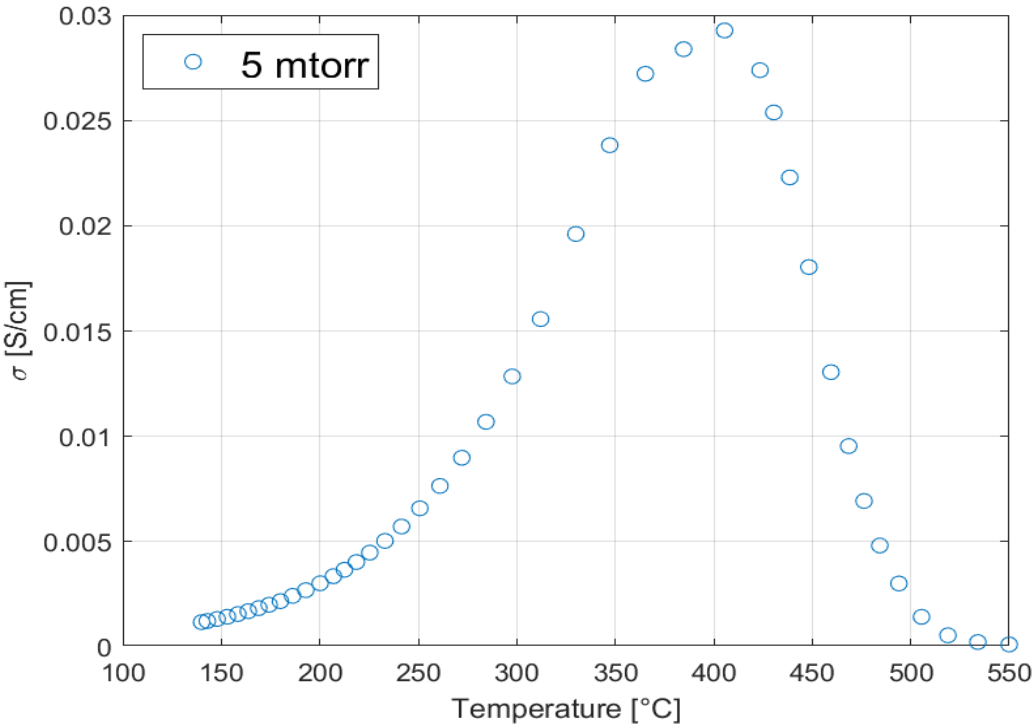

Figure 4-35. Conductivity trend with temperature in oxidizing atmosphere.

All the films showed a substantial modification of the electrical properties in hydrogen; indeed, an increasing conductivity has been measured for each film with the variation of atmosphere from oxidant to reducing one. Figure 4-36 shows the conductivity dependence on oxygen partial pressure variation. The inclination showed in figure 4-36 (-0,35) is related to the *reduction type semi-conduction behaviour* also called *n-type semi-conduction behaviour*. This phenomenon is related to a progressive decrease of oxygen content in the lattice, which generates an increase of electrons in the system for charge compensation. This rise of the electronic charge carriers give rise to an increase of the in-plane conductivity in n-type materials, as measured in the LST thin films.

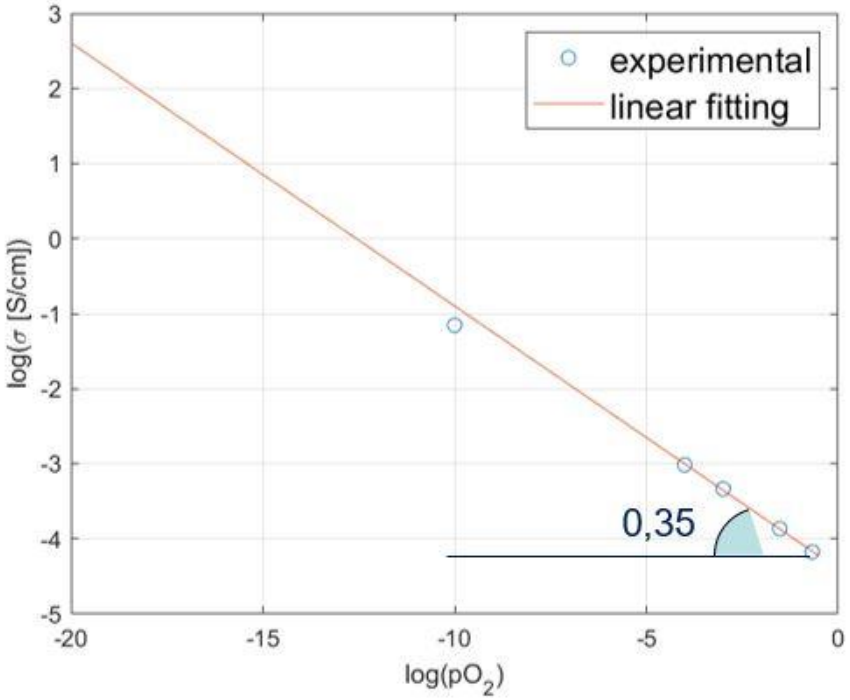

Figure 4-36. N-type semi-conduction behaviour on 5 mtorr deposition.

To calculate the activation energy of the thin films, the Arrhenius formula must be considered:

$$\sigma = \sigma_0 \cdot e^{\left(\frac{-E_a}{k_b T}\right)} \qquad (4.4)$$

Where k_b is the Boltzmann constant ($8{,}61733 \cdot 10^{-5}$ evK^{-1}), T is the temperature, σ_0 is the pre-exponential factor and E_a is the activation energy. However, a better fitting and hence E_a calculation was found by using the *polaron hopping adiabatic* model, which consider that electronic charge carriers are localize around the Ti atoms by strong electron-lattice phenomena, giving rise to a semiconducting behaviour with the temperature. The Arrhenius formula is changed as follow:

$$\sigma = \frac{\sigma_0}{T} \cdot e^{\left(\frac{-E_a}{k_b T}\right)} \qquad (4.5)$$

Therefore, applying the natural logarithm to the equation (4.6), the constant σ_0 and the E_a can be obtained:

$$\ln(\sigma T) = A - k * \frac{1000}{T} \qquad (4.6)$$

Where the A and k constant are:

$$A = ln(\sigma_0) \rightarrow \sigma_0 = e^A \qquad (4.7)$$

$$k = \frac{E_a}{k_b} \rightarrow E_a = k_b * k \qquad (4.8)$$

In this way, by plotting the ln(σT) as a function of 1000/T, the activation energy is calculated from the angular coefficient of the linear interpolation and σ_0, which represents the conductivity (liberty of carriers' motion) with "infinite" temperature.
Figure 4-37 shows the results obtained with three different films. Increasing the deposition pressure from 5 mtorr to 120 and 200 mtorr a substantial rise of conductivity is observed, especially at low temperature. Nevertheless, it must be noticed that the thin film deposited at 60 mtorr did not show any electronic conductivity even at high temperature (the resistance was always above the detection limit). This is probably related to the huge lack of titanium measured in this film (Ti/(La+Sr) ~0.5). Indeed, since the electronic charge carrier are mostly located on the Ti sites (polaron behaviour), the lack of Ti strongly hinder the electronic conduction, giving rise to a highly insulating behaviour. Also, it is possible that the presence of negatively charged Ti vacancies in these films (V_{Ti}''') reduces the concentration of negative electrons generated for charge compensation by the La doping (and by the H_2 reduction), again hindering the electronic conduction.

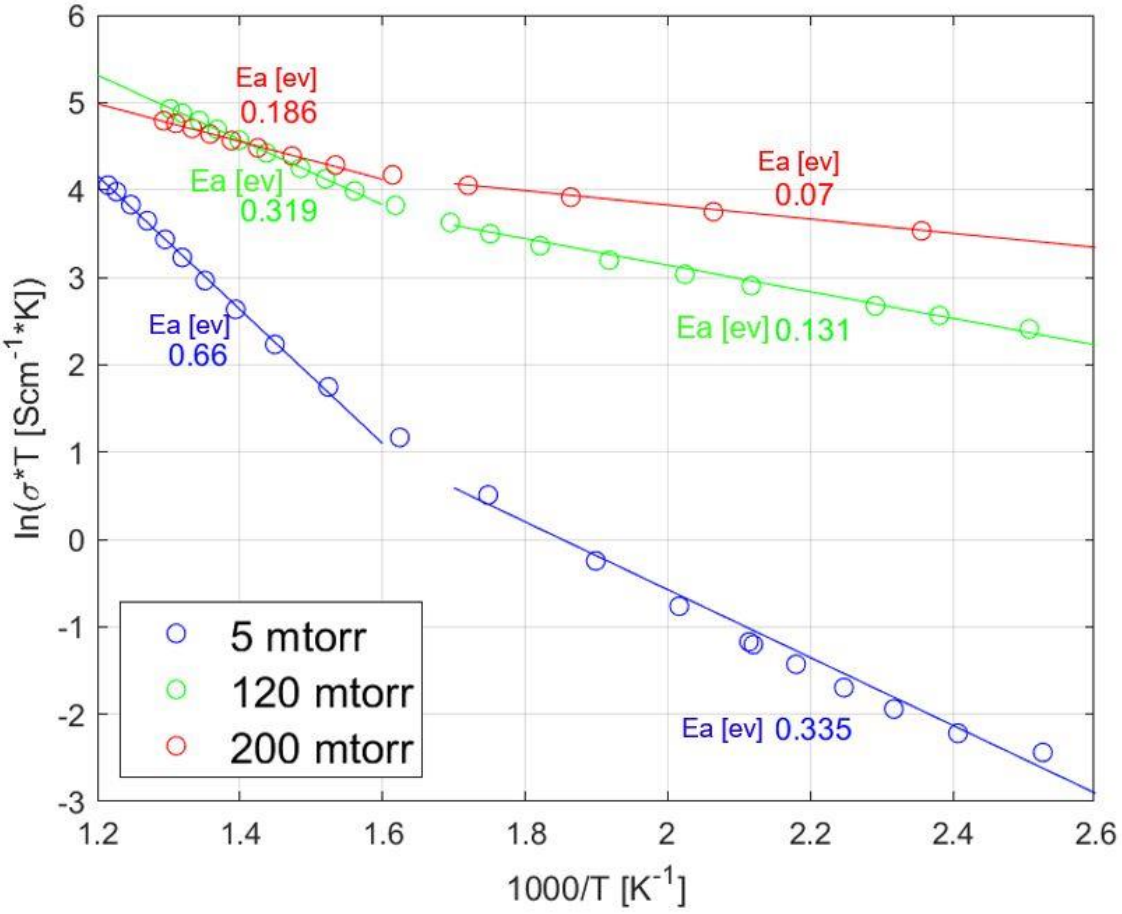

Figure 4-37. Evolution of in-plane conductivity of three films measured with Van der Pauw method.

Each measured film showed a variation of the slope at intermediate temperature, i.e. the activation energy changes between low temperature range (100 – 350°C) to high temperature range (350 – 550 °C). Therefore, a higher activation energy is required for higher temperature, while at low temperature low activation energies were detected, comparable to bulk LST anodes in literature [54], as shown in figure 4-38.

Nevertheless, a large decrease of conductivity is observed in comparison with the reference bulk, regardless of the deposition pressure of the thin films.

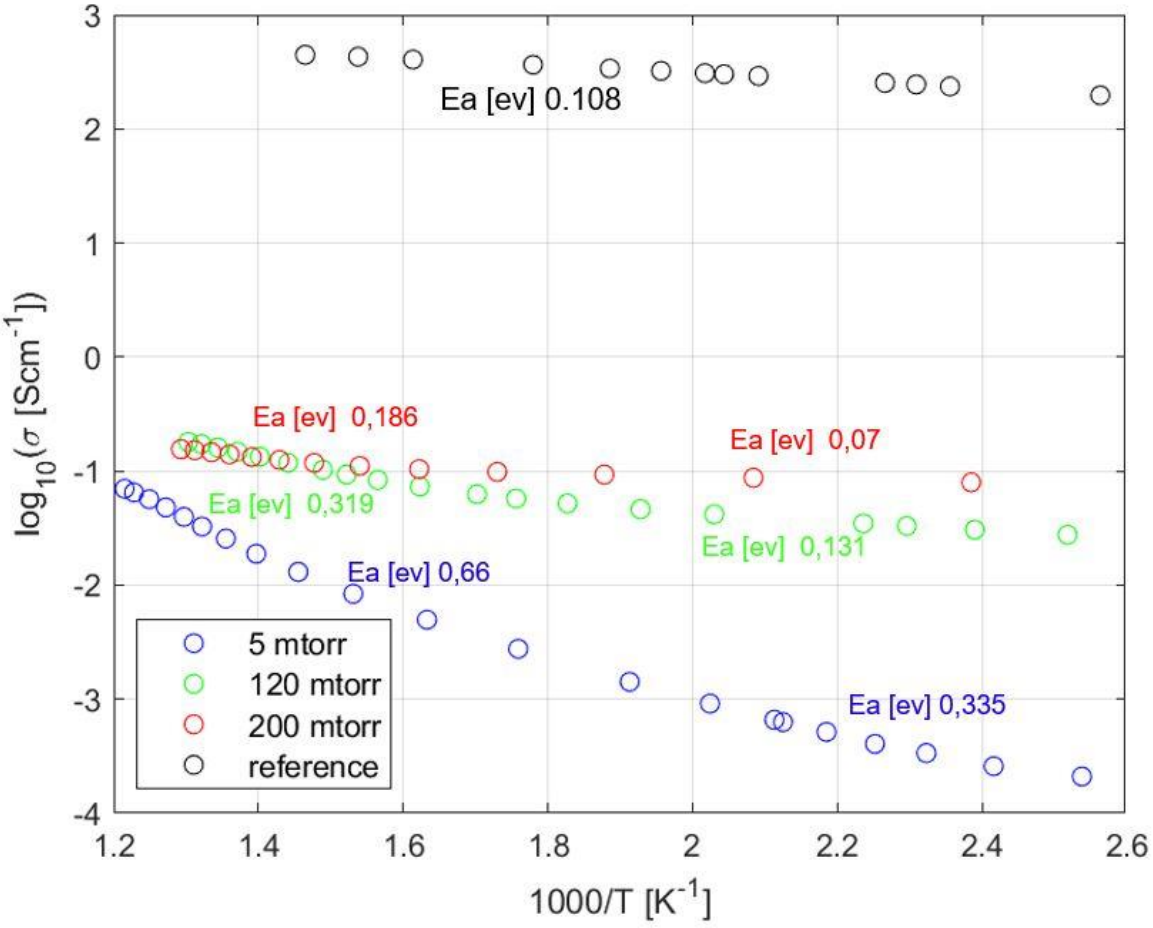

Figure 4-38. Evolution of in-plane conductivity of three films compared to a reference [54] value.

The low electrical conductivity measured on the LST thin film can be associated to:

- The lack of titanium atoms with respect to the stoichiometric material, as measured with EDS (Ti/(La+Sr) ~0.8) which, as discussed above, severely hinder the electronic conduction;
- Grain boundary effects, i.e. some paths of electrons could have a difficult motion;
- Trapping phenomena: some sites could present this effect, which increases the necessary electron energy to move throughout the lattice.

The overall decrease of conductivity respect to the bulk values probably originates from the Ti deficiency observed in the thin films. However, this mechanism cannot explain the differences measured among the 5, 120 and 200 mtorr samples, since similar B/A ratio were detected in these layers. The substantial grain evolution observed in the previous section suggests that the thin film's structure influences the electronic motion. Indeed the 120 and 200 mtorr deposition showed larger grains (it is evident in SEM pictures and the morphologies obtained with AFM) with respect to the 5 mtorr one. Small grain sizes should have higher probability of localized electronic defects presence, such as oxygen vacancies, during the conduction path. Therefore,

the electrons moving in the grain boundary of a large grain size structure should incur into a low number of defects.

Figure 4-39 shows the influence of pressure deposition on film grain size and on the conductivity. The grain sizes of the films were calculated through *XEI* software, analysing the AFM topography results obtained. To increase the background pressure on PLD has a structural consequence as previously described and the larger grain sizes obtained confer higher electrical properties.

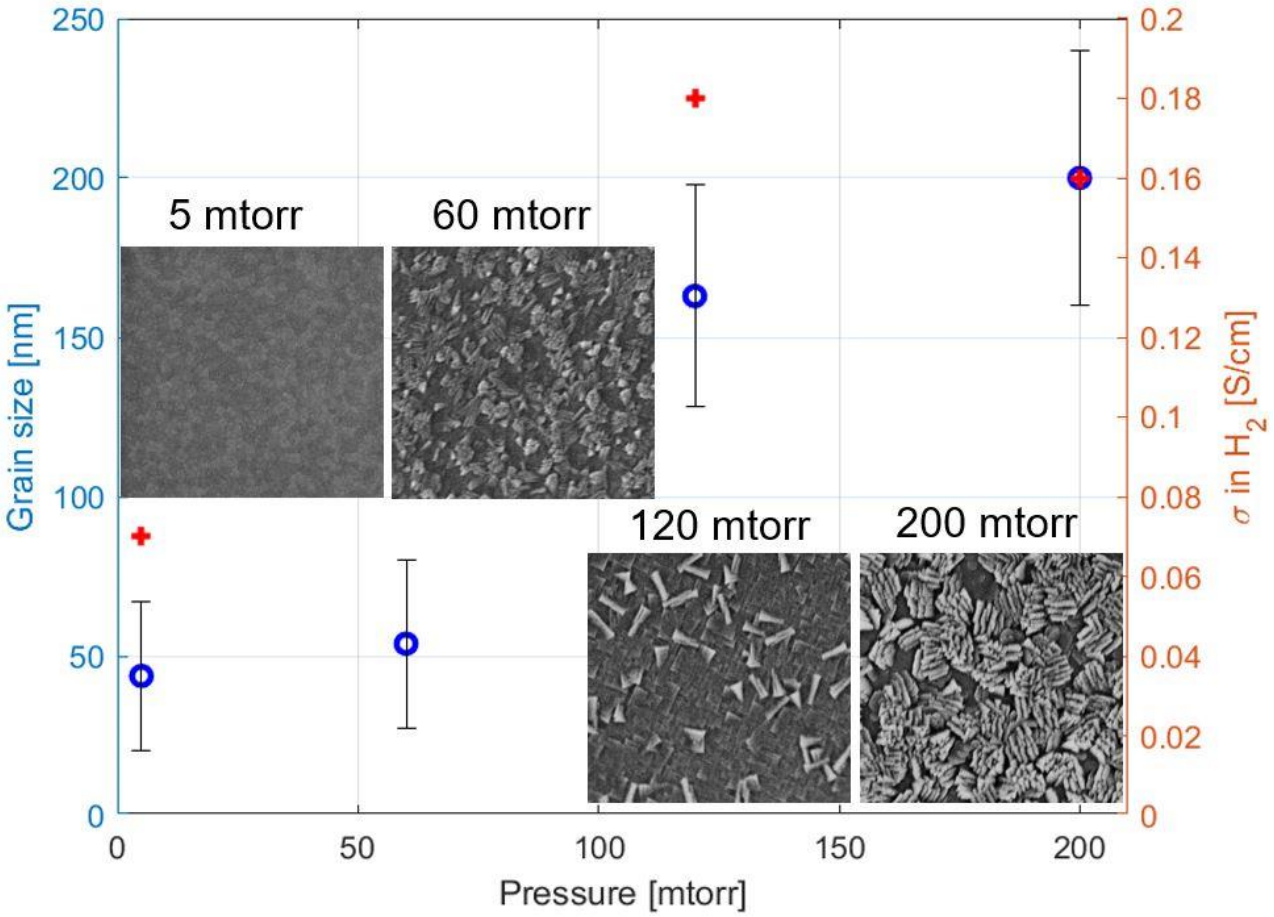

Figure 4-39. Deposition pressure influence on film grain size and conductivity at 500°C.

Moreover, the grain size effect on the activation energy is shown in figure 4-40. The layout has been studied both for the high temperature range (350 – 550°C) and for the low temperature range (100 – 350°C). Both cases highlighted the decreasing activation energy with the increasing grain size. This linear behaviour with the grain dimensions strongly suggests that the grain boundaries are at the origin of the differences in conductivity measured in the different thin films.

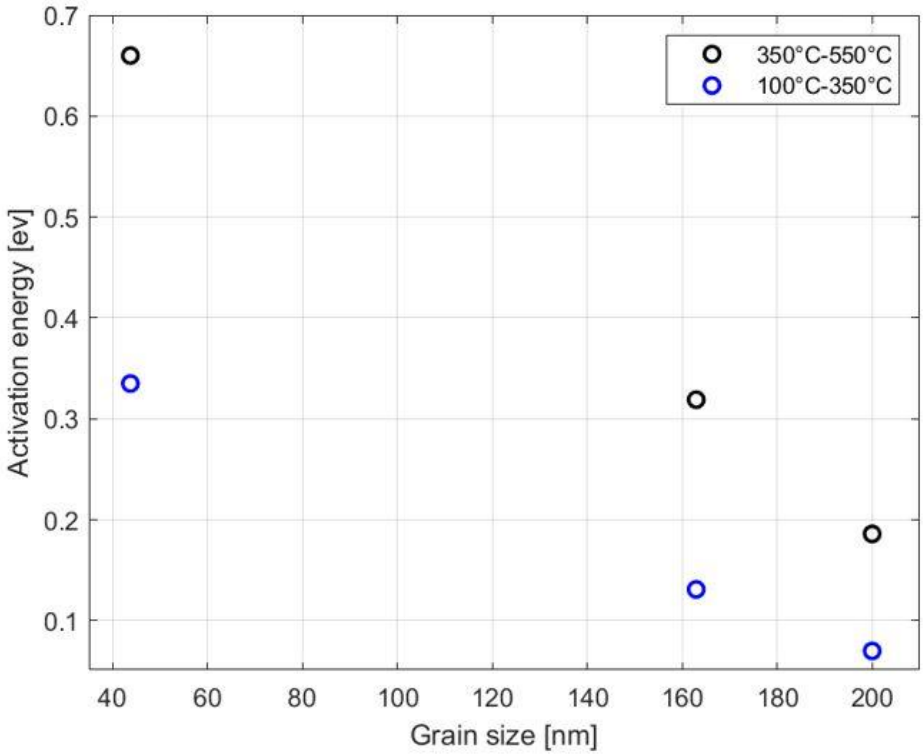

Figure 4-40. Activation energy trend with grain size.

Finally, it is important to note that, although a smaller conductivity was observed in the thin films respect to the bulk, the results still signify a large improvement respect to the state of art anode for μSOFC. Indeed, previous in-plane conductivity measurements performed on 250 nm-thick porous CGO anode deposited on dense YSZ on Si3N4/SiO2/Si substrate [15] showed 0,02 S/cm of conductivity at 550°C. Here, the maximum value achieved with the 120 mtorr deposition at 500°C is near 0,2 S/cm, which is one order of magnitude higher. Moreover, increasing the temperature up to 600 – 650°C (typical operating temperature of our micro device), the conductivity of the 5 mtorr deposition could reach even higher values since its activation energy is higher than the other ones.

4.2.3 Out-of-plane electrochemical properties

The electrochemical properties of LST thin films were then investigated by electrochemical impedance spectroscopy (EIS). The measurements were performed in an out-of-plane configuration, depositing two symmetrical LST thin films on both surfaces of single crystal YSZ chip. Two deposition pressures were selected (5 mtorr and 200 mtorr) to analyse the electrochemical properties with the whole range of pressure.

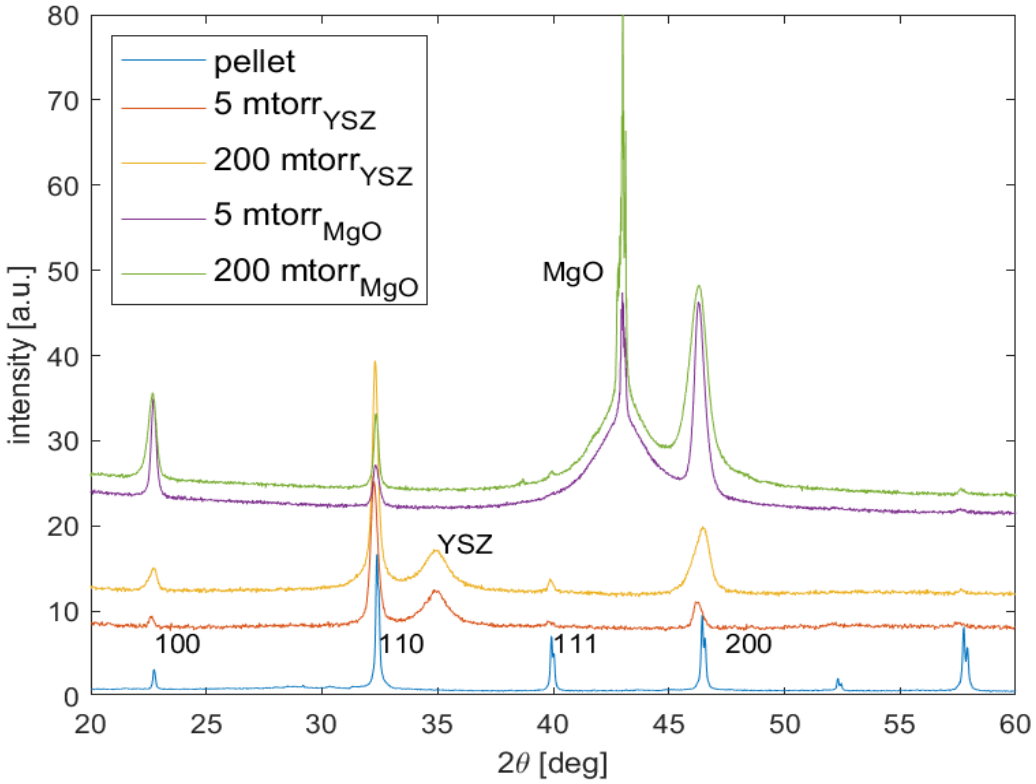

Figure 4-41. XRD results on LST thin film depositions on single crystal YSZ chip.

Figure 4-41 shows the XRD spectra of thin films deposited on sc-YSZ. Clearly, the substrate peak changes from MgO to YSZ. Moreover, a higher intensity of (110) orientation has been noticed, with a corresponding decreasing of (100) and (200) peak intensities. No secondary phases were noticed.

The sample has been covered in both sides with a porous gold paste and two gold nets in order to effectively measure the entire thin film surface and enhance the electron percolation [69, 70], as shown in figure 3-13, section 3-2. Carefully inserting the sample in the ProboStat station, avoiding gold wires contacts (causing short-circuit), the measurements were performed varying temperature and atmosphere. Both synthetic air and humidified hydrogen (5 % in Argon) were used. The temperature was varied every 25°C between 700°C to 600°C.

The 200 mtorr film did not show significant results, since its spectrum showed huge values of impedance. The 5 mtorr film measurement results are shown in the Nyquist plot in figure 4-42. High values of impedance were detected at 700°C. Mainly three phenomena were observed at $7{,}5 \cdot 10^4$ – 5 – 0,2 Hz. An equivalent circuit with a series of constant phase elements (CPE) in parallel with resistances have been adopted, as shown in figure 4-42. The series resistance is associated to the electrolyte (YSZ) resistance, which ASR value is represented by the real axis offset in the Nyquist plot (see the magnification of figure 4-42).

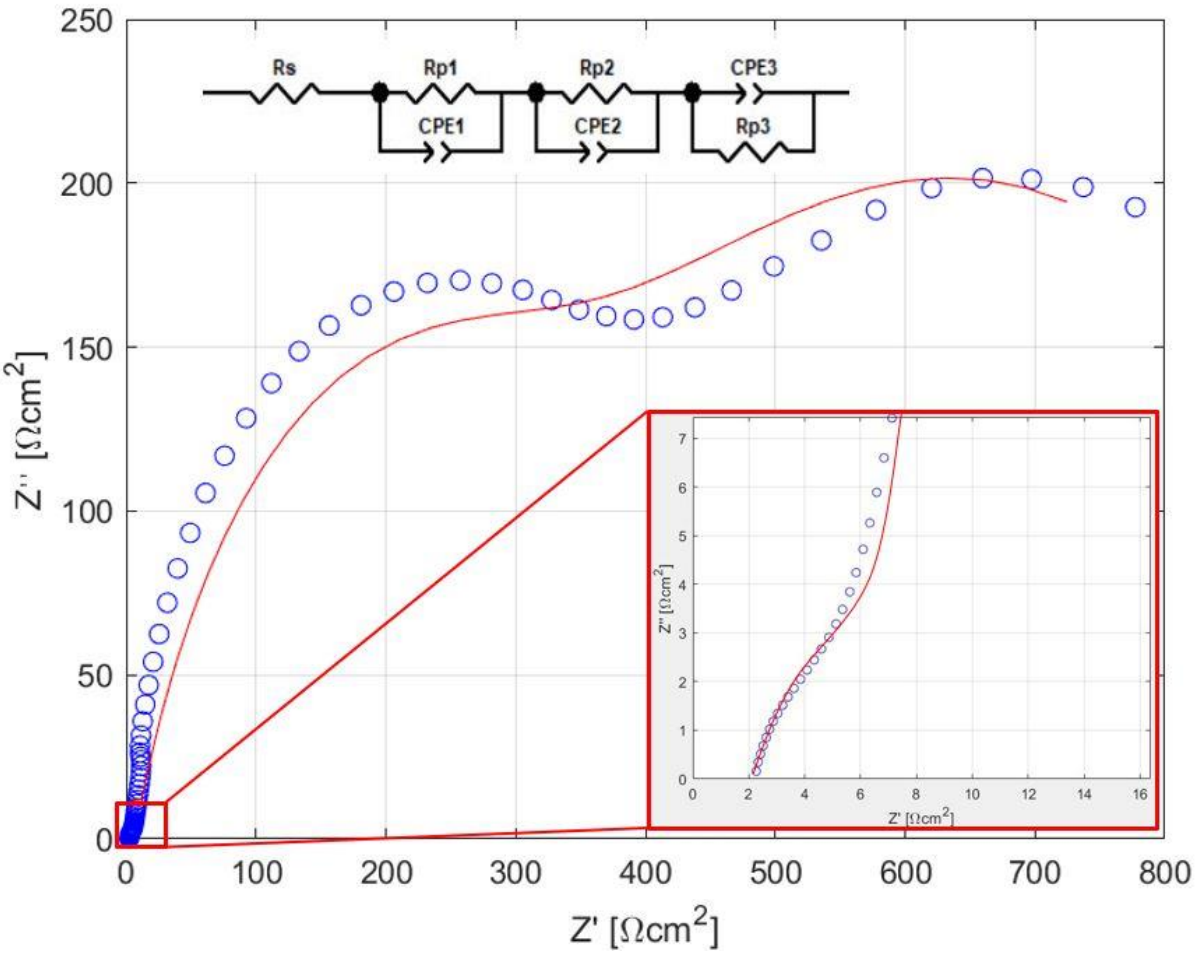

Figure 4-42. Nyquist plot of 5 mtorr deposition at 5% H_2 in Ar atmosphere at 700°C.

To obtain a good fitting was rather complicated, since the electrochemical process measured is complex. A difficult interpretation could be given on the three different phenomena. Considering the CPE obtained from the fitting, interphase sample-electrode (10^{-5} F/cm) and electrochemical reactions processes (10^{-4} F/cm) are the most probable phenomena present.

With the results on CPE and resistances obtained with the fit curve, the evolution of the ASR with temperature in reducing atmosphere has been obtained, shown in figure 4-43. The total reactive area considered was a square film of 0,8 cm edge (the chip used is 1 cm). Therefore, the contribution of impedance measured was multiplied by 0,64 cm^2 and divided by two, since the EIS measures the resistance in both sides. To reach the target value of ASR of 0,30 Ωcm^2, temperatures above 800°C are necessary. A higher activation energy (1,6 ev) with respect to the previous work of G. Iñigo et al. [15] was obtained, confirming the high impedances measured in the Nyquist plot. Despite the difference of ASR obtained with respect to [15], it is worth to mention that G. Iñigo et al. used a cermet CGO-Pt anode, which increase extremely the electrochemical performance of a fully ceramic anode. However, further enhancements are necessary to make LST a competitive thin film for micro-SOFC.

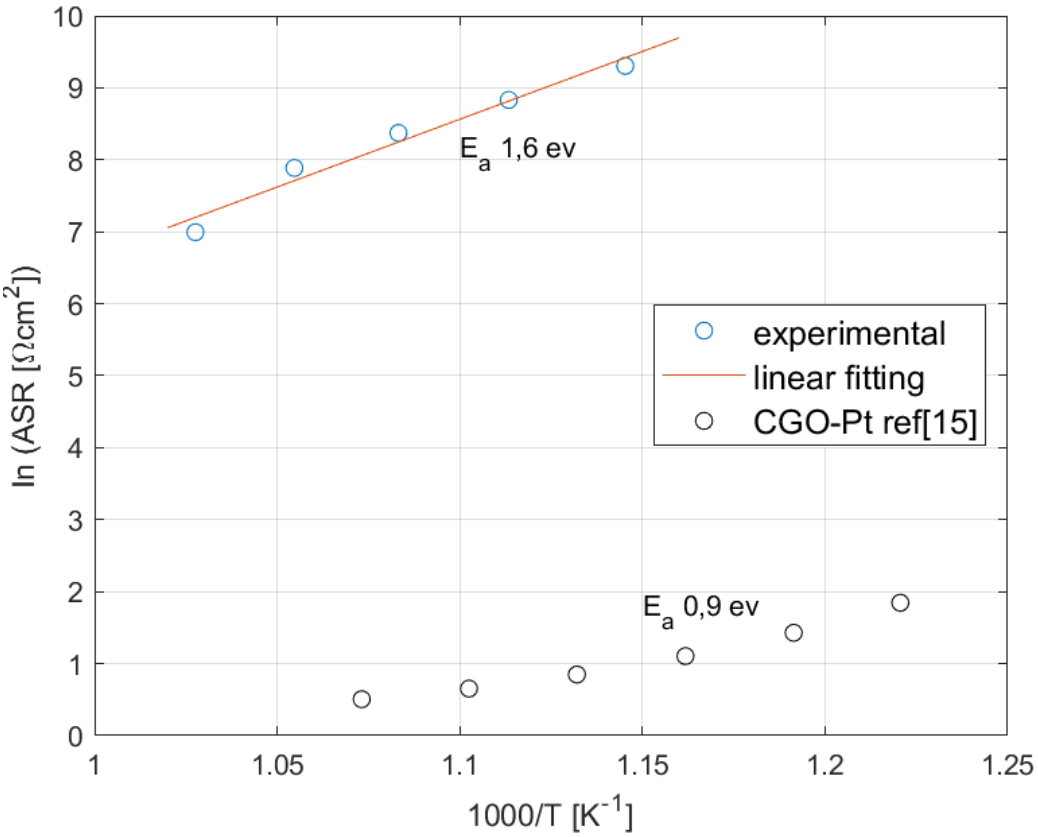

Figure 4-43. Evolution of ASR of symmetrical LST/YSZ/LST cell with temperature.

4.2.4 Discussion and further works

Different LST thin films were obtained with pressure deposition variation. Dense films were expected in order to measure the real electrical and electrochemical behaviour of the material. With low pressure (5 mtorr) deposition, super dense thin film has been obtained with a very reduced roughness. A grain size dependence on pressure deposition has been noticed, i.e. large grain size (200 nm) were measured with 200 mtorr pressure deposition while 40 nm grain size was detected in 5 mtorr film. The poly-crystalline films obtained had two preferential orientations, determined by XRD and significant no secondary phases were detected. EDS analyses determined an important lack of titanium in each film thus leading to low electrical and electrochemical properties.
An interesting grain size effect on activation energy and conductivity of the films has been highlighted with the in-plane conductivity measurements. Relative low activation energy has been measured with high pressure depositions (and large grain sizes) giving the dependence of electrical properties with grain boundary of the films. Therefore, the smaller the grain size the higher probability to encounter defects which could block the electrons migration.

Further works are mandatory to enhance the functional properties of LST thin films; therefore, promising technique could be adopted:

- Exsolution of metal nanoparticles should increase the in-plane conductivity of the films and the electrochemical properties. For instance, C. Arrivé et al. [73] demonstrated that Ni nanoparticle exsolution at the surface of a conductive titanate could enhance the electrical conductivity, probably due to the formation of a sufficiently high concentration of Ti^{3+}. They obtained 0,55 Ωcm^2 at 800°C in an anode for bulk SOFC. For thin film applications, this technique could be adopted by doping the target with Ni nanoparticles.
- Deposition of platinum on top of the films, obtaining cermet materials and hence improving the electronic conductivity as already demonstrated by I. Garbayo [15, 17].
- Combinatorial pulsed laser deposition (C-PLD) by using different target materials, some of them with higher amount of titanium. Indeed, an initial target with a A-site deficiency (decreasing the amount of strontium, which could form strontium oxides and blocking the electronic paths) could be prosperous for the electric properties, as already demonstrated in bulk SOFC [13, 52, 55, 57].
- Porous thin film depositions could largely increase the electrochemical performance, because it would enlarge the active contact area with H_2.

In conclusion, the first complete thin film characterization of $Sr_{0,7}La_{0,3}TiO_3$ ceramic anode for micro-SOFC has been proposed. Future works on LST37, enhancing the electrochemical properties, could develop a highly stable and fully compatible ceramic anode with other SOFC components.

CONCLUSIONS AND FURTHER PERSPECTIVES

The main goals of the current study were to develop a novel ceramic thin film anode for micro-SOFCs and to optimize the joining encapsulation process with a glass-based sealant. The obtained results (either at IREC and at POLITO) have shown an improved reliability of the *Ultra-SOFC* system, opening new strategies on the fabrication and encapsulation of micro-SOFCs.
The main results on the glass-based sealant joining and the innovative thin full-ceramic anode are listed and detailed below:

- **Glass sealant joining**

A glass-based sealant (G018-197 commercial powder from SCHOTT AG) has been optimized in terms of characteristic properties (thermal expansion coefficient (CTE), viscosity, shrinkage behaviour, wettability) and deposition technique. The results have been carried out by comparing two different thermal treatments (650°C and 700°C as max T) used for the joining of silicon chips (encapsulation).
The joining related to the glass sealant heat treated at 700°C has been demonstrated the optimal procedure for the final device encapsulation. Indeed, unlike the other treatment, it has highlighted several advantages:

- ✓ From dilatometry measurement, a CTE close to the silicon one has been found, due to the crystalline phases detected from EDS, SEM and XRD analyses (zinc borates, zinc silicates, zinc oxides). The measured sealant CTE in the device operating temperature (100°C – 600°C) is 4,716E-06 K^{-1};
- ✓ As demonstrated by HSM measurements, the shrinkage behaviour allows a higher volume reduction (more than 15%) than the sealant heat treated at 650°C, and an overall shrinkage of 40% with respect to the as-deposited paste;
- ✓ The sealant guarantees good adhesion and wettability with silicon, showed by SEM images and the work adhesion measurements performed with sessile drop tests;
- ✓ The glass-ceramic behaviour of the sealant with a proper amount of residual glassy phase (softening temperature around 580°C), allows to heal possible cracks formed during thermal cycles and guarantees a reduced porosity.
- ✓ Its thickness and controllable line deposition can be managed and be reproduced, thanks to the micro etched steps on silicon chips and the development of a suitable liquid deposition modelling (LDM) technique.

A further study could assess the sealant behaviour by changing the glass particle dimensions, which would modify the crystallization process.
Further research should be undertaken to investigate the gas tightness of the joined area, i.e. by hermeticity measurements. Despite SEM images revealed a quite uniform volume without porosities, tests in relevant conditions are necessary.

- **Innovative thin film anode material**

Micro-SOFC devices are based on thin membranes (cathode/electrolyte/anode) integrated on silicon substrate. The production of dense thin films is fundamental to characterize the electrical and electrochemical properties of thin film materials.

Four different $Sr_{0,7}La_{0,3}TiO_3$ (LST) thin films were deposited with PLD on MgO substrate by varying the background pressure deposition (5/60/120/200 mtorr). Dense films were expected in order to measure the real electrical and electrochemical behaviour of the material.
A very dense and low roughness (2 nm) thin film (130 nm thick) was obtained with low pressure (5 mtorr) deposition. A grain size dependence on pressure deposition was found, i.e. large grain size (200 nm) were measured with 200 mtorr pressure deposition while 40 nm grain size was detected in 5 mtorr film, with the AFM analysis.

The poly-crystalline films obtained had two preferential orientations, determined by XRD and no secondary phases were detected. EDS analyses determined an important lack of titanium in each film thus leading to low electrical and electrochemical properties. The amount of Ti deficiency on thin films has been correlated to their lattice parameter, showing a decreasing of the lighter element with the increasing of the cubic cell dimension.

In-plane electric conductivity tests have highlighted an important difference with the anodes of bulk SOFCs, especially in terms of maximum conductivity (0,2 S/cm) reached at 500°C. Despite that, a very low activation energy was measured (down to 0,07 ev for the 200 mtorr thin film) demonstrating the LST as a promising material for thin film anodes.
Moreover, an interesting grain size effect on activation energy and conductivity of the films has been highlighted with the in-plane conductivity measurements. Relative low activation energy has been measured with high pressure depositions (and large grain sizes) giving the dependence of electrical properties with the grain boundary. This study has shown that, the smaller the grain size the higher probability to encounter defects (such as oxygen vacancies) which could block the electrons migration.

Out-of-plane electrochemical performances has been performed on LST/YSZ/LST symmetrical cells, showing high ionic impedances and an activation energy of 1,6 ev. Interphase sample-electrode and electrochemical reactions processes seem to be the main phenomena causing high values of impedance in the Nyquist plot.

Further works should focus on enhancing the functional properties of LST thin films. For instance, exsolution of metal nanoparticles should increase the in-plane conductivity of the films and the electrochemical properties. This technique could be adopted by doping the target with Ni nanoparticles. Moreover, combinatorial pulsed laser deposition (C-PLD) by using different target materials, could enhance the amount of Ti at the expense of Sr in thin films. Furthermore, deposition of platinum on top of the films, obtaining a more electronic conductive cermet material, as well as porous thin film depositions could largely increase the electrochemical performances.

In conclusion, the joining thermal treatment of a glass-based sealant for micro-SOFC has been optimized, obtaining the required properties for the integration of MEMS technology. Furthermore, the first complete thin film characterization of $Sr_{0,7}La_{0,3}TiO_3$ ceramic anode for micro-SOFC has been proposed, showing a grain boundary effects on thin film electrical properties.

This thesis has provided a deeper insight into advanced ceramics materials for energy conversion, opening new strategies for the development of a full-ceramic stable micro-SOFC device.

References

[1] *Introduction to PEMFC*, M. Santarelli, Energy department, Politecnico di Torino, *Polygeneration and advanced energy systems* course of study, 2014.

[2] *Progress in material selection for solid oxide fuel cell technology: A review,* Neelima Mahato et al., Progress in Material Science, 2015.

[3] *Hydrogen technologies and fuel cells. Notes on electrochemistry*, Massimo Santarelli, Energy department, Politecnico di Torino, *Polygeneration and advanced energy systems* course of study, 2014.

[4] *Fuel Cell Materials and Components,* S.M. Haile, Acta Materialia, Vol. 51, 5981–6000, 2003.

[5] *A thermally self-sustaining solid oxide fuel cell system at ultra-low operating temperature (319 °C),* Ikwhang Chang et al., Energy, 2016.

[6] *Celle a combustibile a ossidi solidi (SOFC). Descrizione generale della cella e dei suoi principi di funzionamento,* M. Santarelli, Energy department, Politecnico di Torino, *Polygeneration and advanced energy systems* course of study, 2014.

[7] *Redox study of anode-supported solid oxide fuel cell,* Faes A, Nakajo A et al., Journal of Power Sources, 2009.

[8] *Notes on the State-of-the-Art of SOFC,* M. Santarelli, Energy department, Politecnico di Torino (Italy), *Polygeneration and advanced energy systems* course of study, 2014.

[9] *Solid oxide cells materials part II*, F. Smeacetto, Energy department, Politecnico di Torino (Italy), *Advanced Materials for Energy* course of study, 2014.

[10] *3-D Nanostructured Bilayer Solid Oxide Fuel Cell with 1.3 W/cm^2 at 450 °C*, Jihwan An et al., Nano letters, Otterbein university, 2013.

[11] *Micro solid oxide fuel cells and their fabrication methods*, Piotr Jasinski, Faculty of Electronics, Telecommunication and Informatics, Gdansk University of Technology, Gdan´ sk, Poland, 2008.

[12] *Powering the Wireless World with MEMS*, Samuel B. Schaevitz, Lilliputian Systems, Inc., Micromachining and Microfabrication Processes Technology, Wilmington, MA, USA, 2012.

[13] *The Applicability of Sr-deficient n-type $SrTiO_3$ for SOFC Anodes*, T. Kolodiazhnyi & A. Petric, Journal of Electroceramics, 2005.

[14] *High-Performance Ultrathin Solid Oxide Fuel Cells for Low-Temperature Operation*, Hong Huang et al., Journal of The Electrochemical Society, 2007.

[15] *Integration of thin film-based micro solid oxide fuel cells in silicon technology*, Iñigo Garbayo Senosiain, PhD thesis in "Nanoscience" Program, University of Barcelona, electronic department, physic faculty, 2013.

[16] *Micro solid oxide fuel cells: a new generation of micro-power sources for portable applications*, F. Chiabrera et al., Invited paper, Catalonia Institute for Energy Research (IREC), 2017.

[17] *Integration of thin film-based micro solid oxide fuel cells in silicon technology*, Dolors Pla I Asesio, PhD thesis in "Engineering and Advanced Technologies" Program, University of Barcelona, electronic department, physic faculty, 2015.

[18] *Review on microfabricated micro-solid oxide fuel cell membranes*, A. Evans et al., Journal of Power Sources, 2009.

[19] *An introduction to Microelectromechanical Systems Engineering*, N. Maluf, Artech House, 2000.

[20] *Thin Film Materials Technology: Sputtering of Compound Materials*, Kiyotaka Wasa et al., 2004.

[21] *Coatings*, M. Ferraris, Applied science and technology department, Politecnico di Torino (Italy), *Advanced Materials for Energy* course of study, 2014.

[22] *Full ceramic micro solid oxide fuel cells: towards more reliable MEMS power generators operating at high temperatures*, I. Garbayo et al., Energy & Environmental Science, 2014.

[23] *Micro Solid Oxide Fuel Cells on Glass Ceramic Substrates*, Ulrich P. Muecke et al., Advanced Functional Materials, 2008.

[24] *Simple fabrication of micro-solid oxide fuel cell supported on metal substrate*, Jong Hoon Joo and Gyeong Man Choi, Journal of Power Sources, 2008.

[25] *Scalable nanostructured membranes for solid-oxide fuel cells*, M. Tsuchiya et al., Nature Nanotechnology, 2011.

[26] *Nanoscale membrane electrolyte array for solid oxide fuel cells*, Pei-Chen Su and Fritz B. Prinz, Electrochemistry Communications, 2012.

[27] *Three-Dimensional Nanostructured Bilayer Solid Oxide Fuel Cell with 1,3 W/cm² at 450 °C*, Jihwan Ant et al., Nano letters, ACS publications, 2013.

[28] *Processing of Foturan® glass ceramic substrates for micro-solid oxide fuel cells*, R. Tölke et al., Journal of the European Ceramic Society, 2012.

[29] *M. V. F. Schlupp, A. Evans, J. Martynczuk and M. Prestat,* Advanced Energy Material, 2013.

[30] *Nanoporous YSZ film in electrolyte membrane of Micro-Solid Oxide Fuel Cell*, S. Rey-Mermet, Thin Solid Films, 2010.

[31] *Pt/$Y_{0.16}Zr_{0.84}O_{1.92}$/Pt thin film solid oxide fuel cells: Electrode microstructure and stability considerations*, Kian Kerman, Journal of Power Sources, 2011.

[32] *High-Performance Micro-Solid Oxide Fuel Cells Fabricated on Nanoporous Anodic Aluminum Oxide Templates*, Chang-Woo Kwon, Advanced Functional Materials, 2011.

[33] *Nanostructured ruthenium e gadolinia-doped ceria composite anodes for thin film solid oxide fuel cells*, Yuto Takagi et al., Journal of Power Sources, 2012.

[34] *Micro solid oxide fuel cell fabricated on porous stainless steel: a new strategy for enhanced thermal cycling ability*, Kun Joong Kim et al., Scientific Reports, 2016.

[35] *Is it possible to design a portable power generator based on micro-solid oxide fuel cells? A finite volume analysis*, D. Pla et al., Journal of Power Sources, 2015.

[36] *Cisco Visual Networking Index: Global Mobile Data Traffic Forecast Update, 2017-2022*, Cisco, February 2019.

[37] *Batteries for Portable Devices*, G. Pistoia, Elsevier Science, 2005.

[38] *Energy Harvesting and Storage for Electronic Devices 2009-2019*, P. Harrop, R. Das, IDTechEx, 2009.

[39] *Fuel cell technologies - Part 6: Micro fuel cell power systems*, International Electrotechnical Commission (IEC), Geneva, 2010.

[40] *http://www.ultrasofc.eu/index.php/research.*

[41] *Unraveling bulk and grain boundary electrical properties in $La_{0,8}Sr_{0,2}Mn_{1-y}O_{3\pm\delta}$ thin films*, F. Chiabrera et al., APL Materials, 2018.

[42] *Wafer bonding for MEMS*, P. Enoksson et al., Solid State Electronics Laboratory, Chalmers University of Technology, Göteborg, Sweden, 2005.

[43] *https://www.seas.upenn.edu/~nanosop/Bonding_Methods.htm*.

[44] *Silicon fusion bonding and its characterization*, C. Harendt, Journal of Micromechanics and Microengineering, 1999.

[45] *Glass frit bonding: a universal technology for wafer level encapsulation and packaging*, Roy Knechtel, technical paper, Microsystem Technology, 2005.

[46] *Glass and glass ceramic for energy conversion devices*, F. Smeacetto, Energy department, Politecnico di Torino (Italy), *Advanced Materials for Energy* course of study, 2014.

[47] *Fundamentals of inorganic glasses*, Arun K. Varshneya, Elsevier, 2013.

[48] *Glass-ceramic seal to join Crofer 22 APU alloy to YSZ ceramic in planar SOFCs*, Federico Smeacetto, Journal of the European Ceramic Society, 2007.

[49] *Glass frit bonding with controlled width and height using a two-step wet silicon etching procedure*, Liu Yifang et al., Journal of Micromechanics and Microengineering, 2016.

[50] *https://www.bosch-sensortec.com/bst/support_tools/technology/overview_technology*.

[51] *http://www.sfscientific.com/science/2016/04/08/perovskite-structure-abo3*

[52] *Structure and properties of $La_{0.4}Sr_{0.4}TiO_3$ ceramics for use as anode materials in solid oxide fuel cells*, D. Neagu and J. Irvine, Chemistry of Materials, 2010.

[53] *Thermal, electrical, and electro-catalytical properties of lanthanum-doped strontium titanite*, O. Marina et al., Solid State Ionics, 2002.

[54] *Large polaron hopping phenomenon in lanthanum doped strontium titanite*, S. Singh et al., Journal of Alloys and Compounds, 2017.

[55] *Synthesis and performance of A-site deficient lanthanum-doped strontium titanite by nanoparticle based spray pyrolysis*, D. Burnat et al., Journal of Power Sources, 2011.

[56] *Structural, optical, and electrical properties of strained La-doped $SrTiO_3$ films*, M. Choi, Journal of applied physics, 2014.

[57] *Electrical conductivity and structural stability of La-doped $SrTiO_3$ with A-site deficiency as anode materials for solid oxide fuel cells*, Xue Li et al., International Journal of hydrogen energy, 2010.

[58] *Preliminary Data Sheet of Glass No: G018-197*, SCHOTT AG Business Unit Electronic Packaging, 2018.

[59] *Glasses*, M. Ferraris, Applied science and technology department, Politecnico di Torino (Italy), *Advanced Materials for Energy* course of study, 2018.

[60] *http://www.micro.magnet.fsu.edu/primer/java/interference/index*.

[61] *http://thermalanalysislabs.com/dilatometry.*

[62] *Contact angle and wetting properties*, Y. Yuan and T. Randall Lee, Department of chemistry, University of Houston, 2013.

[63] *Glass frit free of alkaline, lead and cadmium and its use to produce coloured enamels*, Patent: CN101092308A, 2006.

[64] *Process for verifying a hermetic sealant and semiconductor device*, Steven Edward Staller, patent number 6074891, date of patent June 13, 2000.

[65] *Role of substrate temperature in the Pulsed Laser Deposition of Zirconium Oxide Thin Film*, J. Mittra et al., Material Science, 2012.

[66] *Effect of Laser Fluence on Electrical Properties of $Sr_{0,75}La_{0,25}TiO_3$ Thin Films Grown by Pulsed-Laser-Deposition*, K. Eom et al., Journal of Nanoscience and Nanotechnology, 2014.

[67] *Basic principles of Data Acquisition*, introduction to crystallography and data acquisition, basic XRD course, PANalytical.

[68] *Pilas de combustible de óxidos sólidos (SOFC)*, Juan Carlos Ruiz Morales et al., Centro de la cultura popular Canaria, pag 208.

[69] *Electrochemical behavior of thin-film Sm-doped ceria: insights from the point-contact configuration*, Tae-Sik Jung, Sossina Haile, Royal Society of Chemistry, 2015.

[70] *High electrode activity of nanostructured, columnar ceria films for solid oxide fuel cells*, Woo Chul Jung, Sossina Haile et al., Energy and Environmental Science, 2012.

[71] *La-doped $SrTiO_3$ as anode material for IT-SOFC*, C. D. Savaniu and J. T. S. Irvine, Solid State Ionics, 2010.

[72] *Effect of Laser Fluence on Electrical Properties of $(Sr_{0,75}$-$La_{0,25})TiO_3$ Thin Films Grown by Pulsed-Laser-Deposition*, K. Eom et al., Journal of Nanoscience and Nanotechnology, 2014.

[73] *Exsolution of nickel nanoparticles at the surface of a conducting titanate as potential hydrogen electrode material for solid oxide fuel cells*, C. Arrivé et al., Journal of Power Sources, 2012.

[74] *Pulsed laser ablation of complex oxides: The role of congruent ablation and preferential scattering for the film stoichiometry*, Wicklein, S. Sambri, A. Amoruso, S. Wang, X. Bruzzese, R. Koehl, A., Dittmann, R., Applied Physics Letters, 101 (2012).

[75] *The impacts of cation stoichiometry and substrate surface quality on nucleation, structure, defect formation, and intermixing in complex oxide heteroepitaxy-LaCrO3 on SrTiO3(001),* Qiao, L. et al., Advanced Functional Material, 23, 2953–2963 (2013).

[76] *Nonstoichiometric accommodation in SrTiO3 thin films studied by positron annihilation and electron microscopy*, Keeble, D. J. et al., Phys. Rev. B 87, 195409 (2013).

[77] *Effect of cation off-stoichiometry on optical absorption in epitaxial LaFeO3 films*, Scafetta, M. D. & May, S. J. Phys. Chem. Chem. Phys. 19, 10371–10376 (2017).

[78] *https://www.3dprintingmedia.network/additive-manufacturing/am-technologies/what-is-liquid-deposition-modeling.*